Forschungszentrum Jülich

Institut für Grenzflächenforschung
und Vakuumphysik

Kinetic Growth Manipulation during Molecular Beam Epitaxy

Wulf Wulfhekel

Jül-3434

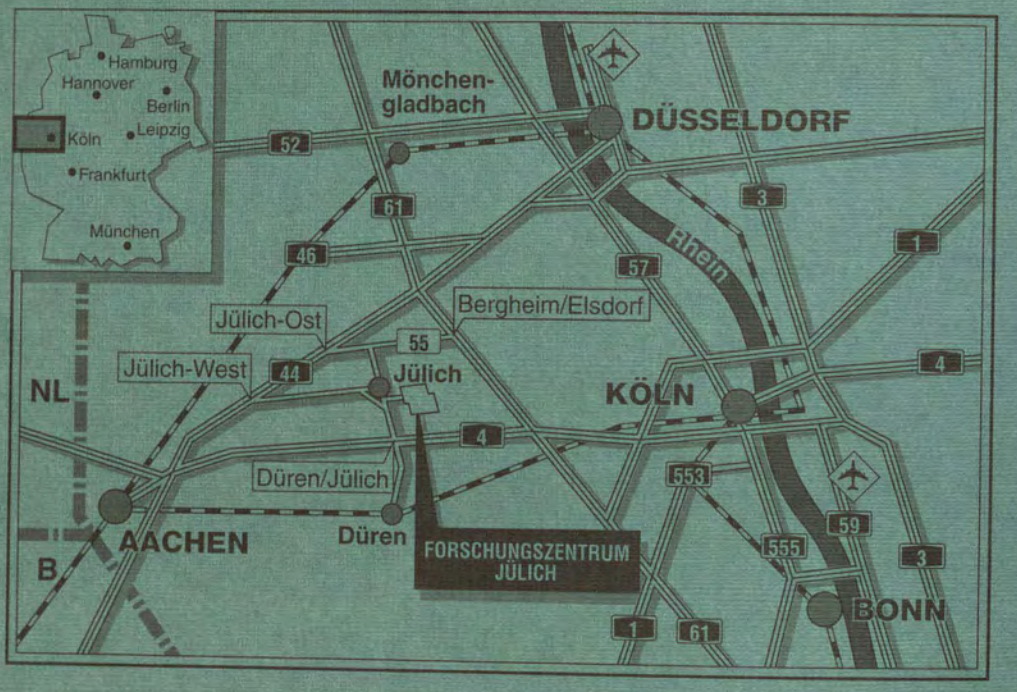

Berichte des Forschungszentrums Jülich ; 3434
ISSN 0944-2952
Institut für Grenzflächenforschung und Vakuumphysik Jül-3434
Diss. Universität Enschede, Niederlande

Zu beziehen durch: Forschungszentrum Jülich GmbH · Zentralbibliothek
D-52425 Jülich · Bundesrepublik Deutschland
☎ 02461/61-6102 · Telefax: 02461/61-6103 · e-mail: zb-publikation@fz-juelich.de

Kinetic Growth Manipulation during Molecular Beam Epitaxy

Wulf Wulfhekel

Abstract

The growth of ultra thin films of Cu and Ni on Cu(111) as well as Si on Ge(100) by molecular beam epitaxy is studied in-situ with helium atom scattering (TEAS), LEED or STM. During growth with constant deposition parameters at temperatures, where the film structure is determined by kinetics and not thermodynamics, in all three cases three-dimensional structures evolve. Due to a hampered interlayer mass transport, nucleation of higher layer islands sets in before the lower layers are completed. Using the purely kinetic concept of two mobilities, layer-by-layer growth in all three cases is obtained. This concept is based on creating an artificially enhanced density of islands during the early stage of monolayer growth such that nucleation on top of these smaller islands is prevented up to the stage of coalescence. However, details of the growth recipes have to be adjusted to the specific kinetics of the system under investigation. In case of Ni/Cu(111), interdiffusion limits the applicability of temperature variation to enhance the island density. In the case of Si/Ge(100), interlayer mass transport is hampered only at double steps. Hence in this system, growth manipulation is adjusted to avoid the formation of such steps. By measuring the island density or other film properties as a function of temperature or by direct observation of diffusion processes with STM, different microscopic diffusion barriers are estimated.

Contents

Chapter 1

Introduction

One of the major aims of epitaxy is to produce smooth films, since flat films of constant thickness are essential for many technological applications of thin film systems. Device characteristics may depend critically on the film thickness, on the chemical sharpness or interface roughness between film and substrate. Often, a chemically sharp and flat interface between two films or between film and the substrate is desired. For example in sandwiched structures of different semiconductors a modulation of the bandgap leads to many new and exciting quantum well features [1] and are of large technological potential for opto-electronic devices [2, 3, 4] or high speed electronics [5]. However, the sandwiched films have to be of microscopically constant thickness in the film plane to achieve coherent film properties. Interface roughness or insufficient chemical sharpness between the two semiconductors have a negative influence on device properties and hence a sharp and flat interface is necessary [6, 7]. Similar constraints hold for analogous systems like alternating layered films of magnetic and non magnetic metals, giving rise to the giant magnetic resistance effect [8, 9], which is of large interest for magnetic recording [10], or alternating layered films of superconductors and insulators in a Josephson junction [11]. All major device characteristics strongly depend on the film smoothness. However, these seemingly rather simple requirements for the topology of the films are by no means under complete control. Even in the simplest case, where substrate and film are of the same kind, i.e., in homoepitaxy, the problem of controlling the film morphology has not been solved completely [1].

During the past 40 years, intensive studies of film growth as function of the two free parameters, deposition rate and substrate temperature, have been carried out, but for many systems the mere variation of the growth parameter in this parameter space does not lead to flat films. Often, a high growth temperature or a low rate is chosen to allow equilibration of the surface during growth with the hope to minimize roughness. This thermodynamical way of approaching the problem is doomed to fail in heteroepitaxial systems, as been shown by Bauer [13]. Due to the difference in the

[1] Even in the extensively studied homoepitaxial system of Si/Si(100), surprising new findings on basic properties during growth are made up to the present day [12].

surface free energies of the two materials, only in one of the two configurations, the film wets the substrate. In the other case, droplets or crystallites form on the surface already at the early stages of growth (Volmer-Weber growth mode). In addition, the misfit between the two lattice constants leads to an increase of the free energy of the film with film thickness. At high temperatures, this also results in three-dimensional growth above a certain film thickness (Stranski-Krastanov growth mode). In the worst case, even a rough film is not a thermodynamically stable configuration due to the tendency of intermixing of the two materials.

A more promising view of the growth process offers the kinetic picture. Not only, that it is a more realistic view due to the very high supersaturation of adatoms on the surface especially for high deposition rates and low temperatures, but it also holds the key for controlling growth by kinetic growth manipulation, as shown by Rosenfeld et al. in the case of homoepitaxy on a non reconstructed, closed packed metal surface [14, 15, 16]. The basic idea behind growth manipulation is to enhance interlayer mass transport by increasing the number of nuclei during the first stage of monolayer growth. Two different mobilities are used - a low one during nucleation and a high until completion of a monolayer is achieved. By this, the diffusing atoms that land on top of the growing islands of the film reach the island edges more frequently in comparison to conventional growth, such that the probability that they overcome the diffusion barrier to cross the descending step edge is largely enhanced. So, nucleation of second layer islands is largely suppressed and growth proceeds in a nearly layer-by-layer mode resulting in flat films. The aim of this work is to study the technique of kinetic growth manipulation in further detail and to expand it to other systems namely heteroepitaxial ones and semiconductors.

After a short introduction into the elementary processes occurring during homo- and heteroepitaxial growth, the method of two mobilities is discussed and the experimental techniques used are illustrated.

In the second chapter, the natural and manipulated growth of Cu on Cu(111) is discussed and it is shown, that growth manipulation does lead to the aim of flat surfaces.

The third chapter deals with the manipulation of growth of Ni on Cu(111). Here additional effects complicate the realization of the method of two mobilities. However, in several cases, also in this heteroepitaxial system, flat films could be grown.

In the last chapter, the complex diffusion processes of Si on the (2x1) reconstructed surface of Ge(100) are studied. It is shown that the concept of two mobilities can be modified, so that even in this case, flat films can be grown.

1.1 Atomic Processes during MBE

During molecular beam epitaxy atoms with thermal energy, i.e., low kinetic energy, are deposited onto a surface. During the deposition event, the atoms gain the binding energy which is in the order of several eV. This energy is quickly dissipated and the individual deposited atoms equilibrate fast [17]. In some cases, the deposited atoms may travel a short distance on the surface during thermalisation, resulting in transient mobility [18] or downward funneling [19]. But it is only in few cases that these mechanisms play a significant role in the kinetics during growth like in the oxidation of Al(111) [20]. In the systems studied in this work, these dynamic process during adsorption can be neglected. Once bound to the surface, the deposited atoms usually cannot thermally overcome the desorption barrier due to the moderate substrate temperatures chosen. They stay on the surface. Hence, in the following also desorption is neglected (we want to grow things!). Under usual growth conditions, the deposited atoms have different possibilities to thermally diffuse on the substrate surface (see Fig. 1.1). Atoms on the surface, or in short terms 'adatoms', may jump from one lattice site to the next on a flat terrace. So they wander in a random way on the surface until they eventually meet e.g. an ascending step edge. Since coordination at a step edge is higher than on the terrace, adatoms are bound more strongly to an ascending step edge. Hence, step edges usually act as sinks for adatoms. When temperature is high enough, atoms may also diffuse along a step edge or may even thermally overcome the barrier to detach from a step edge and return to the terrace. On the other hand, an adatom might also approach a step edge from the upper side. To cross over to the lower terrace and to occupy the energetically favourable binding site two possible pathways exist. It may roll over the step. During this process, it is less coordinated for a short time which implies a high diffusion barrier. It may also push an atom of the step edge outward and take the former position of the step atom. This, so called exchange mechanism often has a lower barrier [21, 22]. Nevertheless, both processes may have a higher barrier than that of diffusion on the flat terrace. The additional barrier is called the step edge barrier [23, 24]. The diffusion over a downward step edge is called *inter*layer diffusion in contrast to diffusion on the flat terrace - the *intra*layer diffusion. An adatom diffusing on the terrace may also encounter other adatoms and build a small cluster. Since the coordination rises, these clusters may be stable and immobile. However, when the temperature is high enough, these clusters may be mobile [25] or may even loose atoms and decay [26].

Due to the crystal symmetry of the substrate, the different diffusion processes might differ along different crystal directions leading to a complex situation on the surface during growth as, e.g., in the case of Pt/Pt(110) [27] or Si/Si(100) [28]. However, already from a simplified picture of the diffusion processes the major aspects of growth kinetics can be grasped.

When the mobility of adatoms on the terraces is very high, all deposited adatoms reach pre-existing sinks like ascending step edges and are captured there (in absence

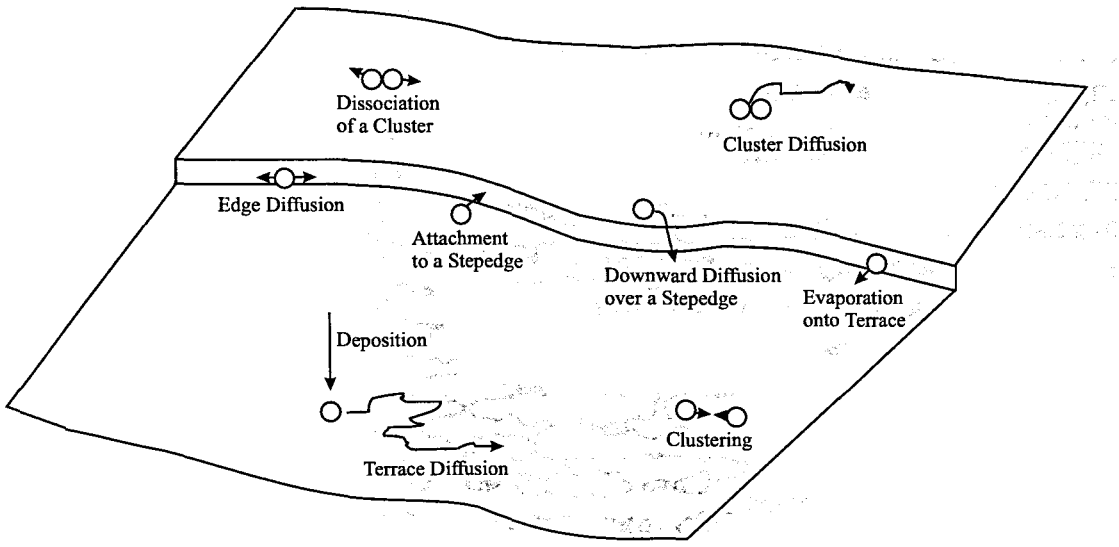

Figure 1.1: Elementary processes during growth

of a step edge barrier also by descending step edges) before they meet to form stable clusters. Hence, in this case the pre-existing step edges on the surface just propagate during growth and step-flow growth is achieved. Due to a practically unavoidable misorientation of the substrate, always some steps are present on the surface of a real crystal. Hence, step-flow growth will eventually occur on any crystal, provided the adatom mobility is high enough.

When the mobility of the adatoms is chosen to be lower by reducing the temperature and by this the diffusivity of the adatoms or equivalently by increasing the deposition flux, not all the adatoms reach pre-existing step edges before meeting other adatom(s) to form a stable cluster. Under these conditions, nucleation of islands sets in. When a saturation density of small islands or nuclei is established, the island separation is small enough that every adatom deposited on the terrace reaches an island (or a pre-existing step), nucleation ceases and the islands just grow laterally. When no step edge barrier exists, also the material deposited on top of the growing islands is captured by the island edge and the islands remain one layer high. So, the islands grow without nucleation of the second layer until shortly after coalescence. Then, not all the material deposited on the second layer reaches a sink quickly enough and nucleation of the next layer begins. This growth mode is called layer-by-layer or two-dimensional growth, since growth of subsequent layer islands

only starts, when the lower layer islands have coalesced.

With a rising step edge barrier, the descending step edges become less efficient sinks for adatoms and nucleation of second layer islands sets in earlier, i.e before coalescence. So, during growth, islands consisting of stacks of layers are built up. This growth mode is called three-dimensional or multilayer growth.

When the temperature is further reduced or the rate further increased, one after the other diffusion process is becoming inefficient on the time scale set by the deposition. So for example, the diffusion along step edges might become inefficient leading to dendritic or fractal island growth shapes [29]. Finally at very low mobilities, the adatoms might even not find a correct lattice position and the growing layer accommodates crystal imperfections as stacking faults [30] or in the worst case is amorphous [31]. The latter case is mainly observed in growth of semiconductors.

1.1.1 Homoepitaxy

During homoepitaxy per definition, substrate and deposited material are of the same kind. As a consequence, homoepitaxial systems can be regarded as simplest possible model systems, where growth kinetics can be studied in its pure form. No difference between deposited material and substrate has to be made and no complicating effects arise due to a misfit between substrate and film or differences of surface free energies or other physical properties. In homoepitaxial systems, growth manipulation is mainly of academic interest. Layer-by-layer growth in these systems can simply be achieved by very high substrate temperatures, so that growth proceeds via step-flow and the surface always remains in the thermodynamically favoured flat state. Nevertheless, the detailed study of homoepitaxial growth may lead to fundamental understanding of growth kinetics that may also help to grow flat heteroepitaxial films. Besides this, during growth of very thick heteroepitaxial films eventually a transition to a homoepitaxial growth situation occurs, but due to the tendency of alloying of film and substrate very high temperatures have to be avoided.

1.1.2 The Concept of Two Mobilities

For mobilities below the step-flow regime, nucleation and growth of islands on the terraces is observed. During the early stages of monolayer growth, the supersaturation of adatoms deposited onto the surface leads to nucleation of first layer islands with a characteristic separation λ, depending on the deposition rate and substrate temperature [32], i.e., the mobility. Nucleation ceases at a coverage of several percent of a monolayer and the second stage of monolayer growth, the growth and coalescence of islands takes place. In the case of the absence of a step edge barrier, nucleation of second layer islands only sets in near layer completion when islands have coalesced. Layer-by-layer growth occurs and flat films can be grown without complications. However, when a finite step edge barrier exists, the adatoms that are deposited on top of the growing islands are reflected at the descending step edge

with a non vanishing probability; interlayer mass transport is partially suppressed. For small islands, this does not lead to immediate nucleation of a second layer island, since the adatoms landing on a small island visit the island edge frequently and may eventually succeed in descending the step edge. In addition, the total flux onto a small island is low, so that it is unlikely that several adatom are at the same time trapped on the island leading to the formation of a stable nucleus. However, the islands of the first layer grow by capturing adatoms deposited on the terrace and on them and when they reach a critical diameter d_c, depending on the adatom mobility and the size of the barrier, nucleation of a second layer island takes place [33]. For a finite step edge barrier, d_c is smaller than λ, leading to second layer islands before coalescence of the first layer islands, i.e., three-dimensional islands are grown and film growth is rough. This only holds though, when the adatom mobility is constant during monolayer deposition. Here lies the key to manipulate the growth mode. When the adatom mobility is varied during growth, the relation between λ and d_c may be changed and they may be adjusted independently. The idea of the concept of two mobilities is, to have a small mobility during nucleation, leading to a small typical island distance λ or, equivalently, a high density of small islands. After nucleation, growth is continued with a high mobility, resulting in a larger d_c. If the adatom mobility is varied only strongly enough, d_c may eventually be larger than λ and nucleation of second layer islands only sets in after coalescence of the first layer islands. Layer-by-layer growth is achieved. Besides the variation of the mobility during nucleation, also the creation of a high density of nuclei by some other means leads to the same improvement of interlayer mass transport.

1.1.3 Heteroepitaxy

In model experiments, Rosenfeld et al. showed that in the case of homoepitaxy of Ag on Ag(111) the application of this purely kinetic concept of two mobilities indeed results in an enhanced interlayer mass transport and rather flat films [14]. In chapter 2.4 we study growth manipulation in more detail for the homoepitaxial system Cu/Cu(111).

For technological applications of thin films, film and substrate need to differ in some physical property allowing to realize specific functions. Therefore, deposited material and substrate often are of different kind and hence the fabrication of such structures involves heteroepitaxy.

Heteroepitaxy substantially differs from homoepitaxy, as can easily be seen from thermodynamic considerations. First, substrate and film material in general have different surface free energies. This means, that only in one of the configurations, the film material may wet the substrate. In the other case, a closed film would give rise to a higher surface free energy. The film then usually splits up in three-dimensional droplets or crystallites at high substrate temperatures to reduce its surface energy. Hence, for half of the substrate film configurations, the surface energies of the materials do not allow to grow flat films by growth at high temperatures, since

thermodynamics drives growth to a three-dimensional mode. Second, substrate and deposited material often have a different natural lattice spacing and during growth of pseudomorph films, the lattice mismatch results in a build up of strain. During growth the film either eventually reacts with the formation of dislocations or the growth front roughens strongly as Bauer showed [13]. The three-dimensional islands created by this can elastically relax in the higher layers as e.g. observed in the system Ge/Si(100) [34]. The higher the substrate temperature, the faster the system reacts on the strain. Again, the growth of flat films by choosing a high substrate temperature will not lead to the desired result. Third, the desired flat film with a chemically sharp interface might altogether not be the thermodynamic stable configuration due to a tendency of film and substrate material to alloy. Also in this case, growth at high temperatures is counter productive. Therefore, growth recipes are needed that allow to grow flat films at lower temperatures, where the pathway to the thermodynamic equilibrium is still blocked. Here, the kinetic picture of growth is more promising and the concept of two mobilities can show its full power. Growth is performed at such low temperatures that film morphology is determined by kinetics and thermodynamic considerations about the film morphology have not to be made. However, it is a priori not clear that also in heteroepitaxy the kinetic growth manipulation succeeds, since also the kinetics of heteroepitaxy differs from that of homoepitaxy. For example, the diffusion speed of adatoms on the substrate and on differently high layers of the film can substantially differ [35, 36], details of interlayer mass transport may vary in different layers or the strain might play such a dominant role, that it alters growth kinetics substantially.

In the heteroepitaxial growth manipulation experiments in this thesis, we tried to apply the concept of two mobilities to the systems Ni/Cu(111) and Si/Ge(100). In both cases, the deposited material has a higher surface free energy than the substrate and a tendency of alloying is known. In Ni/Cu(111) the misfit is moderate (2.5%) while for Si/Ge(100) it is with 4.2% of substantial size. As will be shown, in both cases growth manipulation indeed leads to flatter films, although details of some growth recipes have to be adjusted to the system under investigation.

1.2 Experimental Methods

To study the growth of thin films, two complementary approaches were taken in this work. In the first two chapters of this work, diffraction methods, namely thermal energy atom scattering (TEAS) and low energy electron diffraction (LEED), were used that easily allow monitoring of the growth process in real time *during deposition* [37, 38]. With these scattering methods, one obtains information from the surface that is averaged over the beam diameter, which is in the order of one square millimeter. This fact holds the advantages and disadvantages of these methods. It is relatively easy to obtain a qualitative picture of the surface from the diffraction pattern. Quantities like the average island separation, the defect density, the step height or facet angles can be determined accurately, but it is impossible to invert the diffraction pattern by Fourier techniques to obtain all information about the morphology of the surface. Scattering methods are most useful in the study of non reconstructed closed packed surfaces, where no different adsorption sites exist. Hence, these methods are used to examine growth and growth manipulation on the (111) surface of copper in real time and in a large temperature range. In the second part of this study, a real space method, namely scanning tunneling microscopy (STM), is used that allows to examine the morphology of the films *after deposition* in great detail. This method has the great advantage that one actually sees all the surface features. However, only a very small area is scanned and many pictures are necessary to obtain good statistics for average quantities like the mean island density. An other disadvantage is that it is hard, though not impossible, to study the growth in vivo [39] or over a large temperature range [40]. For the rather complex situation of growth on the reconstructed surfaces of Ge(100) with all the different local configurations, STM as a high resolution real space method is more suitable and hence is used in the second part of this work. The following sections describe the experimental methods and set-ups in more detail.

1.2.1 Helium Atom Scattering

Thermal energy atom scattering of He atoms was used to study the growth of Cu and Ni on Cu(111). Figure 1.2 sketches the experimental set-up. The He gas of high purity (99.999%) and high pressure (70-90 bar) is adiabatically expanded through a nozzle with a diameter of 10 μm into the vacuum of the nozzle chamber ($p < 10^{-4}$ mbar under operation). During the expansion, the whole enthalpy of the gas, which is determined by the nozzle temperature T_D, is transferred into kinetic energy of the supersonic He beam [41]. So, a monochromatic beam of an energy of $E_{He} = 5/2 k_B T_D$ and $\Delta\lambda_{He}/\lambda_{He} \approx 0.02$ is formed [42]. In a second step, the outer regions of the beam are removed by a skimmer and the beam passes the chopper chamber ($p \approx 10^{-7}$ mbar) before it enters the main chamber through an aperture. In the main chamber, the beam has a divergence of 0.2° and hits the surface with a width of less than 1mm [42]. The beam is then reflected from the sample surface

and is detected in a quadrupole mass spectrometer (QMS) with a solid angle of acceptance of 0.15°. Both, the sample and the detector, can be rotated around two axes allowing to vary the scattering conditions over a wide range. During operation of the He beam, the pressure in the main chamber rises from $\approx 2 \times 10^{-11}$ mbar to $\approx 2 \times 10^{-9}$ due to the increase of the partial pressure of He. This He background pressure limits the signal to noise ratio of the detection of the reflected He beam in the QMS to 10^3. By using a chopped beam and lock-in techniques, higher signal to noise ratios can be achieved.

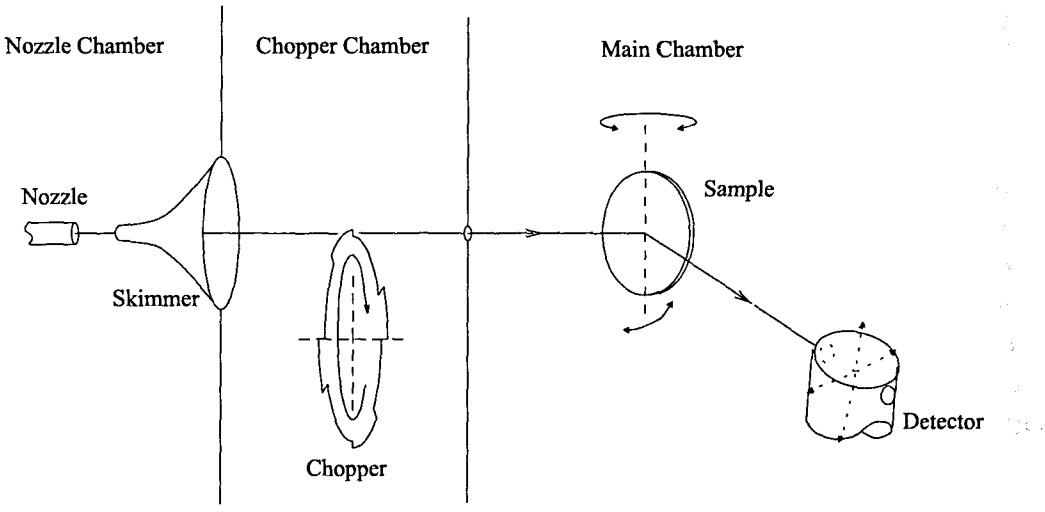

Figure 1.2: Schematic set-up of the TEAS apparatus.

TEAS is of very high surface sensitivity, since the low thermal energy of the He atoms and the strong repulsive interaction of the filled electron shell of the helium and the outer valence electrons of the surface [43] leads to a classical turning point of the He atoms that lies 3-4 Å *in front of* the surface [44, 45]. At these distances, low indexed metal surfaces display only a very small corrugation [46, 47] (e.g.$\approx$ 0.01Å in the case of Pt(111) [48]). Hence, most of the beam is specularly reflected into the (00) reflex and higher order reflexes are by three to four orders of magnitude weaker. The surface practically acts as a mirror. Besides the exclusive surface sensitivity and the simple scattering situation, the low energy of the He atoms also guarantees a practically non destructive probing of the surface and processes on the surface, which makes TEAS an ideal method to study undisturbed growth in vivo.

Fig. 1.3 sketches the elastic scattering of He atoms from a mirror like metallic surface containing an atomic step. Due to local distortion of the flat potential by

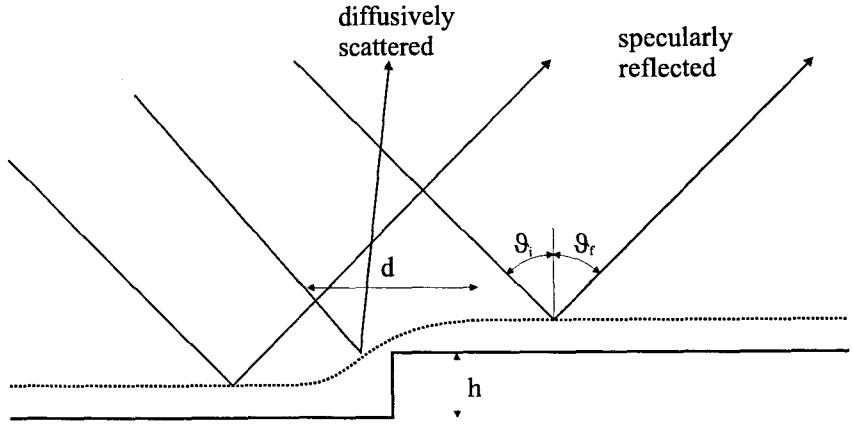

Figure 1.3: Scattering of the He beam from a stepped surface.

the step, helium atoms hitting this area will not be specularly reflected but are lost from the (00) beam ($\vartheta_i \neq \vartheta_f$). Phenomenological, this effect can be described by a stripe of roughly 10 Å around step edges that causes diffuse scattering. Scattering from the two adjacent terraces leads to interference in the detector. The phase difference between the two specularly reflected beams, i.e., the scattering phase S is determined by the angle of incidence $\vartheta = \vartheta_i = \vartheta_f$, the wave length of the He beam λ and the step height h :

$$S = \frac{2h\cos\vartheta}{\lambda} \tag{1.1}$$

The nozzle set-up used in all experiments of this work did not allow to vary the nozzle temperature; it was fixed to room temperature. This results in a 67 meV He beam, corresponding to a de Broglie wave length of λ =0.556 Å. Hence, the scattering phase S was varied by varying the angle of incidence ϑ.

In the case of in-phase scattering conditions ($S = 1, 2, 3 \ldots$) interference is constructive and the only loss in the specular beam is caused by diffuse scattering. Then, the normalized intensity is given by [42]:

$$\frac{I}{I_0} = (1 - ds)^2 \tag{1.2}$$

where d is the width of the stripe causing diffuse scattering and s is the density of steps on the surface. Under this scattering condition, one obtains a high sensitivity to step edges or other defects like point defects or adsorbed atoms, which also cause

strong diffuse scattering. However, from the reflected intensity no information can be gained on the distribution of open layers.

In the case of anti-phase scattering conditions ($S = 1/2, 3/2, 5/2 \ldots$) interference is destructive. Then the specularly reflected normalized intensity is given by the layer distribution :

$$\frac{I}{I_0} = \left(\sum_{i=0}^{\infty}(-1)^i A_i\right)^2 \tag{1.3}$$

where A_i is the fraction of the visible area of atomic level i. For a three-level-system, this equation can also be inverted to obtain the coverages Θ_i in the three layers, when the total coverage Θ is known. For deposition of around one monolayer of material on a flat substrate, the inversion of equation 1.3 results in:

$$\Theta_1 = \frac{1}{4}\left(1 + 2\Theta + \sqrt{\frac{I}{I_0}}\right) \tag{1.4}$$

Due to the destructive interference from adjacent terraces, diffuse scattering has no influence on the specularly reflected anti-phase intensity for structures larger than d. For structures this large, the atoms scattered from the stripe around the step edge would also have been lost from the specular beam by interference. However, when very small structures are present on the surface or when the structures are not compact but ramified or fractal, diffuse scattering may become significant also under anti-phase scattering conditions leading to a loss in the specular reflected intensity.

Due to limited coherence of the He-beam, the linear dimension from which coherent information is gathered, i.e. the transfer width, is finite. For structures much larger than the transfer width, the difference of in- and anti- phase scattering condition vanishes. The transfer width of the set-up during operation at the selected scattering conditions ($S = 2, 2.5$) is ≈ 420 Å.

Besides the specularly reflected intensity, also the intensity distribution around the geometrically reflected beam, i.e. the shape of the specular spot, contains information about the surface morphology. In the kinematic approximation, the intensity distribution $I(k_{\|}, k_{\perp})$ of the scattered wave as the function of perpendicular momentum transfer $k_{\perp}$ and parallel momentum transfer $k_{\|}$, i.e. the diffraction pattern, is given by the Fourier transform of the autocorrelation function $\Phi(x, k_{\perp})$ of the surface [49]:

$$I(k_{\|}, k_{\perp}) = \int_x \Phi(x, k_{\perp}) e^{ik_{\|}x} dx \tag{1.5}$$

where $\Phi(x, k_{\perp})$ is given by the perpendicular momentum transfer $k_{\perp}$ and the height of the surface $h(x)$ at position x as follows [51] :

$$\Phi(x, k_{\perp}) = \int_y e^{ik_{\perp}(h(x+y)-h(y))} dy \tag{1.6}$$

Except for the diffusely scattered part of the intensity, this simple kinematic approximation is valid for TEAS.

In this work, island densities after homogeneous nucleation are estimated from anti-phase peak profiles. An isotropic island distribution with typical island separation λ results in a ring of intensity around the specular spot [50], reflecting the correlation between neighboring islands according to equation 1.5. A radial linescan through the diffraction spot shows the central specular peak and two additional peaks caused by the ring. The additional peaks can be approximated by Lorentzians with parameters depending on the details of the distribution of island separations. The distance from the central spot gives the most probable island separation and the width of the peaks the scatter in the island distribution. From both parameters, an estimate of the average island separation and hence the island densities can be obtained, according to Wollschläger et al. [51].

The limited transfer width results in a minimum half-width of the spot. The observed diffraction pattern can be written as a convolution of the ideal diffraction pattern, obtained with a hypothetical instrument of infinite transfer width, and the instrument function which can be approximated by a Gaussian with a half width of the inverse of the transfer width of the instrument [49].

At temperatures where the adatoms are mobile, ideal three-dimensional growth is due to the complete lack of interlayer mass transport. For this type of growth, both in- and anti-phase He specular intensity decay monotonically. The normalized anti-phase intensity follows an exponential decay law :

$$I^{anti}/I_0^{anti} = e^{-4\theta} \tag{1.7}$$

where θ is the coverage in monolayers (ML) [42]. Accompanied by this decay, the anti-phase peak profile of the (00) spot widens with coverage.

During layer-by-layer growth mass transport between layers is efficient, resulting in oscillations of the He intensity under both diffraction conditions. The minimum intensity corresponds to deposition of about 0.5 ML, when the surface is roughest. Accordingly, the anti-phase peaks widens and reaches a maximum width at half monolayer coverage. The maximum intensity corresponds roughly to completion of a layer, where the surface again is smooth and in accord to this the anti-phase peak profile is sharp again.

During step-flow growth, both in- and anti-phase intensities remain constant and the anti-phase peak sharp.

1.2.2 SPA-LEED

Besides TEAS, low energy electron diffraction (LEED) was used in this work as a second diffraction technique. Figure 1.4 sketches the experimental set up. The commercially available Omicron SPA-LEED consists of an electron gun with a LaB_6 cathode, an octopole electron optics and a channeltron with small aperture. During operation, the octopole is used to scan the diffraction pattern over the aperture of

the channeltron. In this way, high resolution images of the diffraction pattern can be obtained. The high sensitivity of the channeltron allows low beam currents and hence low widening of the beam due to space charge, leading to transfer width of up to 2000 Å. The high linearity of the channeltron allows quantitative analysis of the observed diffraction profiles.

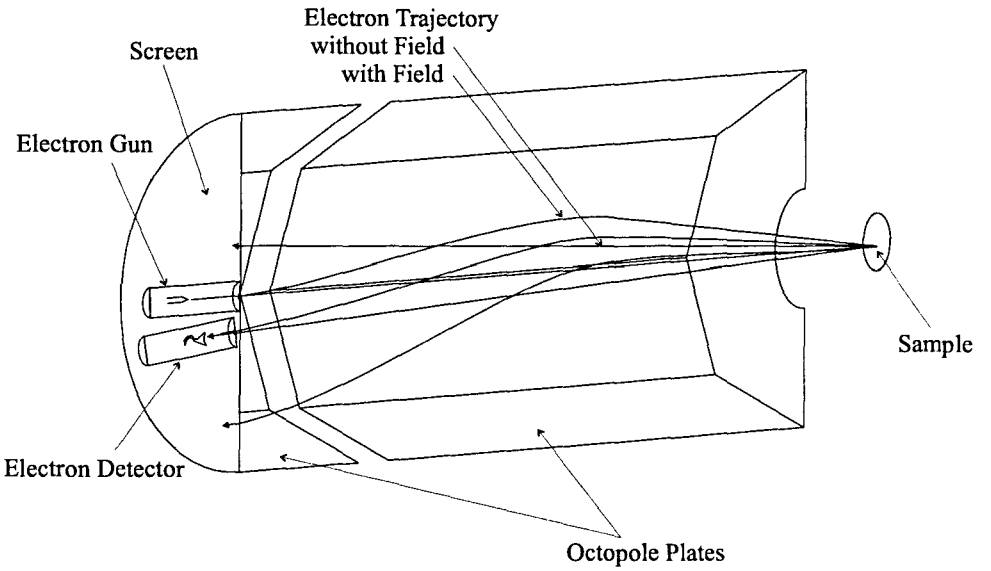

Figure 1.4: Sketch of the Omicron SPA-LEED set-up

Since the mean free path of the electrons in the solid is finite (and varies with energy), the experimentally observed LEED diffraction patterns cannot be completely explained on grounds of the simple kinematic approximation of equation 1.5. First, interference from the different atomic layers of the substrate leads to additional modulation of the intensity of all diffraction peaks and hence contains information about the layer structure of the crystal. Second, multiple scattering events cannot be neglected. Nevertheless, the shape of the different diffraction peaks can be well described in the kinetic approximation [52] according equation 1.5, similarly to TEAS, except for the absolute intensity. To also explain the intensity of a diffraction peak as a function of electron energy, i.e. its IV curve, more elaborate techniques must be used [53]. In this work, only the shape of LEED diffraction patterns peaks are used to study the film morphology. LEED IV curves are not analysed to gain structural information, since in the SPA-LEED used, the angle of incidence changes with electron energy when observing a certain diffraction peak with the channeltron. This fact makes the analysis of IV curves impractical.

To show the equivalence of the two diffraction methods used in this work, two

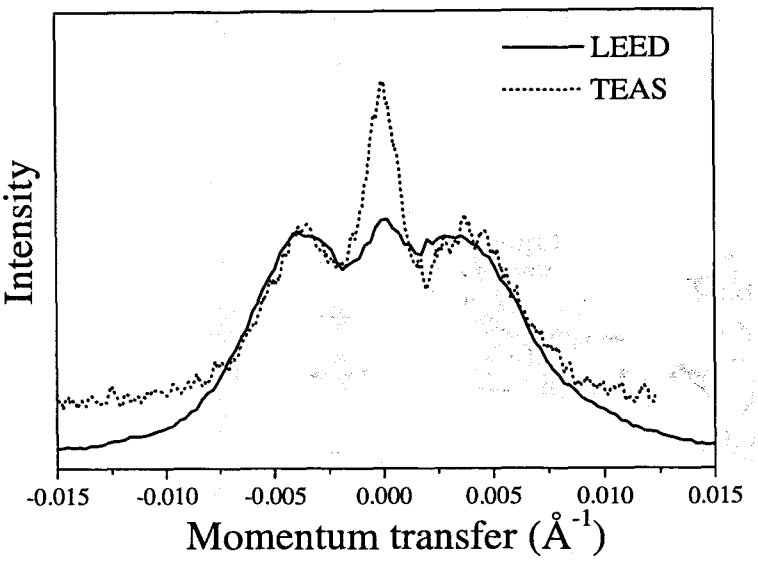

Figure 1.5: LEED and TEAS anti-phase spot profiles of the (00) spot from a Cu(111) surface with a high density of Cu islands.

linescans through the specular spot at anti-phase diffraction condition were taken from the same surface - one with TEAS and one with SPA-LEED - as displayed in Fig. 1.5. On the surface, a high island density was created by growth manipulation techniques followed by deposition to nearly half of a monolayer of Cu. Obviously, the shape of the two profiles is similar. However, when the structures on the surface become smaller than the width of the band of diffuse scattering around step edges d, TEAS diffraction peaks loose intensity and even the observed step height and by this the scattering phase S might change due to the Smoluchowski effect [54]. At these high step densities, SPA-LEED is more suitable to study film morphology.

1.2.3 Scanning Tunneling Microscopy

As a high resolution real space method, scanning tunneling microscopy (STM) allows one to take images of the surface morphology up to atomic resolution [55]. In this work, a commercially available room temperature STM from Omicron was used. The set-up consists of a UHV chamber system with a preparation chamber, equipped with a sputter gun and an evaporator, and an analysis chamber containing the STM (see fig. 1.6). Further, a load lock allowed the introduction (and removal) of samples and tips without braking the vacuum. A carousel close to the analysis chamber was used to store up to eight samples and tips. Both samples and tips are handled with

a wobble stick to insert (and remove) them into (from) the STM and the magnetic transfer stick of the preparation chamber and the load lock. The tips were prepared ex-situ by etching with NaOH solution. In the case that scanning with a tip did not result in images of atomic resolution, atomic resolution could usually be achieved after soft sputtering of the tip.

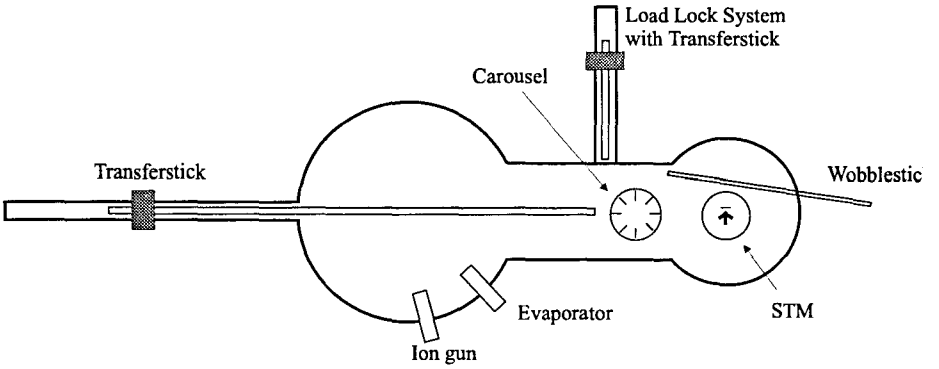

Figure 1.6: Sketch of the Omicron STM set-up

Images of the surfaces were taken after preparation or growth at room temperatures. When the preparation of the structures involved elevated temperatures, a time of approximately 15 minutes was needed to cool down the sample before tunneling could be started. Otherwise, the drift lead to strong distortions of the images. Different tip voltages were used in this work. In this way, different states or bands contribute to the tunneling current and by switching the sign of the tunneling voltage, both empty and filled state images were taken to unambiguously identify the surface features.

Bibliography

[1] F.F. Fang, P.J. Wang, B.S. Meyerson, J.J. Nocera, K.E. Ismail, Surf. Sci. **263**, 175 (1992)

[2] J.A. Moriarty and S. Krishnamurthy, J. Appl. Phys. **54**, 1892 (1983)

[3] R. People, J.C. Bean, D.V. Lang, A.M. Sergent, H.L. Störmer, K.W. Wecht, R.T. Lynch and K. Baldwin, Appl. Phys. Lett. **45**, 1231 (1984)

[4] T.P. Pearsall, J. Bevek, L.C. Feldman, J.M. Bonar, J.P. Mannaerts and A. Ourmazd, Phys. Rev. Lett. **58**, 729 (1987)

[5] see e.g. K. Ismail, M. Arafa, K.L. Saenger, J.O. Chu, B.S. Meyerson, Appl. Phys. Lett. **66**, 1077 (1995)

[6] E. Kasper and H. Jorke, J. Vac. Sci. Technol. A **10**, 1927 (1992)

[7] G. Theodorou and C. Tserbak, Phys. Rev. B **51**, 4723 (1995)

[8] P. Grünberg, R. Schreiber, Y. Pang, M.B. Brodsky and H. Sowers, Phys. Rev. Lett. **57**, 2442 (1986)

[9] M.N. Baibich, J.M. Broto, A. Fert, F. Nguyen Van Dau, F. Petroff, P. Etienne, G. Creuzet, A. Friedrich and J. Chazelas, Phys. Rev. Lett. **61**, 2472 (1988)

[10] B. Dieny, V.S. Speriosu, S.S.P. Parkin, B.A. Gurney, D.R. Wilhoit, D. Mauri, Phys. Rev. B **43**, 1297 (1991)

[11] R.G. Wichern, Planar High-T_C Josephson Junctions, Ph.D. Thesis University of Twente (1996)

[12] B. Voigtländer, T. Weber, P. Smilauer, D.E. Wolf, Phys. Rev. Lett. **78**, 2164 (1997); A.J. Hoeven, E.J. Loenen, D. Dykkamp, J.M. Lenssinek, J. Dieleman, Thin Solid Films **183**, 263 (1989)

[13] E. Bauer, Appl. Surface Sci. **11-12**, 479 (1982)

[14] G. Rosenfeld, R. Servaty, C. Teichert, B. Poelsema, G. Comsa, Phys. Rev. Lett. **71**, 895 (1993)

[15] G. Rosenfeld, B. Poelsema, G. Comsa, J. Cryst. Growth **151**, 230 (1995)

[16] G. Rosenfeld, N. N. Lipkin, W. Wulfhekel, J. Kliewer, K. Morgenstern, B. Poelsema, G. Comsa, Appl. Phys. A, **61**, 455 (1995)

[17] D.E. Sanders, A.E. DePristo, Surf. Sci. **254**, 341 (1991); P. Stoltze, J.K. Nørskov, Phys. Rev. B **48**, 5607 (1993)

[18] W.F. Egelhoff, Jr, I. Jacob, Phys. Rev. Lett. **62**, 921 (1989)

[19] J.W. Evans, D.E. Sanders, P.A. Thiel, A.E. DePristo, Phys. Rev B **41**, 5410 (1990)

[20] H. Brune, J. Wintterlin, R.J. Behm, G. Ertl, Phys. Rev. Lett. **68**, 624 (1992)

[21] S.C. Wang, G. Ehrlich, Phys. rev. Lett. **67**, 2509 (1991)

[22] J. Jacobsen, K.W. Jacobsen, P. Stoltze, J.K. Nørskov, Phys, Rev. Lett. **74**, 2295 (1995)

[23] G. Ehrlich, F. G. Hudda, J. Chem. Phys. **44**, 1039 (1966)

[24] R. L. Schwoebel, E. J. Shipsey, J. Appl.Phys. **37**, 3682 (1966)

[25] T.T. Tsong, P. Cowan, G.L. Kellogg, Thin Solid Films **25**, 97 (1975); G.L. Kellogg, Phys. Rev. Lett. **73**, 1833 (1994)

[26] see e.g. J.-K. Zuo, J.F. Wendelken, H. Dürr, C.-L. Liu, Phys. Rev. Lett. **72**, 3064 (1994)

[27] D.W. Basset, P.R. Webber, Surf. Sci. **70**, 520 (1978)

[28] Y.-W. Mo and M.G. Lagally, Surf. Sci. **248**, 313 (1991)

[29] R.Q. Hwang, J. Schröder, C. Günter, R.J. Behm, Phys. Rev. Lett. **67**, 3279 (1991)

[30] S.C. Wang, G.J. Ehrlich, J. Chem. Phys. **95**, 4071 (1991)

[31] D.J. Egelsham, H.-J. Grossmann, M. Cerullo, Phys. Rev. Lett. **65**, 1227 (1990)

[32] J. A. Venables, Phil. Mag. **27**, 697 (1973); J. A. Venables, G. D. T. Spiller, M. Hanbücken, Rep. Prog. Phys. **47**, 399 (1984)

[33] J. Tersoff, A.W. Denier van der Gon, R.M. Tromp, Phys. Rev. Lett. **72**, 266 (1994)

[34] Y.-W. Mo, D.E. Savage, B.S. Swartzentruber, M.G. Lagally, Phys. rev. Lett. **65**, 1020 (1990)

[35] J.A. Meyer, P. Schmid, R.J. Behm, Phys. Rev. Lett. **74**, 3864 (1995)

[36] H. Brune, K. Bromann, H. Röder, K. Kern, J. Jacobsen, P. Stoltze, K. Jacobsen, J. Nørskov, Phys. Rev. B **52**, R14380 (1995)

[37] B. Poelsema, A. F. Becker, R. Kunkel, G. Rosenfeld, L. K. Verheij, G. Comsa, Springer Proceedings in Physics Vol.**73** Eds. R. F. Howe, R. N. Lamb, K. Wandelt, Springer-Verlag, Berlin, 1993 pp. 95

[38] M. Henzler, T. Schmidt, E. Z. Luo, The Structure of Surfaces IV, ed. X. D. Xie, S. Y. Tong, M. A. van Hove, World Scientific, Singapore 1994, pp. 619

[39] B. Voigtländer and A. Zinner, Appl. Phys. Lett. **63**, 3055 (1993)

[40] H. Röder, R. Schuster, H. Brune and K. Kern, Phys. Rev. Lett. **71**, 2086 (1993)

[41] J. P. Toennies and K. Winkelmann, J. Chem. Phys. **66**, 3965 (1977)

[42] B. Poelsema and G. Comsa, Scattering of Thermal Energy Atoms, Springer Tracts in Modern Physics **115**, Springer, Berlin (1989)

[43] E. Zaremba and W. Kohn, Phys. Rev. B **13**, 2270 (1976)

[44] N. Esberg and J. K. Nørskov, Phys. Rev. Lett. **45**, 807 (1980)

[45] J. Harris and A. Liebsch, Phys. Rev. Lett. **49**, 341 (1982)

[46] G. Boato, P. Cantini and R. Tatarek, J. Phys. F **6**, L237 (1976)

[47] J. Horne, S. C. Yerkes and D. R. Miller, Surf. Sci. **93**, 47 (1980)

[48] K. Kern, Untersuchung dynamischer Oberflächeneigenschaften und zweidimensionaler Phasenübergänge an einer reinen und adsorbatbedeckten Pt(111)-Oberfläche mittels hochaufgelöster He-Streuung, Bericht des Forschungszentrum Jülich, Jül-2040, (1986)

[49] see e.g. J. E. Houston and R. L. Park, Surf. Sci. **21**, 209 (1970)

[50] see e.g. P. Hahn, J. Clabes, M. Henzler, J. Appl. Phys. **51**, 2079 (1980)

[51] see e.g. J. Wollschläger, J. Falta and M. Henzler, Appl. Phys. A **50**, 57 (1990)

[52] see e.g. M. Henzler, Appl. Phys. A **34**, 205 (1984)

[53] M.A. Van Hove, W.H. Weinberg, C.-H. Chan, Low Enerhy Electron Diffration : Theory and Surface Structure Determination, Springer-Verlag, Berlin 1986

[54] P. Bedrossian, B. Poelsema, G. Rosenfeld, L.C. Jorritsma, N.N. Lipkin, G. Comsa, Surf. Sci. **334**, 1 (1995)

[55] G. Binnig, H. Rohrer, Ch. Gerber, E. Weibel, Appl. Phys. Lett. **40**, 178 (1982); Phys. Rev. Lett. **49**, 57 (1992)

Chapter 2

Homoepitaxial Growth of Cu(111)

2.1 Introduction

Homoepitaxial systems can be used as model systems, where simple kinetic processes influencing epitaxial growth can be studied without complicating effects such as lattice mismatch, differences in surface energy, etc. A detailed understanding of the origin of the various phenomena occurring in homoepitaxy, as well as the development of general concepts and the identification of general trends are important for deriving from these simpler systems conclusions applicable to the more complex, and more useful, heteroepitaxial systems.

Such general trends seem to apply for homoepitaxy on non reconstructed fcc(100) metal surfaces, for which layer-by-layer growth is generally found (Pd [1], Ni [2], Cu [3, 4], Ag [4, 5, 6]). For homoepitaxy on fcc(111) metal surfaces the situation is more complex. The two model systems studied extensively – Pt/Pt(111) and Ag/Ag(111) – display a richness of behaviour, depending on the growth conditions (substrate temperature, deposition rate) and on the metal.

For homoepitaxy on Pt(111), three growth regimes were observed at temperatures below step-flow [7, 8, 9, 10, 11]: at intermediate temperatures (340-450 K), several layers grow simultaneously and the system grows three-dimensionally rough (3D growth). This mode of growth was explained by the existence of a barrier (step-edge barrier [12, 13]), hindering interlayer mass transport. At lower temperatures, a non-ideal layer-by-layer growth mode (reentrant 2D growth) is encountered, which was explained by the partial enabling of interlayer mass transport due to the dendritic shape of the islands growing at these temperatures [7]. Ab initio calculations show, that especially kinks in {111} step edges of the dendritic island are responsible for lowering the effective step edge barrier [14, 15]. At high temperatures, growth proceeds in an almost ideal layer-by-layer manner for a very large number of monolayers. This latter growth mode was explained initially by an increased probability for adatoms to thermally surmount the step-edge barrier. Recently, an alternative mechanism was proposed, tracing back this growth mode to a reconstruction network forming on the Pt(111) surface during deposition [16, 17]. Scanning Tunneling

Microscopy (STM) investigations [17] showed that those parts of the surface which are not reconstructed grow three-dimensionally while the reconstructed areas grow in a layer-by-layer manner. Due to a strong tensile stress of the non reconstructed surface, a reconstruction network is formed by the incorporation of additional Pt atoms into the first layer during deposition, which leads to a decreased mobility of adatoms on the surface and a high island density. The growing islands, though, are not reconstructed and adatoms landing on them have a high mobility. This leads to a natural realisation of the concept of two mobilities.

Ag growing on Ag(111) shows a very different behaviour [6, 11, 18, 19, 20]. For this system, the growth is three-dimensional at all temperatures below step-flow, indicative of a high step-edge barrier.

For the third fcc(111) system studied in detail so far – Cu/Cu(111), conflicting results were reported. A behaviour similar to that of Ag/Ag(111) has been observed by Dastoor and co-workers [21], whereas a behaviour similar to that of Pt/Pt(111) was found by Henzler and co-workers [11, 22, 23].

The first part of this chapter (sec. 2.3) is devoted to the investigation of the conventional homoepitaxial growth on Cu(111), in order to resolve this discrepancy and gain a more general overview on the growth in fcc(111) systems.

The second part of this chapter deals with growth manipulation in the Cu/Cu(111) system, leading to much smoother films than those grown using conventional procedures. Manipulation is based on the "concept of two mobilities" [24, 25] which has been applied previously to the growth of Ag on Ag(111) [18]. In these experiments, an artificially high density of islands is produced during the nucleation stage of each monolayer, such that the typical distance between two such islands is smaller than the "free-diffusion length" of adatoms at the growth temperature and deposition rate used. Adatoms landing from the gas phase on these small islands will therefore reach the edge of the islands much more frequently and the probability of surmounting the barrier and reaching the lower terrace before forming a stable nucleus on top of a pre-existing island is largely enhanced.

Artificially enhanced island density during nucleation was produced in several ways. Sec. 2.4.1 presents the results of experiments where an enhanced island density was produced by lowering the substrate temperature during the nucleation stage of monolayer growth, Sec. 2.4.2 presents the results of experiments in which this aim was achieved by ion bombardment at that stage. An assessment of the quality of the grown layers and of the degree to which the island density must be increased in order to achieve high-quality layers is given.

In addition, Sec. 2.5 presents results of experiments where growth was influenced by pre-exposing the copper surface to molecular oxygen. This procedure results in an (imperfect) layer-by-layer growth of several monolayers. A mechanism for the influence of oxygen is proposed.

2.2 Experimental set-up

The experiments described in this chapter were carried out in an ultra-high-vacuum (UHV) chamber with base pressure below $2 * 10^{-11}$ mbar. The transfer-width at the experimental conditions was ≈ 420 Å [28]. The scattering apparatus was also equipped with an Auger electron spectrometer (AES). Sample temperature was measured using a Ni-CrNi thermocouple inserted into a cavity in the crystal. The Ni-CrNi thermocouple was calibrated at low temperatures by thermal desorption spectroscopy of the multilayer desorption peak of Ar and Xe from the Cu crystal [29].

The sample is a high quality Cu(111) single crystal with a miscut angle $< 0.1°$. It was cut by spark erosion, then carefully polished and in a first step cleaned of sulphur and carbon by glowing in a hydrogen atmosphere at 1100 K. The sample was prepared in UHV by repeated cycles of sputtering with 1.2 keV Ne^+-ions and annealing to 1000 K. This procedure was repeated until no contamination could be detected by means of AES and the He reflectivity from the surface was high. The estimated mean terrace width on the surface was over 1000 Å[1].

After each deposition experiment, the initial conditions were recovered by sputtering and annealing to 850 K.

Copper was evaporated onto the sample from a high purity Cu disk which was thoroughly desulphurised and out-gassed. A home made electron bombardment evaporator was used. During deposition the pressure stayed below $1 * 10^{-10}$ mbar. The deposition rate was determined from the frequency of He intensity oscillations under conditions where layer-by-layer growth was obtained.

The specularly reflected He beam under in- or anti-phase conditions was recorded in-situ during deposition.

Mean island separations were estimated from the broadening of He peak profiles under anti-phase conditions [30, 31]. Peak profiles were recorded by changing the angle of the sample with respect to the detector after quenching the sample temperature to 200 K following deposition.

Oxygen experiments were carried out using molecular oxygen 4.8 which was let in through a leak valve. Partial pressures up to a maximum of $2*10^{-7}$ mbar were used. Immediately after dosing of oxygen, the original base pressure was re-established.

[1]Mean terrace widths were estimated by comparing the reflected He intensities under in- and anti-phase conditions. An estimate of the average terrace width $\bar{\Delta}$ is given by

$$\bar{\Delta} = \frac{\lambda_{He}}{\Delta\vartheta_i} \times \left[\sqrt{\left(\frac{1+\cos^2\vartheta_i}{2}\right)^2 + \cos^2\vartheta_i \left(\left(\frac{I^{in}}{I^{anti}}\right)^2 - 1 \right)} - \frac{1+\cos^2\vartheta_i}{2} \right]^{-\frac{1}{2}}$$

where λ_{He} is the wavelength of the He-beam, $\Delta\vartheta_i$ is the full width at half maximum (FWHM) of the direct He-beam, ϑ_i is the diffraction angle under in-phase conditions, I^{in} and I^{anti} are the reflected He-intensities under in- and anti-phase diffraction conditions [28].

2.3 Conventional Growth of Cu/Cu(111)

The normalized specularly reflected He intensities under anti-phase diffraction conditions ($S = 2.5$) were recorded for different substrate temperatures as a function of deposition time. Deposition was carried out at a rate of $R = 0.006$ ML/sec for all temperatures. The results are shown in Fig.2.1.

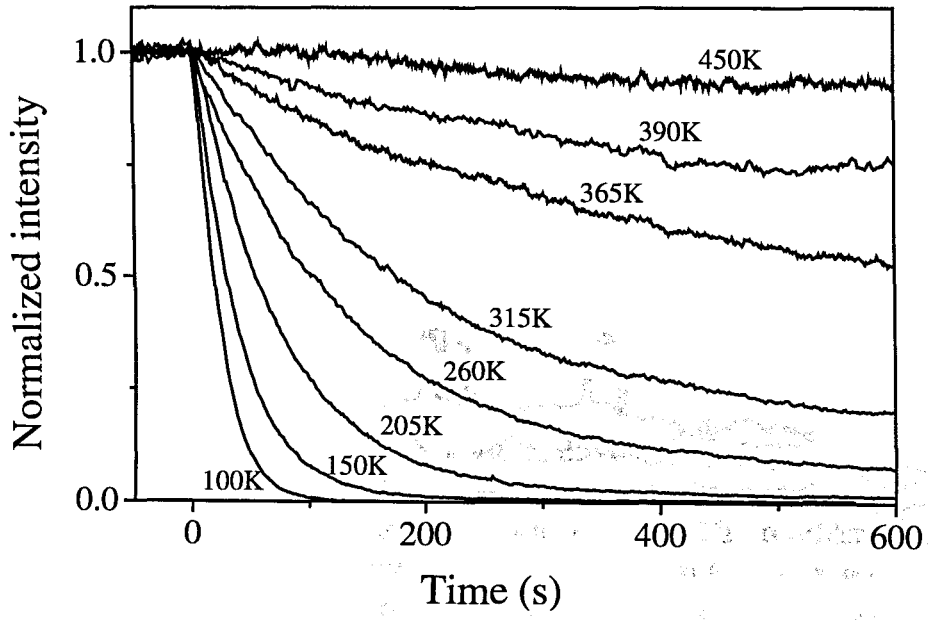

Figure 2.1: Evolution of the normalized specular He intensity under anti-phase conditions ($S = 2.5$) during deposition of Cu onto Cu(111) at different substrate temperatures, as indicated. Deposition was carried out at a rate of $R = 0.006$ ML/sec.

For the highest temperature chosen ($T = 450$ K), the intensity remains about constant during deposition. This indicates growth by step-flow. At this high temperature the mobility of the adatoms is high enough, such that all adatoms landing on the pre-existing terraces diffuse to the ascending step edges, where they are captured before they nucleate. Hence, no nucleation of islands is taking place on the terraces and the film grows via propagation of the pre-existing steps [2]. The onset temperature of ideal step-flow growth is not an intrinsic property of the material. It is also determined by the average terrace width of the surface and hence the crystal surface quality.

[2]The slight decay of the anti-phase He intensity during deposition at 450 K may be attributed to kinetic roughening of the pre-existing steps in the step-flow growth mode or by three-dimensional growth on exceptionally large terraces.

At lower temperatures the intensity falls monotonically during deposition, typical for 3D growth. Note that for the curve obtained at 100 K, the rate of decay is steeper than that expected for ideal 3D growth (see equation 1.7). This is due to diffuse scattering from small structures as will be discussed at the end of this section. Between the two extremes, 3D growth at low temperatures and step-flow at high temperature, a gradual transition is found.

None of the curves displays oscillations of the intensity during deposition. This indicates that growth does *not* proceed in a layer-by-layer fashion at any temperature. The fact that the intensity decays monotonically even at elevated temperatures (> 300 K), i.e., 3-dimensional structures are formed, shows that interlayer mass transport is considerably hampered by the existence of a barrier for downward diffusion over a step edge.

The high temperature oscillations observed for Cu/Cu(111) with SPA-LEED (T = 370 K,R = 0.8 ML/min and 3 ML/min) [11, 22, 23] could not be reproduced in our He scattering experiments. It is unlikely that the discrepancy is due to differences in the average terrace width, as both surfaces were of similar quality. It is also not likely that the different transfer widths of the two diffraction techniques (about 400 Å for TEAS and 1000-2000 Å for SPA-LEED) is responsible for the contradicting results. The very pronounced oscillations observed in the SPA-LEED experiments should have been observable also with He scattering. In addition, simple SPA-LEED experiments with our crystal did not show intensity oscillations under the conditions used in ref. [11, 22, 23]. The reported oscillations were found to be accompanied by a widening in SPA-LEED anti-phase peak profiles taken from the surface during growth with respect to peak profiles recorded during growth at lower temperatures [33]. The structures growing during the high-temperature oscillations are thus smaller than structures growing at lower temperatures. Such a behaviour is not expected on the basis of nucleation theory [34, 35] and can therefore not be explained by simple homogeneous nucleation. Neither our TEAS nor SPA-LEED experiments showed signs of such smaller structures.

In the light of our observations, it seems that a high step-edge barrier is in general a common feature of the (111) face of fcc noble metals, as both Cu(111) and Ag(111) [6, 11, 18, 19, 20] grow three-dimensionally for all temperatures below step-flow, and Pt(111) grows in the same mode for a wide temperature range [7, 8, 9, 10]. The 2D growth of Pt(111) at higher temperatures seems to be an exception which can be traced back to the reconstruction of the Pt surface. The reconstruction network reduces the mobility of adatoms on the surface and leads to an enhanced density of nuclei during the early stages of each monolayer growth [16, 17]. In the absence of this reconstruction, also Pt grows 3D at high temperatures [17].

Recently, also density functional theory calculations by Yu and Scheffler [32] for silver also show, that no step edge barrier is present at steps on the Ag(100) surface, while a substantial step edge barrier hinders mass transport over step edges on the Ag(111) surface in agreement with previous experiments.

Like in the homoepitaxial system Ag/Ag(111), no reentrant oscillations could be

found for Cu/Cu(111) with He scattering. In LEED measurements, though, low-scale reentrant oscillations were observed at low temperatures [11]. The oscillations were of very low amplitude (e.g. for a surface temperature of 172 K and a deposition rate of $R = 0.03$ ML/sec, the amplitude of the first and highest oscillation is 0.005 of the initial LEED intensity [33]). At these low temperatures we find a strong decay of the in-phase He intensity during growth, indicating a substantial diffuse scattering from small structures on the surface. This strong diffuse scattering causes an additional damping of the anti-phase He intensity, which could lead to a lower sensitivity of TEAS to such small oscillations. A reduced sensitivity of TEAS to low temperature oscillations was encountered for several other systems. RHEED oscillations during low-temperature growth of Ag/Ag(100) [6] and Cu/Cu(100) [3] are much more pronounced than the equivalent TEAS oscillations for these systems [36, 37], whereas the high temperature oscillations are of equal quality. The discrepancy between LEED and TEAS measurements at low temperatures are most likely due to this effect.

Nevertheless, even if low-scale reentrant oscillations are present, it is clear that neither Cu/Cu(111) nor Ag/Ag(111) displays such pronounced reentrant oscillations as Pt/Pt(111) does, where the amplitude of the first oscillation is 0.5 of the initial He intensity [7]. The existence of the reentrant layer-by-layer growth mode in Pt/Pt(111) was explained by a transition in the island shapes from compact at higher temperatures to dendritic at low temperatures. However, such a transition in island shapes is present also in Ag/Ag(111) [18] and in Cu/Cu(111), as will be shown at the end of this section. This indicates that a transition in island shape alone is not a sufficient condition for the occurrence of reentrant layer-by-layer growth. The behaviour of Pt/Pt(111) also at low temperatures seems to be the exception rather than the rule. Simulations point out that the reentrant layer-by-layer growth on Pt(111) may be promoted by an exceptionally low barrier for an exchange process at kink sites, leading to efficient interlayer mass transport at irregularly-shaped islands [38, 39]. A series of corrected effective medium (CEM) calculations for the three systems [40, 41] indicated that for Pt adatoms diffusing on Pt(111) the potential energy barrier for interlayer diffusion by an exchange mechanism at the edge of small (10-60 atoms) compact islands is actually lower than the barrier for terrace diffusion, whereas for Ag/Ag(111) and Cu/Cu(111) the situation is reversed. Both calculations emphasize the importance of a diffusion behaviour unique to Pt/Pt(111) in the occurrence of the pronounced reentrant layer-by-layer growth mode for Pt/Pt(111). The exceptionally low barriers for diffusion by exchange are in accord with the tendency of the Pt(111) surface to reconstruct by adatom incorporation into the topmost surface layer.

To complete the study on the unmanipulated growth of Cu/Cu(111) we investigate the annealing of structures obtained by growth at low temperatures. First, 0.1 ML were deposited at 100 K with a rate of $R = 0.006$ ML/sec. At this low coverage the islands would be predominantly two-dimensional, even in the presence of a high barrier for interlayer mass transport. Following deposition the substrate

was heated at a constant rate of 10 K/min while monitoring the in- or anti-phase He intensity. The resulting intensities, normalized to unity before deposition and corrected for Debye-Waller effects [3], are shown as a function of temperature in Fig.2.2a.

At about 200 K, both in- and anti-phase intensities start to increase until at about 250 K a plateau is reached, which indicates that a first annealing step has taken place. Around 350 K the onset of a second annealing step is observed: both intensities rise again and at $\approx$ 400 K the initial intensity values corresponding to a freshly prepared surface are reached. A similar behaviour has already been observed for Ag/Ag(111) (see Fig.2.2b), and the two steps have been interpreted as a transition in the island shape from dendritic to compact and two-dimensional Ostwald ripening, respectively [18]. Here we will look in more detail to these annealing steps and try to substantiate this interpretation.

The two annealing steps are essentially different processes. This is evident from the fact that during the first (lower temperature) step the increase of the in-phase intensity is much larger than that of the anti-phase intensity, while during the second step the situation is reversed.

The intensity behaviour during the first annealing step is in accord with a transition in island shape. The strong rise of the in-phase intensity is expected if dendritic islands which give rise to strong diffuse scattering collapse to a compact shape with straight edges. The anti-phase intensity, on the other hand, is more sensitive to the layer distribution on the surface. It does not increase much during the first annealing step, but does so during the second. The second annealing step can thus be identified as two-dimensional Ostwald-ripening, where larger islands grow at the expense of small ones, which decompose. This ripening process is completed when few very large islands have formed or, on a real surface, when all material on the terraces has been captured by the pre-existing step edges. The surface thus becomes effectively a one-layer system within the transfer width.

To verify the origin of the first annealing step, anti-phase He peak profiles were recorded during annealing. The profiles consist of a central spike and a broadening [30, 31]. From the shape and width of the broadening a characteristic length scale of the growth structures can be obtained. For compact two-dimensional islands the characteristic length is the mean island separation. For dendritic islands intra-island correlations strongly influence the broadening so that the observed length scale is smaller than the island separation. The characteristic length scales during the various stages of annealing are shown in the inset of Fig.2.2a. A clear rise of the length scale can be seen between 300 and 400 K corresponding to two-dimensional Ostwald-ripening. Between 100 and 300 K however, the length scale increases only slightly from $\approx$ 150 to $\approx$ 300 Å. Assuming that during the first annealing step the island shape remains the same, this slight change in the characteristic length could

[3] For correction of Debye-Waller effects, the reflectivity at a given temperature before deposition and during annealing was divided by the reflectivity of a freshly prepared sample at that temperature.

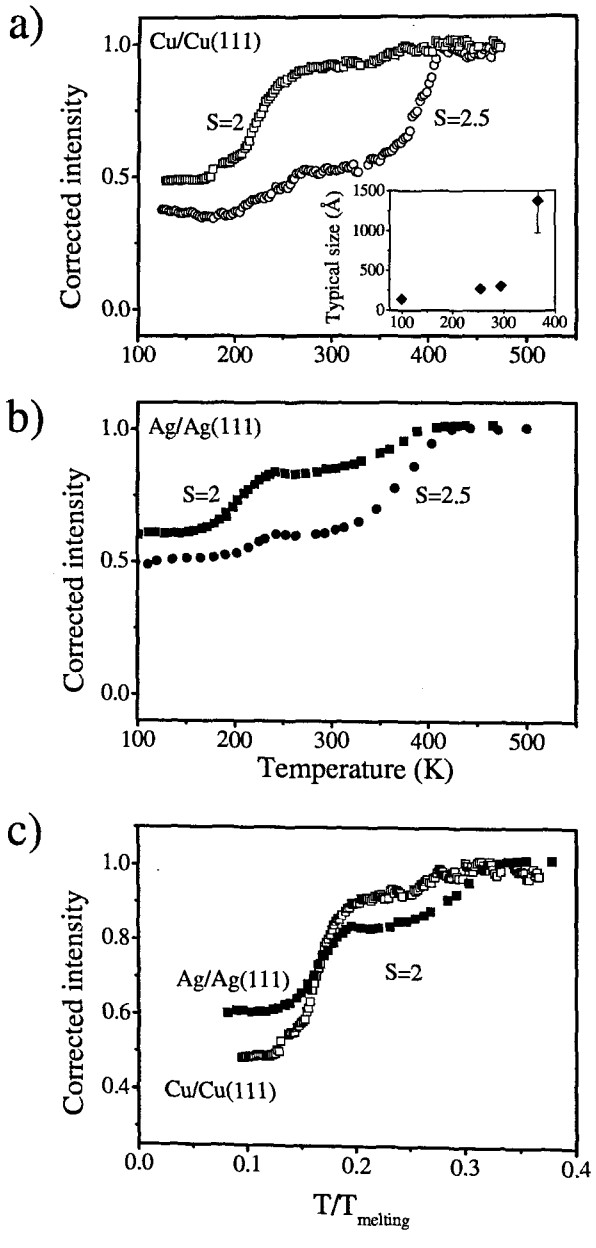

Figure 2.2: Debye-Waller corrected in-phase $S = 2$ (squares) and anti-phase $S = 2.5$ (circles) intensities during annealing of 0.1 ML Cu (hollow symbols) deposited onto Cu(111) and Ag (filled symbols) deposited onto Ag(111) at 100 K, as a function of substrate temperature during annealing. The typical sizes of the Cu structures on the surface during annealing are shown in the inset of a). Sizes were evaluated from the broadening of anti-phase peak profiles. The given error bar represents the error resulting from fitting the peak profiles. For the low temperatures the error is smaller than the symbol.

by no means explain the steep rise in the in-phase intensity (see Fig.2.2a). The

change of length scale alone, not accompanied by changes of the island shape, would result in a rise of only ≈ 0.1 in the normalized in-phase intensity, using equation 1.2. Hence the shape of the islands must have changed during the first annealing step. Similar arguments hold for Ag/Ag(111).

The transformation of shape is also indicated in experiments by Meyer and co-workers [42], although the data were not interpreted in this way originally. These authors studied growth of multilayer films of Cu on Cu(111) using SPA-LEED. For growth below 185 K they observed a rotational symmetry of the anti-phase SPA-LEED peak profiles, which is typical of irregularly shaped islands. Growth at higher temperatures leads to peaks of six-fold symmetry indicating compact islands with straight edges. Although the situation during growth and annealing is not the same, the transition from dendritic to compact islands is determined in both cases by the onset of edge diffusion. Adatom evaporation from islands, necessary for two-dimensional Ostwald-ripening, sets in at higher temperatures.

We also performed Monte Carlo simulations of the annealing of dendritic islands to qualitatively verify the interpretation of the experimental data. The simulation program was especially designed to allow the fast simulation of diffusion processes over time scales[4] equivalent to the time scales found under experimental situations [43]. As input parameters for the simulations, the microscopic diffusion barriers calculated by Stoltze et al. [44] were used. In a first step, the deposition of 0.05 ML of Cu at 140 K was simulated on a 512x512 grid of periodic boundary conditions, resulting in dendritic islands (see Fig. 2.3a). Then, the annealing was simulated by slowly increasing the substrate temperature (5K/sec) and allowing diffusion of the adatoms according to the specific diffusion barriers. Besides the configuration of the simulated surface, also the step length and total island number was generated as output and are depicted in Fig. 2.3e. Indeed, also the simulations show an annealing in two steps at roughly the same temperatures as the experiment, as can be seen from the step length as function of temperature in Fig. 2.3e. Below 200 K, the structures are stable on the time scale of the simulations. Then, in a first annealing step between 200 and 250 K, the dendritic islands contract to a compact shape (see Fig. 2.3b) and the total step length decreases strongly. During this contraction, occasionally also new islands are created by a breaking up of a large dendritic islands into several parts, explaining the small initial rise in the total number of islands. The first annealing step is followed by a plateau in the step length were the morphology varies only little. Only exceptionally small islands, either created by breaking up of dendritic islands or by late nucleation during growth, dissolve resulting in compact islands of similar size on the surface (see Fig. 2.3c). In the second annealing step slowly starting around 300 K, major Ostwald ripening sets in and the smaller compact islands decay by evaporation of atoms onto the terrace while the larger ones grow by capturing adatoms. So the total amount of islands decreases, especially above 320 K, while the step length on the surface

[4]The link between simulated time and experimental time was done by assuming the same attempt frequency $\nu_0 = 10^{13}$Hz for all diffusion processes.

falls only slightly. The resulting configuration of a small number of large islands is shown in Fig. 2.3d. Hence, the simulations further verify an annealing process in two steps. Surprisingly, the consistency with the experiment is better than this. Even the onset temperatures of the different annealing steps coincide well with the experiment, showing that the microscopic barriers calculated by Stoltze et al. are quite reliable.

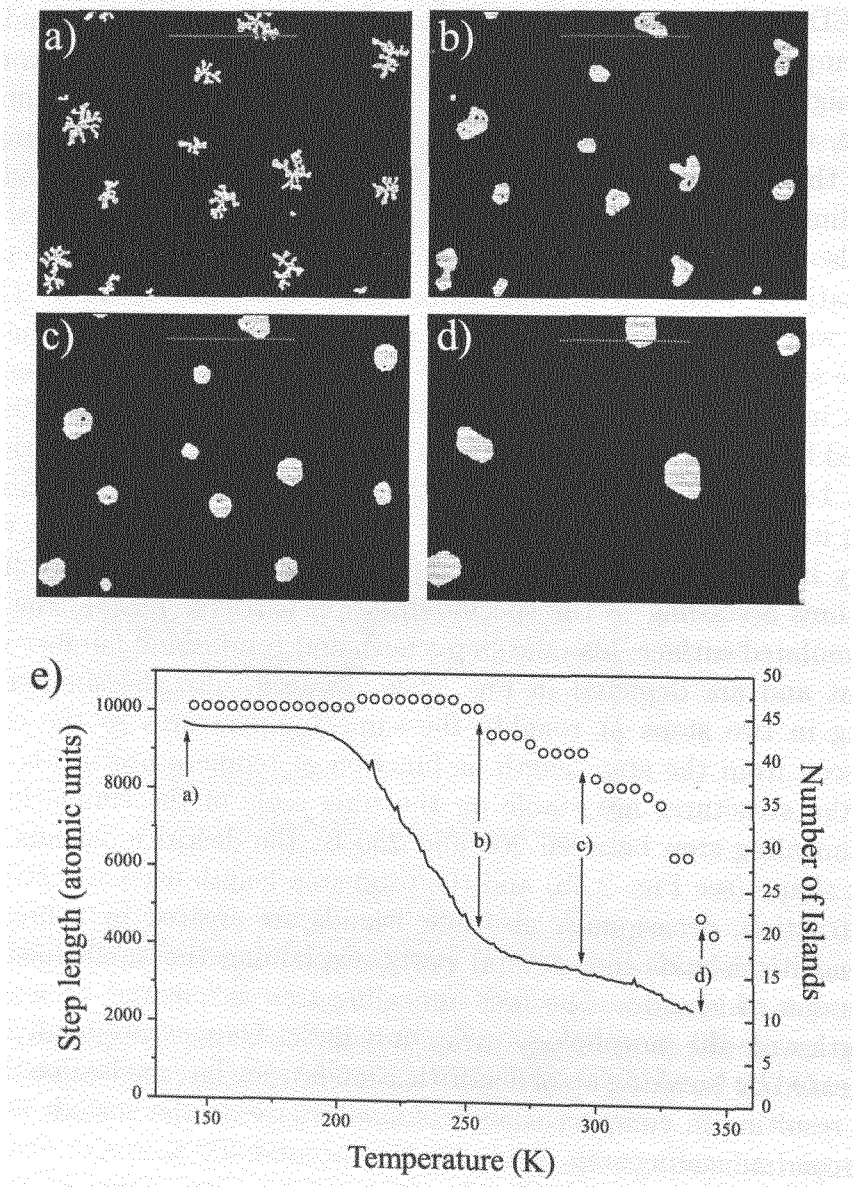

Figure 2.3: Simulated dendritic islands during annealing. a) 140 K, b) 255 K, c) 295 K d) 345 K. e): total step length (line) and island numbers (circles) during simulated annealing.

In summary, a two step annealing process was observed. During the first step, edge diffusion becomes active and the island shape changes from dendritic to compact. During the second step, adatoms can evaporate from islands leading to two-dimensional Ostwald-ripening.

Comparing the in-phase annealing data of Cu/Cu(111) to those obtained for Ag/Ag(111) (see Fig.2.2c), one finds that the temperatures where the first and second annealing steps take place scale approximately with the melting temperature ($T^{Ag}_{melting}$ = 1234K, $T^{Cu}_{melting}$ = 1356K). This is expected on the basis of "rule of thumb" argumentation for bond-breaking processes on the surface.

Such a "rule of thumb" scaling of activation energies is more or less confirmed by effective medium theory (EMT) calculations for Ag(111) and Cu(111) [44]. There is, however, one exception: the energy barrier for adatom diffusion on a flat terrace is found to be lower on Cu(111) than on Ag(111). Interestingly, we arrive at the same conclusion from our data, if we assume that during the first annealing step the island density remains indeed unchanged. As it is unlikely that the cross-section for diffuse scattering is much different for the two systems, the higher in-phase intensity after the first annealing step in Fig.2.2c for Cu(111) indicates a lower island density, and hence, a higher adatom mobility. This is not contradicted by the fact that the intensity directly after deposition, i.e., before the first annealing step, is lower for the Cu system: edge diffusion on Cu(111) does have a higher energy barrier than on Ag(111), such that the islands are expected to be more ramified leading to more diffuse scattering.

Terrace diffusion on Cu(111) seems to be exceptionally effective. For example, an estimate of the size of the structures resulting from growth at 300 K obtained by comparing in- and anti-phase intensities at 0.5 ML coverage, results in a mean terrace width of $\approx$ 600 Å. The 3-dimensional islands that grow at room temperature must therefore have a typical separation of over 1200 Å, corresponding to only one island per average terrace width of the substrate.

An estimate for the diffusion energy can be obtained from an analysis of the island density as a function of temperature, based on nucleation theory [34, 35]. In the case where the dimer is the smallest stable nucleus, the island density n is given by $n \propto \exp\left(\frac{E_d}{3kT}\right)$ where E_d is the diffusion energy, k the Boltzmann factor and T the temperature. Under the same assumption as above, i.e., an unchanged island density after the first annealing step, the island density can be obtained by evaluating peak profiles taken from surfaces onto which submonolayer amounts of Cu are deposited, followed by annealing beyond the first annealing step to make the islands compact. Fig.2.4 shows an Arrhenius plot of the island number density obtained in this manner as a function of temperature in the range 55 to 140 K. 0.1 ML Cu were deposited at the temperatures indicated, followed by annealing to 273 K and additional deposition of 0.2 ML at that temperature. The additional material deposited at the higher temperature diffuses to pre-existing islands and is therefore not likely to change the island-density. A fit to the four lowest temperatures shown in Fig.2.4, where the dimer is expected to be stable, gives a very low diffusion energy

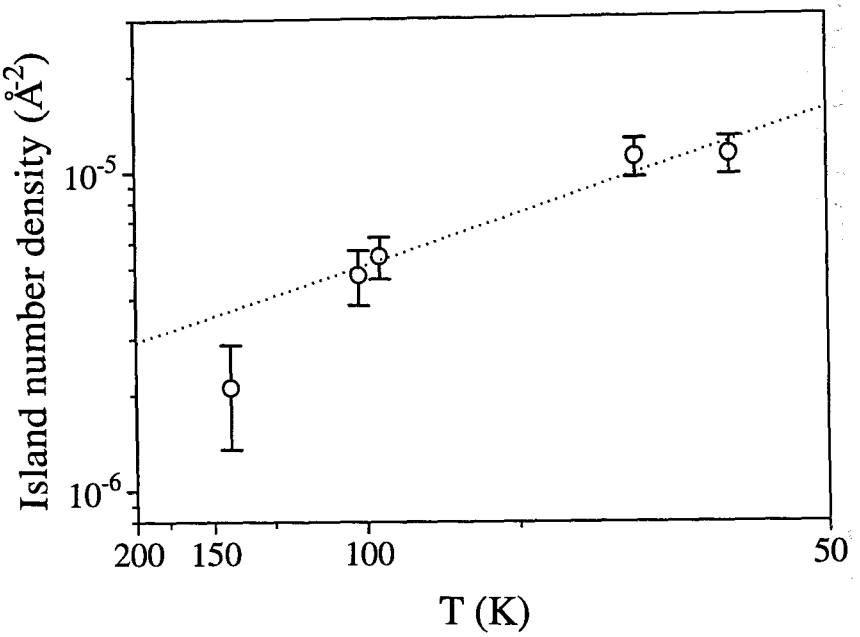

Figure 2.4: Arrhenius plot of the mean island density as a function of temperature for Cu islands grown on Cu(111). Deposition was carried out at a rate of R = 0.006 ML/sec.

of 30^{+10}_{-5} meV. This low value is in accord with calculations for terrace diffusion barriers for Cu/Cu(111) (40 meV [41]; 53 meV [44]). Nevertheless, the measured value is surprisingly low. It is possible that, in contrast to our assumption, some Ostwald ripening does take place during the annealing to 273 K, particularly for very small islands (dimers/trimers) [5] or very ramified islands. The diffusion barrier might therefore be somewhat larger than this value.

2.4 Manipulation of Growth in Cu/Cu(111)

A few monolayers of Cu deposited onto Cu(111) at room temperature form a film composed of large-scale ($\approx$ 600 Å) structures several monolayers high. The multilayer growth is due to the high probability that Cu atoms landing on top of islands will nucleate to form a higher layer before they can surmount the energy barrier at the island edge and fill the lower one.

The growth manipulation procedures described in the following are aimed at reducing the probability for nucleation on top of existing islands. These proce-

[5] Since edge diffusion is active at 273 K, also some loss of very small islands may be due to some mobility of these islands caused by edge diffusion.

dures intervene with the nucleation stage of each monolayer, such that the mean distance between the nucleating islands is smaller than the distance which would have evolved naturally under the conditions prevailing during the further stages of monolayer growth. Once nucleation is achieved, intervention is stopped, and growth proceeds further undisturbed. The mean distance which an adatom can traverse during the later stages of monolayer growth before it collides with other adatom(s) to form a stable nucleus is thus larger than the mean distance between the islands formed during the nucleation stage. Adatoms landing on top of these islands prior to coalescence can therefore reach the edge of the island much more frequently, and the probability that they surmount the step edge barrier and fill the lower layer (2D growth) before nucleating to form a higher one (3D growth) is greatly increased.

2.4.1 Growth Manipulation via Temperature Alternation

In this procedure, an increased island density is achieved by decreasing the substrate temperature during the nucleation stage. According to nucleation theory [34, 35], the mean island separation shrinks (at least) exponentially with decreasing temperature. A reduction of the temperature during the nucleation stage therefore reduces the mean island separation quite effectively.

After nucleation, the temperature of the substrate was increased, and subsequent growth was carried out at 300 K. As this temperature lies below the onset of major Ostwald-ripening, the island density created at the nucleation stage is not much affected by coarsening during heating.

Figure 2.5 shows the evolution of the anti-phase He intensities during a series of growth experiments of Cu on Cu(111) at 300 K, on surfaces which were prepared by pre-deposition of 0.05 ML Cu at lower temperatures between 200 K and 100 K as indicated. The plot on the leftmost panel of Fig. 2.5 is the result obtained during conventional growth, i.e., where the temperature during nucleation and subsequent growth was the same. The starting intensity of all plots was normalized to the intensity reflected from a freshly prepared surface at 300 K.

From the series of results shown in Fig. 2.5 it is clear that the features indicative of layer-by-layer growth, namely the decrease of the specularly scattered intensity upon deposition of 0.5 ML and its rise towards the completion of a monolayer develop gradually as the pre-deposition temperature is lowered.

The 1 ML film grown on a surface which was prepared by pre-deposition at the lowest temperature, 100 K, is quite flat. The anti-phase scattered intensity after deposition of a full monolayer corresponds to the first layer being more than 95% filled, using equation 1.4 and assuming a three-layer system (substrate, first layer and second layer) and an ideal instrument. Thus the growth is almost ideal layer-by-layer. This indicates that the length scale imposed during the nucleation stage at this low temperature is small enough to almost completely suppress nucleation on top of the pre-existing islands during growth at 300 K and ensure effective interlayer mass transport.

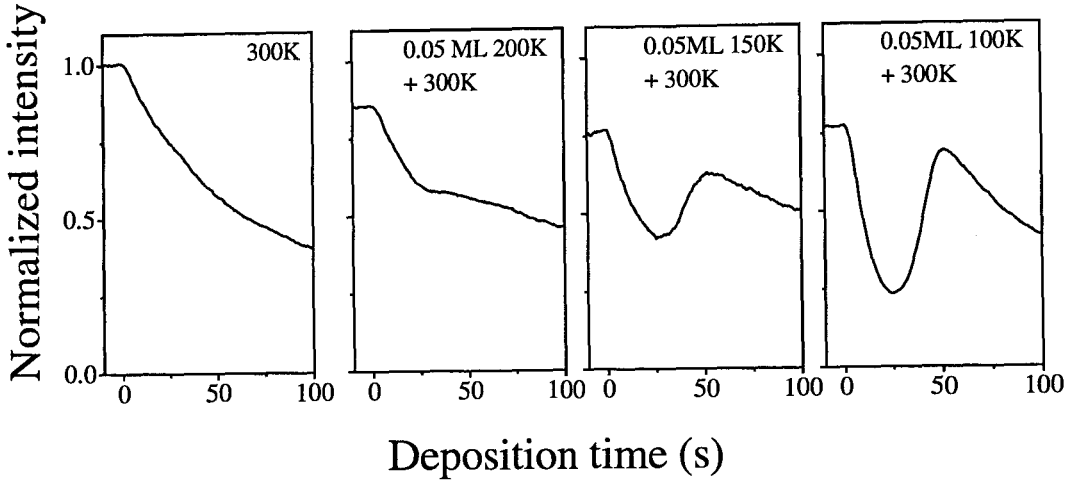

Figure 2.5: Evolution of the normalized anti-phase He intensities during deposition of Cu at $T = 300$ K onto Cu(111) surfaces, which were treated by pre-deposition of 0.05 ML Cu at lower temperatures as indicated. Deposition was carried out at a rate of $R = 0.02$ ML/sec.

The quality of the layer deposited at 300 K deteriorates with increasing pre-deposition temperature, as is evident from the decrease in the height of the intensity maximum upon 1 ML deposition. This deterioration reflects the fact that as the length scale imposed during nucleation increases, the islands are no longer small enough to completely suppress nucleation on top of them prior to coalescence.

The mean island separation for a film grown at 300 K after pre-deposition at 100 K inferred from an analysis of the peak profile under anti-phase diffraction conditions, as well as from a comparison of the in- and anti-phase scattering intensities, is $\approx$ 430 Å. This length being of the same order as the transfer width of our instrument, is the origin of the fact that the anti-phase intensity after deposition of 0.5 ML is higher than zero. This latter consideration would modify our estimate for the degree of completion of the first layer after deposition of 1 ML only slightly, since at this coverage small changes in the intensity are only mildly expressed in the layer distribution. The length scale obtained for growth subsequent to pre-deposition at 100 K corresponds to an increase of the island density by a factor of at least 8 with respect to the unmanipulated growth at 300 K. It must be kept in mind, though, that unmanipulated growth at 300 K on our surface leads to structures of the order of the terrace width. Island sizes may thus be limited by the mean terrace width on

the surface. The island density enhancement factors may therefore be larger with respect to unmanipulated growth on a "perfect" surface.

2.4.2 Growth Manipulation via Ion Beam Pulses

A second and more convenient way of creating an artificially high density of nuclei is to bombard the surface with ions prior to or during the first stages of deposition. During bombardment, the surface is not only sputtered, but also adatoms are created due to displacement of atoms by collisions and upward diffusion of bulk interstitials. These so called "target" adatoms have been directly observed with STM for Pt(111) [45, 46, 47], for Ag(111) [25] and for Cu(100) [48, 49]. At temperatures high enough to allow adatom diffusion, the adatoms created in direct vicinity to the ion impact site form one or several adatom islands close to the impact site [46]. These then serve as nucleation centres during film growth. Fig. 2.6 displays an STM image of such islands close to impact sites of 5 keV Xe^+-ions on Pt(111).

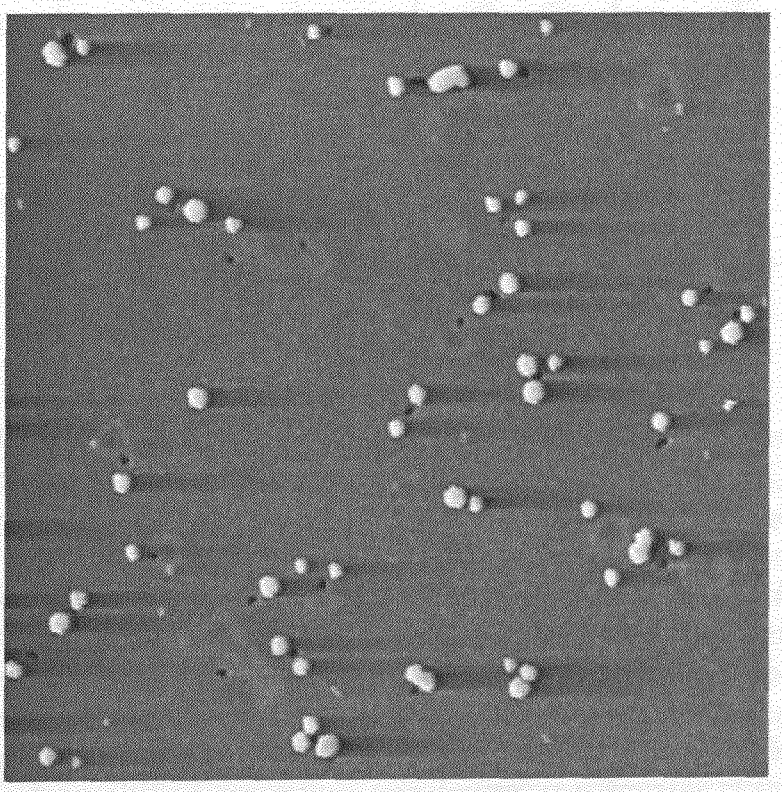

Figure 2.6: STM image of a Pt(111) surface after bombardment with $4.1*10^{15}$ ions/m^2 of 5 keV Xe^+-ions (with kind permission by T. Michely [47]).

Similarly, sputtering of Cu(111) with Ne^+-ions leads to defects on the surface which are used as nucleation centres during manipulated growth. At room temperature, the defects created are metastable and only slowly anneal away, as can bee seen

from a slow recovery of the in-phase He intensity after sputtering towards its original value. The time constant τ of the relaxation is of the size of 10 min at room temperature,[6] easily allowing the application of growth manipulation techniques with typical deposition rates of 1 ML/minute.

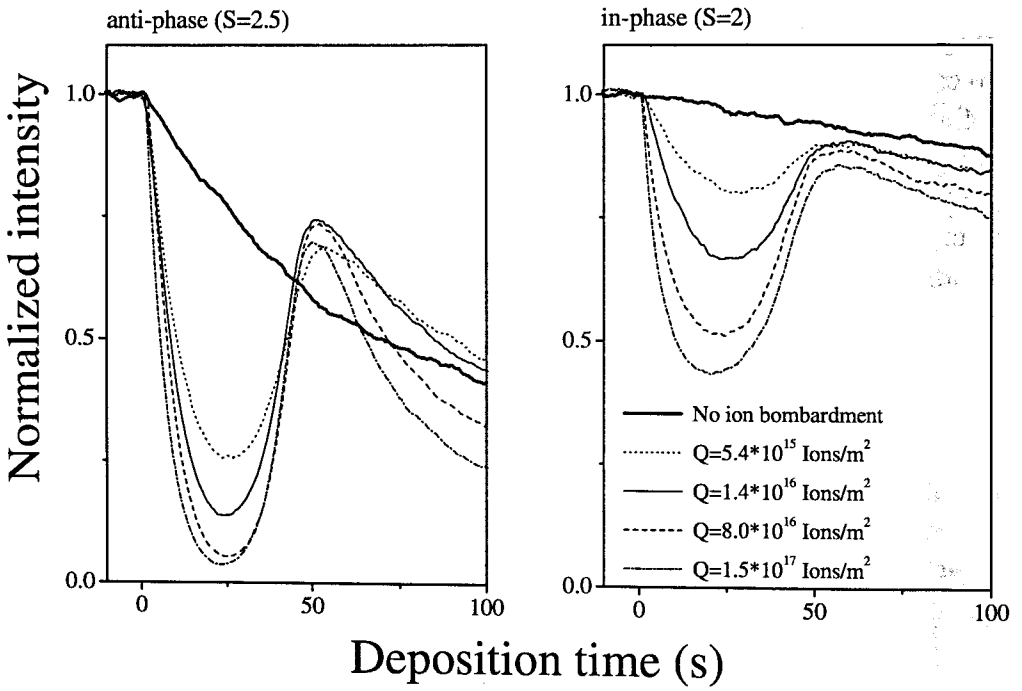

Figure 2.7: Normalized in- and anti-phase He intensities during deposition of Cu at $T = 300$ K onto surfaces which were treated by ion bombardment with fluences as indicated. Deposition was carried out at a rate of $R = 0.02$ ML/sec.

The normalized in- and anti-phase He-intensities recorded during a series of growth experiments at 300 K are shown in Fig. 2.7. In these experiments, the freshly prepared surfaces were bombarded with 1.2 keV Ne^+-ions using fluences Q between $5 * 10^{15}$ and $1.5 * 10^{17}$ ions/m^2, as indicated. These fluences correspond to sputtering of 0.001 to 0.03 ML respectively [7]. The angle of incidence of the ions was

[6]The time constant τ of the annealing of sputter defects shows an Arrhenius behaviour revealing an activation energy of 0.86±0.07 eV. Since soft sputtering leads to a complex structure of vacancies and islands, the energy associated to the annealing is a composition of many different microscopic barriers. However, it gives an upper limit for the sum of the barrier for evaporation of atoms from step edges and adatom diffusion on the terrace.

[7]At 440 K ion bombardment results in layer-by-layer etching causing oscillations of the anti-phase intensity. These oscillations allow to relate the ion fluence to the overall amount of material, that is removed from the substrate. A similar behaviour for Pt(111) [50] and Ag(111) [51] during sputtering has been previously reported.

between 11 and 17° from normal incidence.

Immediately after ion bombardment, Cu deposition was started at a rate of $R = 0.02$ ML/sec. From Fig. 2.7 it is clear that ion bombardment indeed results in the two-dimensional growth of one monolayer for all ion fluences used.

The exact shape of the in- and anti-phase curves varies, however, with the ion fluence. In order to clarify the origin of this variation we took anti-phase peak profiles from surfaces onto which 0.5 ML were deposited after ion bombardment.

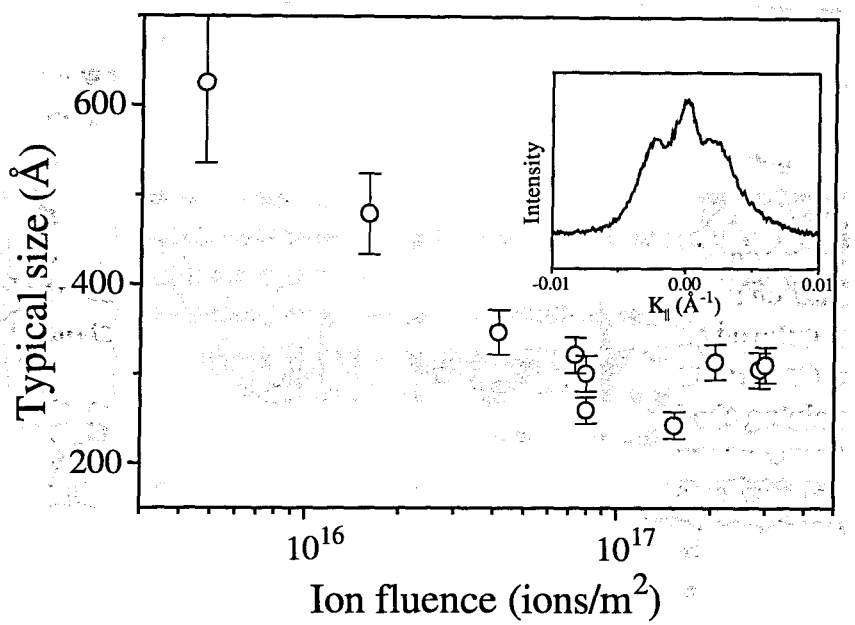

Figure 2.8: Typical structure sizes after deposition of 0.5 ML Cu onto surfaces, which were treated by ion bombardment, as a function of fluence. The sizes were evaluated from the broadening of anti-phase peak profiles, an example of which is shown in the inset. The given error bars represent the error resulting from fitting the peak profiles. Deposition was carried out at a rate of $R = 0.02$ ML/sec.

A typical example is shown in the inset of Fig. 2.8, where the reflected He intensity is plotted versus the momentum transfer parallel to the surface. From the ring-like broadening in the peak profiles, the typical length scale of the structures, i.e., the mean adatom island separation, was derived as a function of the ion fluence. As can be seen from Fig. 2.8, the length scale falls with rising ion fluence until at a fluence of $Q \approx 8{*}10^{16}$ ions/m^2 a saturation in the length scale of ≈ 300 Å is reached. A further increase of the ion fluences by roughly a factor of five does not lead to growth of significantly smaller structures on the surface. An efficient enhancement of the island density under the chosen growth condition requires, therefore, bombarding with an ion fluence of at least $Q = 8 * 10^{16}$ ions/m^2. Lower fluences obviously lead to less effective manipulation of nucleation.

We now return to the detailed examination of the curves shown in Fig. 2.7, starting with the anti-phase curves. For the two lowest fluences ($Q = 5 * 10^{15}$ and $Q = 1.4 * 10^{16}$ ions/m^2) the sizes of the structures are considerably larger than the transfer width. This would explain the rather high anti-phase intensity at the minimum (0.5 ML coverage), even if growth were perfect 2D. At 1 ML coverage, however, the anti-phase intensity for the lowest ion fluence is lower than that for higher ion fluences, indicating that the film is rougher than the others. We conclude that the island density created by bombarding with this low ion fluence is too low in order to efficiently suppress nucleation on top of islands and insure sufficient interlayer mass transport. Increasing the ion fluence leads to smaller structures and the anti-phase intensity at 1 ML coverage increases, indicating a better interlayer mass transport and a more perfect 2D growth. The intensity at the minimum (0.5 ML) decreases with ion fluence both due to the better 2D growth and to the decrease in length scale with respect to the transfer width. For the highest ion fluence shown in Fig. 2.7 ($Q = 1.5 * 10^{17}$ ions/m^2), however, the anti-phase intensity at both 0.5 and 1 ML coverage is slightly lower than the intensity for $Q = 8 * 10^{16}$ ions/m^2. Since this cannot be attributed to a change in length scale, we assume that some ion bombardment induced defects remain in the layer. These defects should be visible also in the in-phase intensity.

When examining the in-phase intensities one notices that, indeed, the intensities at one monolayer coverage and beyond decrease with increasing ion fluence, indicating that the layer contains more defects. As this trend also holds for the higher ion fluences, which give rise to similar island densities, we assume that these defects are not only related to the different morphology of the layers, but contain some contribution from ion bombardment induced defects, which do not anneal even at higher coverage. These defects could either be small vacancy islands created by the sputtering or crystal defects underneath the surface such as implanted neon atoms.

We conclude that bombardment is best done with the minimum ion fluence with which the saturation length scale can be obtained. This ensures that the optimal island density is obtained, while minimizing the amount of residual defects.

Returning to the examination of anti-phase intensity curves beyond one monolayer coverage, one notices that not only the absolute value, but also the *slope* of the decay of the signal varies with ion fluence (or rather with structure size, as it is similar for the two highest fluences). This indicates that there is a difference in morphology of the layers in addition to the different amount of residual sputter defects. Presumably, this has to do with a partial "transfer" of the length scale established in the first layer, to the second one. As the first monolayer is not completely filled upon coalescence, some holes still remain between the islands. The distribution of these holes reflects the characteristic length scale of the first monolayer, which slightly influences the growth of the second layer. This so called "memory" effect was also observed for manipulated growth of Ag on Ag(111) [51].

Assuming an ideal instrument and a three-layer-system, the anti-phase intensity for the ion fluence $Q = 8 * 10^{16}$ ions/m^2 (removal of only 0.016 ML), at 1 ML

coverage corresponds to a filling of the first layer of 96% (using equation 1.4). This result is even better than that obtained by pre-deposition at the lowest temperature. The typical length scale of the structures obtained with this ion fluence gives an enhancement factor of 16 in the island density, which is larger than that obtained by pre-deposition at low temperatures, in accord with the better growth.

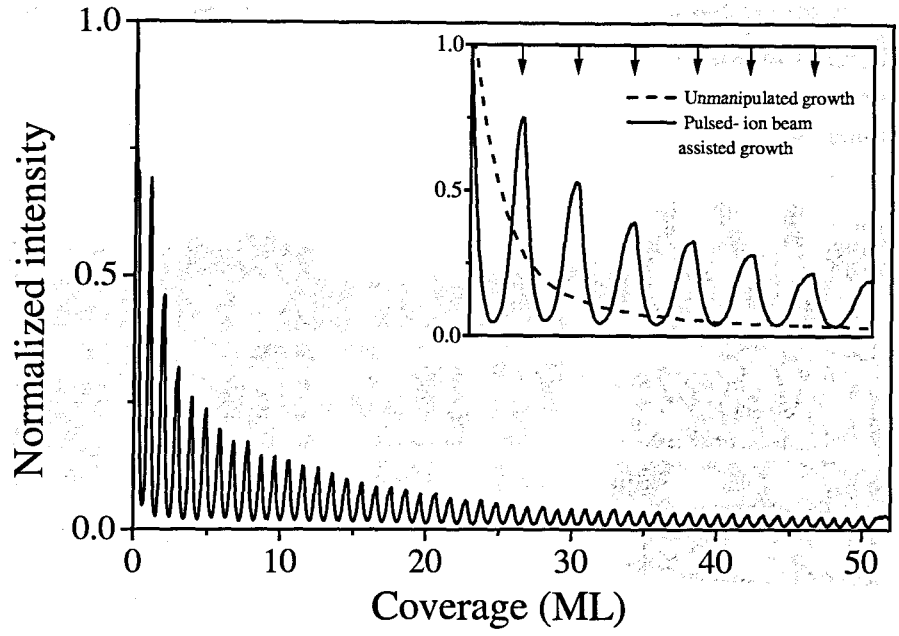

Figure 2.9: Normalized He anti-phase intensity as a function of Cu coverage at $T = 300$ K and a rate of $R = 0.02$ ML/sec. During deposition intermittent ion pulses were given at the initial stages of growth of each layer. The evolution of the anti-phase He intensity during deposition of the first couple of monolayers is displayed in the inset, and compared with the intensity obtained during unmanipulated growth. Ion bombardment is indicated by arrows in the inset.

A comparison of the two growth manipulation procedures – pulsed ion bombardment and temperature alternation – is clearly in favour of the pulsed bombardment procedure, which easily allows higher enhancement factors. Another advantage of this procedure is the easy applicability to the growth of many monolayers. Fig. 2.9 displays the anti-phase He-intensity during deposition of 50 ML copper ($R = 0.02$ ML/sec, $T = 300$ K). Here, an ion pulse was given during deposition just when growth in a given layer started. In this way the island density is enhanced in each layer and the film grows two-dimensionally. The inset in Fig. 2.9 shows in detail the first few oscillations and as a comparison the curve which corresponds to unmanipulated growth with the same growth parameters. It can clearly be seen that the anti-phase intensity upon monolayer completion is higher for the manipulated

growth than for the unmanipulated one even after deposition of a "thick" film. This method therefore enables growth of smooth films many monolayers thick. Similar results were obtained when bombardment was carried out using 600 eV argon ions instead of neon as depicted in Fig. 2.10.

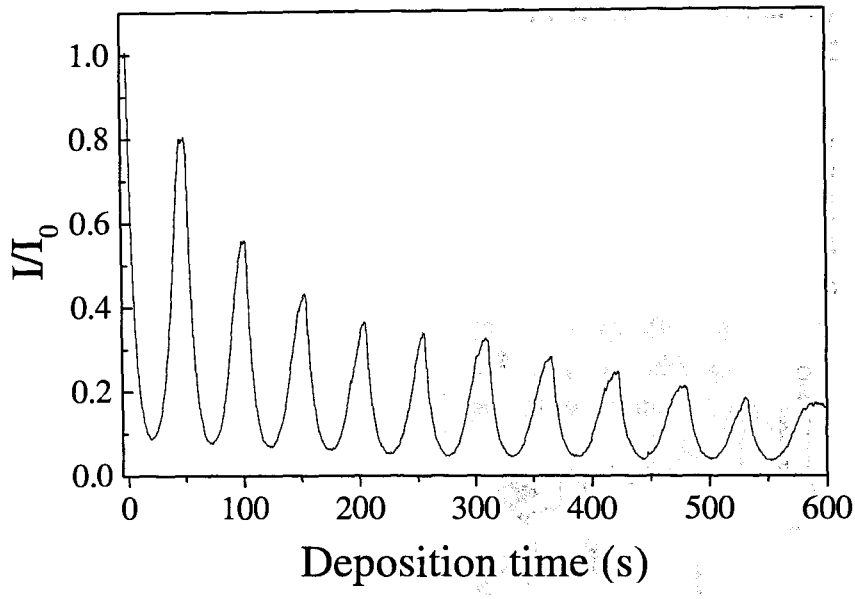

Figure 2.10: Normalized He anti-phase intensity as a function of Cu coverage at $T = 300$ K and a rate of $R = 0.02$ ML/sec. During deposition, intermittent argon ion pulses ($E = 600$ eV) were given at the initial stages of growth of each layer.

2.5 Oxygen mediated Growth

It has long been reported in the literature that the introduction of foreign substances to an epitaxial system can affect the growth mode in hetero- as well as homo-epitaxy [20, 52, 53, 54, 55, 56, 57, 58]. For example, Sb changes the growth mode in the Ag/Ag(111) system from three- to two-dimensional [20].

One of the substances which is known to influence growth in noble-metal and other systems is oxygen [56, 57, 58]. Experiments on the growth of Pt on Pt(111) [56, 57] show that growth in that system is improved when oxygen is used as a surfactant. It was also demonstrated that in the Pt/Pt(111) case oxygen floats up to the highest uncovered layer as deposition is continued. For growth of Pt on Pt(111) it was shown that oxygen influences the growth by reducing the step-edge barrier and thus facilitating interlayer mass transport [57].

Reports on the influence of O_2 on growth of Cu on Cu(111) indicate that exposure to oxygen prior to deposition (pre-exposure) might improve growth in this system also. Dastoor and co-workers [21] observed He intensity oscillations during Cu deposition on Cu(111) at a narrow temperature range around 200 K.

We first concentrate on experiments carried out at 300 K, with different oxygen pre-exposures between 2 and 110 Langmuir. Under our experimental conditions, O_2 is reported to chemisorb on Cu(111) dissociatively, forming a disordered layer [59, 60]. Desorption does not take place at temperatures below 620 K [59]. The oxygen atoms are situated on or within the topmost copper layer [61, 62].

Following low (2 Langmuir) as well as high (110 Langmuir) oxygen exposures no oscillation in He intensity during deposition of copper could be observed. For a limited range of O_2 exposures (≈ 36 - ≈ 72 Langmuir), oscillations as a function of Cu deposition were found.

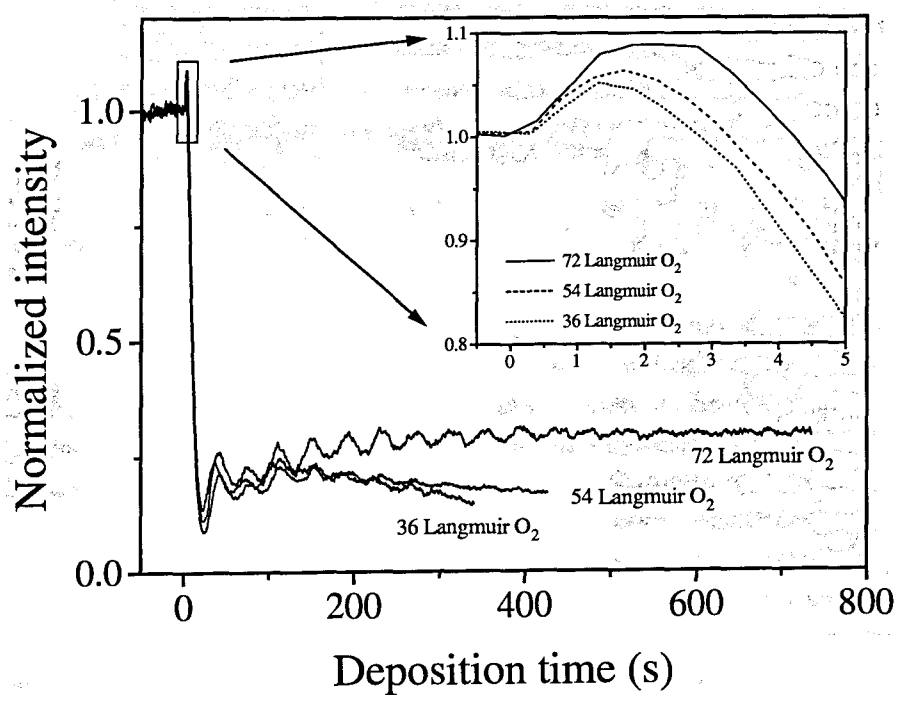

Figure 2.11: Normalized He anti-phase intensity as a function of Cu deposition time at $T = 300$ K onto surfaces which were treated by O_2 pre-exposure as indicated. The initial stages of Cu deposition are shown in detail in the inset.

The main conclusion is that although O_2 pre-exposure does lead to small oscillations in the He intensity as a function of deposition, oxygen is nevertheless quite ineffective in promoting growth of smooth two-dimensional films. Fig. 2.11 depicts the evolution of the $S = 2.5$ normalized anti-phase He reflection during Cu

deposition at 300 K following O_2 exposures as indicated. The main features of the behaviour are a strong decrease in the intensity upon Cu deposition, followed by a couple of minute oscillations, sometimes superimposed on a slight gradual intensity increase. The period of the oscillations, from the second maximum onward is more or less constant and corresponds roughly to monolayer coverage. The best growth is achieved after 72 Langmuir exposure. We estimate the oxygen coverage on the surface following that exposure to be about 5-7% ML from the evaluation of Auger Electron Spectroscopy (AES) data following the procedure in ref. [61].

O_2 exposure was adjusted to obtain He intensity oscillations during Cu deposition at 300 K. When both O_2 exposure and Cu deposition were carried out at either 200 K or 400 K, no oscillations were observed. However, we did observe oscillations during Cu deposition at these temperatures when the pre-exposure of oxygen was done at 300 K. We conclude that the decisive factor is the amount of adsorbed oxygen on the surface, which is strongly temperature dependent.

Two possible principal mechanisms could be responsible for the partially two-dimensional character of the growth. One is a reduction of the step-edge barrier, similar to the case of Pt/Pt(111), the second is a buildup of an increased island density on the substrate due to an oxygen-induced restricted mobility [18, 24]. In both cases monolayer completion should be followed by the oxygen to float up from the lower to the upper layer.

In order to distinguish between the two mechanisms, we exposed to O_2 surfaces onto which 0.05 ML Cu had been pre-deposited at a low temperature (100 K), and examined the subsequent growth at 300 K. Fig. 2.12 shows the results of two such experiments, where the surface was treated by a low (1 Langmuir) as well as by a higher (36 Langmuir) O_2 exposure. These experiments are identical, apart from the O_2 exposure, to the experiments carried out to obtain the result in the right hand panel in Fig. 2.5, which is presented again in Fig. 2.12 for ease of comparison. Had oxygen reduced the step edge barrier, the interlayer mass transport after O_2 exposure would have been much improved due to the combined effect of reduction in the length scale formed by pre-deposition, and the reduced barrier. The resulting layer would have been flatter than the one obtained without O_2 exposure, and the He intensity after deposition of a full monolayer would have been higher. Obviously, this is not the case. The layers grown after O_2 exposure are rougher than the layer grown directly on the surface with pre-deposited islands. We conclude that the oxygen induced oscillations are not a result of a reduction of the step edge barrier.

The alternative mechanism involves reduction in the length scale of the islands formed on the substrate due to a reduced mobility in the presence of oxygen. Evaluation of anti-phase peak profiles at 0.5 ML coverage shows that the length scale of islands formed as a result of deposition in the presence on oxygen is indeed smaller than that formed during unmanipulated growth. The estimated mean island separation at room temperature is about 400 Å.

In order to influence the growth of more than one or two monolayers, the oxygen has to float up during deposition. The oxygen AES signal from the surface after

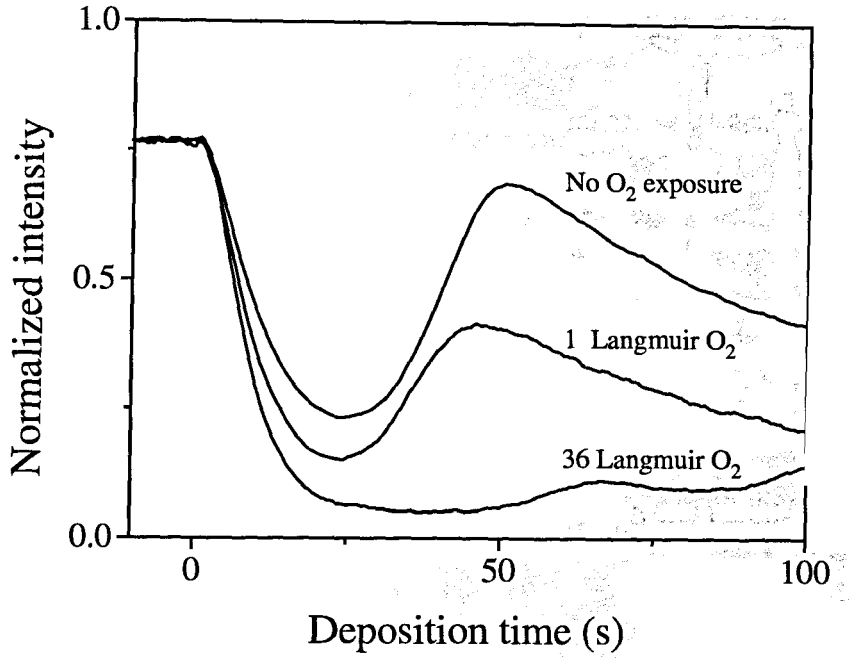

Figure 2.12: Normalized He anti-phase intensity as a function of Cu deposition time at $T = 300$ K. Prior to oxygen exposure and deposition at room temperature 0.05 ML Cu were deposited onto all surfaces at 100 K. The two lower curves were taken from a surface which were additionally treated by 1 and 36 Langmuir O_2 exposure, as indicated.

deposition of 15 ML Cu was found indeed to be identical within the sensitivity of our AES to that obtained from the surface directly after O_2 exposure. We can therefore exclude major incorporation of oxygen into the growing film. AES studies of O_2 mediated growth of Cu on Ru(0001) reveal a similar floating [58].

The two-dimensional aspect of the growth can thus be explained by a restriction of the mobility of Cu adatoms in the presence of oxygen on the surface. This leads to an increase in island density, in a similar manner to the modus operandi of the growth-manipulation techniques discussed in the former sections of this chapter.

A closer look into the details of the deposition curves reveals that the interaction of oxygen with copper and the dynamics of growth during Cu deposition are actually far from being simple. To mention some of the unconventional features: 1) Immediately upon Cu deposition, an increase in the He intensity is observed. The time elapsed until reaching the maximum of this increase is a function of O_2 exposure as demonstrated in the inset of Fig. 2.11. This was also observed by Dastoor and co-workers [21]. 2) The period of the first oscillation is smaller than that of the subsequent ones. 3) The amplitude of the second oscillation is lower than that of the others. 4) The first maximum is totally missing when depositing on surfaces

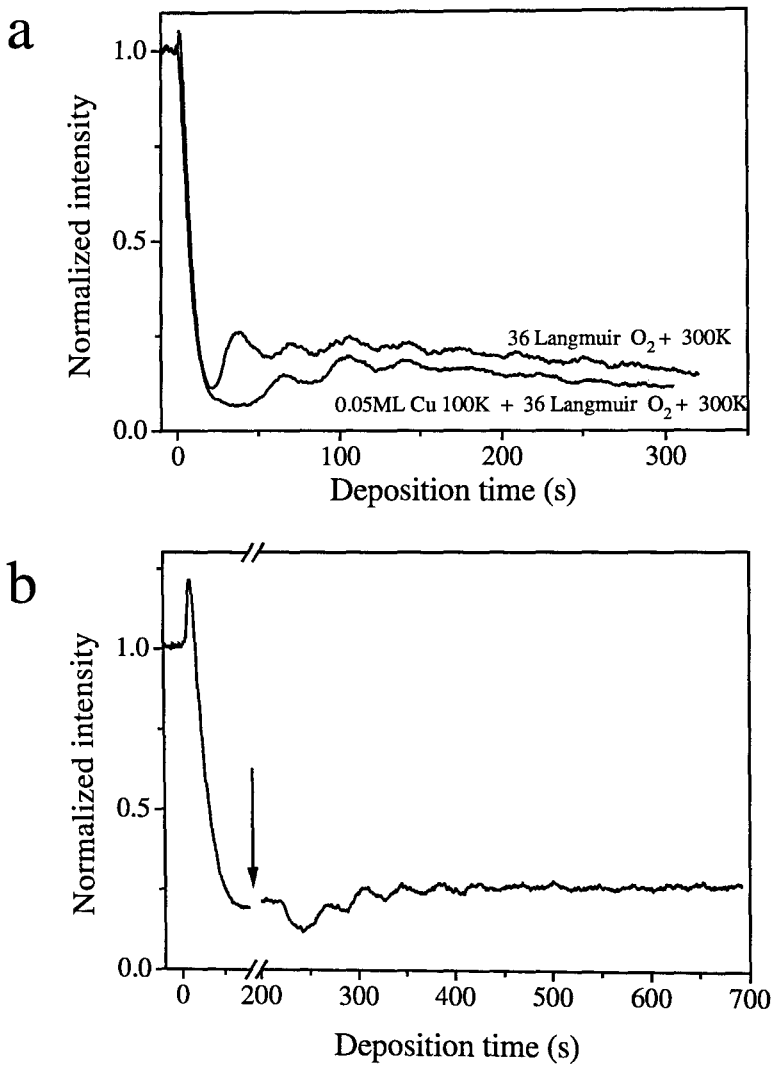

Figure 2.13: a) Normalized He anti-phase intensity as a function of Cu deposition time at $T = 300$ K onto surfaces which were treated by 36 Langmuir O_2 exposure. The lower curve was taken from a surface onto which 0.05 ML Cu were deposited at 100 K prior to O_2 exposure. b) Normalized He anti-phase intensity as a function of Cu deposition at $T = 300$ K after 36 Langmuir O_2 exposure. Deposition was interrupted as indicated by the arrow, and continued after a couple of minutes.

which were treated by Cu pre-deposition, and O_2 exposure (see Fig. 2.12 and Fig. 2.13a. Most interestingly, interruption of deposition during the first oscillation, and continued deposition after a few minutes does *not* result in the completion of the

original interrupted oscillation, but rather in the appearance of a new, complete, oscillation, having the "normal" period (see Fig. 2.13b). This effect does not occur when oxygen is not present on the surface, and 2D growth is induced by e.g. pulsed ion bombardment.

The general picture emerging is that nucleation of oxygen containing islands takes place upon Cu deposition. This stage is accompanied by the small increase in the He intensity, as the oxygen is no longer freely distributed on the terrace. Continued deposition produces a very rough oxygen-containing layer, within which rearrangement of the oxygen position is possible during the time scale of the experiment. This stage is accompanied by a strong decrease in He intensity. Rearrangement presumably continues during the time needed to complete one or two oscillations, and results in the unconventional features occurring during the first two oscillations. On the resulting rough surface, mobility of copper adatoms is restricted, and oscillations in the He intensity can be observed. Oscillations persist as the oxygen is able to float up to the growth front. With increasing deposition, the initial roughness of the surface may be partially smoothed out, and the reflected intensity increases slightly in some cases.

The details of oxygen interaction, and especially the dynamics during the initial stages of Cu deposition seem to be quite complex, and deserve a more thorough examination which is beyond the scope of this present work. These questions may well be better addressed using real-space techniques.

Bibliography

[1] D. K. Flynn-Sanders, J. W. Evans, P.A. Thiel, Surf. Sci. **289**, 75 (1993); H. C. Kang, D. K. Flynn-Sanders, P.A. Thiel, J.W. Evans, Surf. Sci. **256**, 205 (1991)

[2] S. T. Purcell, B. Heinrich, A. S. Arrott, Phys. Rev. B **35**, 6458 (1987); E. Kopatzki, S. Gunther, W. Nichtl-Pecher, R. J. Behm Surf. Sci. **284**, 154 (1993)

[3] J. J. de Miguel, A. Sánchez, A. Cebollada, J. M. Gallego, J. Ferrón, S. Ferrer, Surf. Sci. **189/190**, 1062 (1987); H. J. Ernst, F. Fabre, J. Lapujoulade, Surf. Sci. **275**, L682 (1992)

[4] W. F. Egelhoff, Jr., I. Jacob, Phys. Rev. Lett. **62**, 921 (1989)

[5] H.A. van der Vegt, W. J. Huisman, P. B. Howes, E.Vlieg, Surf. Sci. **330**, 101 (1995); P. Bedrossian, B. Poelsema, G. Rosenfeld, L. C. Jorritsma, N. N. Lipkin, G. Comsa, Surf. Sci. **334**, 1 (1995)

[6] Y. Suzuki, H. Kikuchi, N. Kosizuka, Jap. J. App. Phys.**27**, L1175 (1988)

[7] R. Kunkel, B. Poelsema, L. K. Verheij, G. Comsa, Phys. Rev. Lett. **65**, 733 (1990)

[8] B. Poelsema, R. Kunkel, N. Nagel, A. F. Becker, G. Rosenfeld, L. K. Verheij, G. Comsa, Appl. Phys A **53**, 369 (1991)

[9] M. Bott, T. Michely, G. Comsa, Surf. Sci. **272**, 161 (1992)

[10] B. Poelsema, A. F. Becker, R. Kunkel, G. Rosenfeld, L. K. Verheij, G. Comsa, Springer Proceedings in Physics Vol.**73** Eds. R. F. Howe, R. N. Lamb, K. Wandelt, Springer-Verlag, Berlin, 1993 pp. 95

[11] M. Henzler, T. Schmidt, E. Z. Luo, The Structure of Surfaces IV, ed. X. D. Xie, S. Y. Tong, M. A. van Hove, World Scientific, Singapore 1994, pp. 619

[12] G. Ehrlich, F. G. Hudda, J. Chem. Phys. **44**, 1039 (1966)

[13] R. L. Schwoebel, E. J. Shipsey, J. Appl.Phys. **37**, 3682 (1966)

[14] M. Villarba, H. Jonsson, Phys. Rev. B **49**, 2208 (1994)

[15] J. Jacobsen, K.W. Jacobsen, P. Stoltze, J.K. Nørskov, Phys, Rev. Lett. **74**, 2295 (1995)

[16] M. Bott, M. Hohage, T. Michely, G. Comsa, Phys. Rev. Lett. **70**, 1489 (1993)

[17] T. Michely, M. Hohage, S. Esch, G. Comsa, Surf. Sci. **349**, L89 (1996)

[18] G. Rosenfeld, R. Servaty, C. Teichert, B. Poelsema, G. Comsa, Phys. Rev. Lett. **71**, 895 (1993)

[19] K. Meinel, M. Klaua, H. Bethge, J. Cryst. Growth **89**, 477 (1988) ; K. Meinel, M. Klaua, H. Bethge, Phys. Stat. Sol. **110**, 189 (1988)

[20] H. A. van der Vegt, H. M. van Pinxteren, M. Lohmeier, E. Vlieg, J. M. C. Thornton, Phys. Rev. Lett. **68**, 3335 (1992)

[21] P. C. Dastoor, J. Ellis, A. Reichmuth, H. Bullman, B. Holst, W. Allison, Surf. Rev. Lett. 1, 509 (1994)

[22] M. Henzler, Prog. in Surf. Sci. **42**, 297 (1993)

[23] M. Henzler, Surf. Sci. **298**, 369 (1993)

[24] G. Rosenfeld, B. Poelsema, G. Comsa, J. Cryst. Growth **151**, 230 (1995)

[25] G. Rosenfeld, N. N. Lipkin, W. Wulfhekel, J. Kliewer, K. Morgenstern, B. Poelsema, G. Comsa, App. Phys. A, in press

[26] B. Poelsema, G. Comsa, Scattering of Thermal Energy Atoms, Springer Tracts in Modern Physics **115**, Springer, Berlin 1989

[27] B. Poelsema, G. Mechtersheimer, G. Comsa, Surf. Sci. **111**, 519 (1981)

[28] R. Kunkel, PhD thesis, Jül-2526, (Jülich 1991)

[29] H. Schlichting, D. Menzel, Rev. Sci. Instrum. **64**, 2013 (1993)

[30] M. Henzler, Appl. Surf. Sci. **11/12**, 450 (1982)

[31] J. Wollschläger, J. Falta and M. Henzler, Appl. Phys. A **50**, 57 (1990)

[32] B.D. Yu, M. Scheffler, Phys. Rev. Lett. **77**, 1095 (1996)

[33] M. Henzler, private communication

[34] J. A. Venables, Phil. Mag. **27**, 697 (1973)

[35] J. A. Venables, G. D. T. Spiller, M. Hanbücken, Rep. Prog. Phys. **47**, 399 (1984)

[36] H. J. Ernst, F. Fabre, J. Lapujoulade, Surf. Sci. **275**, L682 (1992)

[37] P. Bedrossian, B. Poelsema, G. Rosenfeld, L. C. Jorritsma, N. N. Lipkin, G. Comsa, Surf. Sci. **334**, 1 (1995)

[38] J. Jacobsen, K. W. Jacobsen, P. Stoltze, J. K. Nørskov, Phys. Rev. Lett. **74**, 2295 (1995)

[39] M. Villarba, H. Jonsson, Phys. Rev. B **49**, 2208 (1994); Surf. Sci. **317**, 15 (1994)

[40] Yinggang Li, A. E. DePristo, Surf. Sci. **319**, 141 (1994)

[41] Yingyang Li, A. E. DePristo, Surf. Sci. **351**, 189 (1996)

[42] G. Meyer, J. Wollschläger and M. Henzler, Surf.Sci. **231**, 64 (1990)

[43] J. Kliewer, Diplom thesis, University of Karlsruhe 1995, unpublished

[44] P. Stoltze, J. Phys: Condensed Matter **6**, 9495 (1994)

[45] T. Michely, G. Comsa, Phys. Rev. B. **44**, 8411 (1991)

[46] T. Michely and C. Teichert, Phys. Rev. B **50**, 11156 (1994)

[47] C. Teichert, M. Hohage, T. Michely, G. Comsa, Phys. Rev. Lett. **72**, 1682 (1994)

[48] M. Breeman, D. O. Boerma, Surf. Sci. **278**, L110 (1992)

[49] J. C. Girard, Y. Samson, S. Gauthier, S. Rousset, J. Klein, Surf. Sci. **302**, 73 (1994)

[50] B. Poelsema, L. K. Verheij, G. Comsa, Phys. Rev. Lett. **53**, 2500 (1984)

[51] G. Rosenfeld, PhD thesis, Jül-2914, (Jülich 1994)

[52] W. F. Egelhoff, Jr. and D. A. Steigerwald, J. Vac. Sci. Technol. A **7**, 2167 (1989)

[53] M. Copel, M. C. Reuter, E. Kaxiras, R. M. Tromp, Phys. Rev. Lett. **63**, 632 (1989)

[54] M. Horn-von Hoegen, F. K. LeGoues, M. Copel, M. C. Reuter, R. M. Tromp, Phys. Rev. Lett. **67**, 1130 (1991)

[55] N. Gradjean, J. Massies, V. H. Etgens, Phys. Rev. Lett. **69**, 796 (1992)

[56] B. Poelsema, R. Kunkel, N. Nagel, A. F. Becker, G. Rosenfeld, L. K. Verheij, G. Comsa, Appl. Phys. A **53**, 369 (1991)

[57] S. Esch, M. Hohage, T. Michely, G. Comsa, Phys. Rev. Lett. **72**, 518 (1994)

[58] H. Wolter, M. Schmidt, K. Wandelt, Surf. Sci. **298**, 173 (1993); M. Schmidt, H. Wolter, K. Wandelt, Surf. Sci. **307-309**, 507 (1994); K. Kalki, M. Schick, G, Ceballos, K. Wandelt, Thin Solid Films **228**, 36 (1993)

[59] G. Ertl, Surf. Sci. **6**, 208 (1967)

[60] L. H. Dubois, Surf. Sci. **119**, 399 (1982)

[61] H. Niehus, Surf. Sci. **130**, 41 (1983)

[62] R. W. Judd, P. Hollins, J. Pritchard, Surf. Sci. **171**, 643 (1986)

Chapter 3

Heteroepitaxial Growth of Ni on Cu(111)

3.1 Introduction

One of the important aims of epitaxy is to produce smooth films on a substrate, but it is only in few cases, that the deposited material grows in a layer-by-layer mode by nature. Even in many homoepitaxial systems, e.g. Ag/Ag(111) or Cu/Cu(111), multilayer growth (3D growth) is observed during molecular beam epitaxy (MBE) [1, 2], due to growth conditions far from thermal equilibrium. In these systems, it is easy to increase the film quality by growth at higher temperatures, when the role of growth kinetics becomes less important and the increased mobility on the surface leads to a quicker equilibration to a thermodynamic stable configuration, i.e. a smooth surface. However, in heteroepitaxy this growth recipe often is counterproductive. Here the system also equilibrates faster at higher temperatures, but due to different lattice constants and different surface energies of substrate and deposited material, the stable configuration in general consists of isolated crystallites [3], or even worse, the thermodynamically favoured state is an alloy of both materials.

In homoepitaxy, the rough growth is due to the high probability that atoms landing on top of islands nucleate to form a higher layer before they can surmount the energy barrier at the island edge [4, 5] and fill the lower one. Based on this kinetic picture, growth manipulation procedures are aimed at reducing the probability for nucleation on top of existing islands. This is done by using two different adatom mobilities: during nucleation a lower one than during subsequent growth [7]. In this way, an artificially high density of nuclei is formed during the early stage of monolayer growth while during subsequent growth the mobility remains high. Adatoms landing on top of these small islands prior to coalescence reach the edge of the island much more frequently in comparison to adatoms landing on the large islands formed during undisturbed nucleation. Hence, the probability that they surmount the step edge barrier and fill the lower layer before nucleating a second layer island is increased and layer-by-layer growth can be obtained [6, 7, 8].

These procedures, already successfully applied to the homoepitaxial systems Ag/Ag(111) [6], Cu/Cu(111) [9] (and schapter 2.4) and partially Pt/Pt(111) [10, 35], should also lead to better heteroepitaxial films at low or intermediate temperatures, where the multilayer growth of the film is mainly determined by kinetics and a transition to the undesirable and rough thermodynamically favoured state is hindered. In the manipulation experiments in this chapter, we tried to apply these recipes to the heteroepitaxial system Ni/Cu(111).

Due to the small misfit of only 2.5%, Ni growth in pseudomorph layers up to film thicknesses of 7 ML on Cu(111) and then relaxes via formation of dislocations [11, 12, 13]. No stacking faults at the interface could be observed by means of x-ray photoelectron diffraction and LEED [13, 14]. However, growth does not proceed in layer-by-layer manner and the films roughen quickly with thickness [15]. Electron energy loss spectroscopy experiments show, that during the early stages of growth, intermixing of Ni and Cu starts at the interface at temperatures as low as 375 K while at even higher temperatures, the Ni film is even covered with a cap-layer of Cu [16]. The aim of the growth manipulation experiments in this chapter is to clarify, if growth can be improved using the concept of two mobilities at temperatures well below this intermixing and hence produce flat films without massive intermixing.

This chapter is divided into two major sections. The first deals with the unmanipulated growth of Ni on Cu(111). The different growth modes are revealed using helium atom scattering (TEAS) and the morphology of the films is studied with spot profile analysis low energy electron diffraction (SPA-LEED). In the second section the concept of two mobilities is used to manipulate the growth mode and the morphology of such prepared films is compared to the conventionally grown ones.

3.2 Experimental set-up

All experiments were carried out in an ultra-high-vacuum chamber with base pressure of $\approx 2 * 10^{-11}$ mbar. A 67 meV supersonic He beam was used for He scattering measurements of a transfer-width of ≈ 420 Å [9]. The scattering apparatus was also equipped with an Auger electron spectrometer (AES) and an Omicron SPA-LEED.

The sample was prepared in-situ by repeated cycles of sputtering with 1.2 keV Ne^+ ions and annealing to 800 K until no contamination could be detected by means of AES and TEAS measurements revealed a mean terrace width on the surface of over 1000 Å [9]. The sample temperature was measured using a Ni-CrNi thermocouple inserted into a cavity in the crystal. Nickel was evaporated onto the sample using a home build electron bombardment evaporator. The high purity Ni charge was cleaned by chemical etching followed by glowing in hydrogen atmosphere at 1100 K and was thoroughly degassed in UHV before the experiments. During deposition, the pressure stayed below $1 * 10^{-10}$ mbar. No contaminations in the deposited films could be found with AES. After each growth experiment, great care was taken to clean the substrate from all the deposited material by sputtering before

annealing to prevent the aggregation of Ni in the substrate.

3.3 Conventional Growth of Ni/Cu(111)

First, we determine the scattering conditions for anti-phase and in-phase He scattering of Ni on Cu(111), from which the step height can be deduced. A small amount of nickel (0.3 ML) was deposited onto the surface at an intermediate temperature (250 K) at a rate of $R = 0.02$ ML/sec. The so prepared nickel islands are mostly only one layer high. Then, by changing the angle of incidence ϑ the scattering conditions was varied, i.e. a rocking curve was taken. Under anti-phase scattering conditions, the destructive interference of the substrate with the islands leads to a strongly reduced specularly reflected intensity. On the other hand under in-phase conditions, the reflected He-beam is insensitive to the island area leading to a maximal signal. Losses in the reflected intensity are only caused by diffuse scattering from defects like step edges or point defects. The inset of Fig. 3.1a displays the rocking curve. It clearly shows two maxima and one minimum corresponding to two in- and one anti-phase scattering conditions. From the scattering angles under in- and anti-phase conditions the height of the nickel-copper step as seen by TEAS is found to be 1.91 ± 0.03Å.

3.3.1 Growth Modes

To monitor the growth of the film, TEAS is used during deposition of material, i.e., deposition curves are taken. Fig. 3.1a and b display such deposition curves of unmanipulated growth at various temperatures. During deposition at a rate of $R = 0.02$ ML/sec, the normalized He intensity under anti-phase diffraction conditions ($S = 2.5$) was recorded as a function of deposition time. At temperatures below 250 K (see Fig. 3.1a), the intensity falls monotonically during deposition, indicative of multilayer growth. At these low temperatures, interlayer mass transport is obviously inefficient. For growth temperatures between 250 K and 350 K, a single oscillation is observed followed again by a monotonous decay. The first layer grows in an imperfect two-dimensional manner. However, subsequent layers grow in a multilayer mode as indicated by the slow decay. With rising temperature, the oscillation becomes more pronounced and the following decay slower indicating that growth is smoother. Growth at these intermediate temperatures results in significantly smoother films compared to growth at low temperatures. Nevertheless, the films are still becoming rough as can be seen by the low reflected intensity after more than one monolayer deposition. For temperatures above 375 K (see Fig. 3.1b), several decaying oscillations are observed. The amplitude of the oscillations, however, is small and the overall intensity remains rather high during growth. This behaviour may be explained by parts of the surface, i.e. the smaller terraces, growing in the step-flow mode. On the larger terraces, nucleation, growth and coalescence of islands

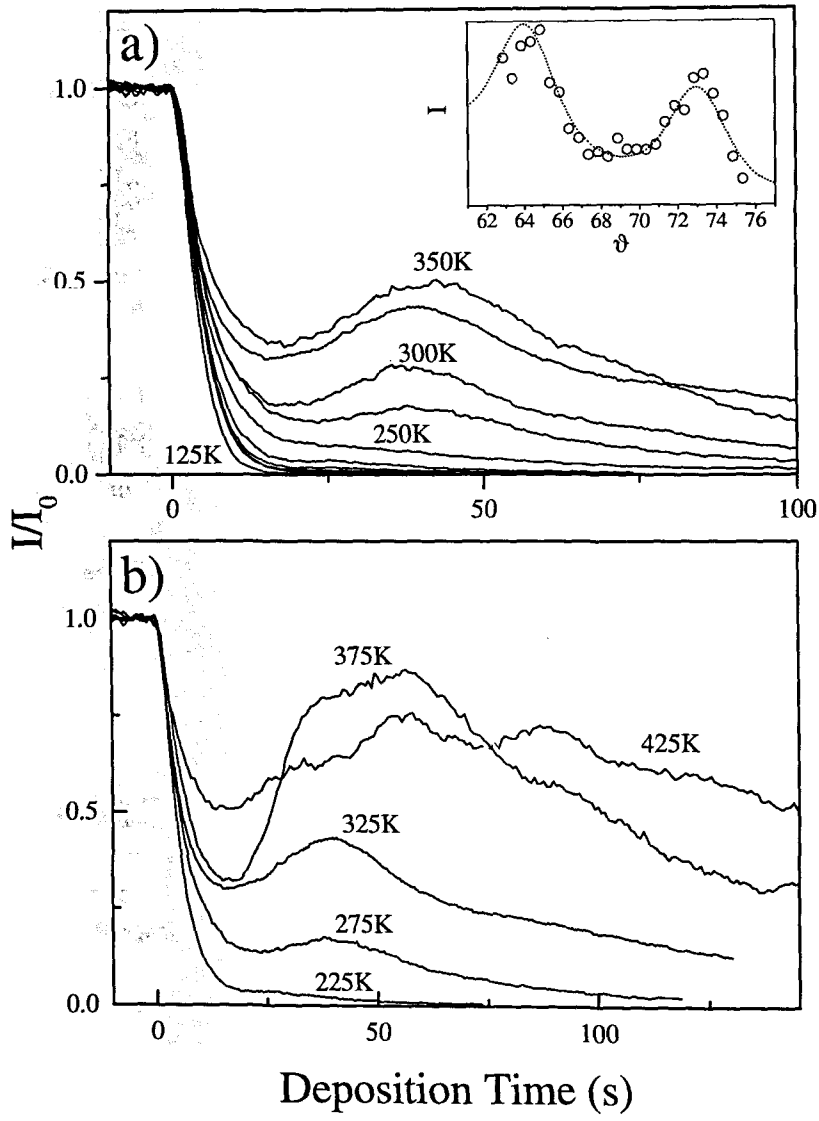

Figure 3.1: Evolution of the normalized specular He intensity under anti-phase conditions ($S = 2.5$) during deposition of Ni onto Cu(111) at a rate of $R = 0.02$ ML/sec. a): substrate temperatures varied between 125 and 350 K in 25 K steps b): substrate temperature varied between 225 and 425 K in 50 K steps. The inset displays the He intensity as a function of the angle of incidence reflected from a surface onto which 0.3 ML of Ni has been deposited at 250 K. Maxima correspond to in-phase and minima to anti-phase scattering conditions.

is taking place, resulting in the oscillations, but detailed features like the amplitude of the first oscillation and the slight variation of the frequency of the oscillations are not explained by this. Especially the fact that at 375 K a higher reflectivity than at 425 K at 1 ML coverage is observed, i.e. the film grown at a lower temperature is flatter, contradicts usual growth mechanisms. From other experiments, massive intermixing is known to start at these high temperatures [16] leading to complex intermixing kinetics which most likely influences growth substantially. The several, weak oscillations at high temperatures might also be due to the Cu-cap layer floating on the growing Ni film at this high temperatures. The Cu layer might act as a natural surfactant leading to an imperfect layer-by-layer growth. For a detailed study of the processes going on at this high temperatures a real space method is more appropriate. We therefore focus on the simpler growth situation below 375 K.

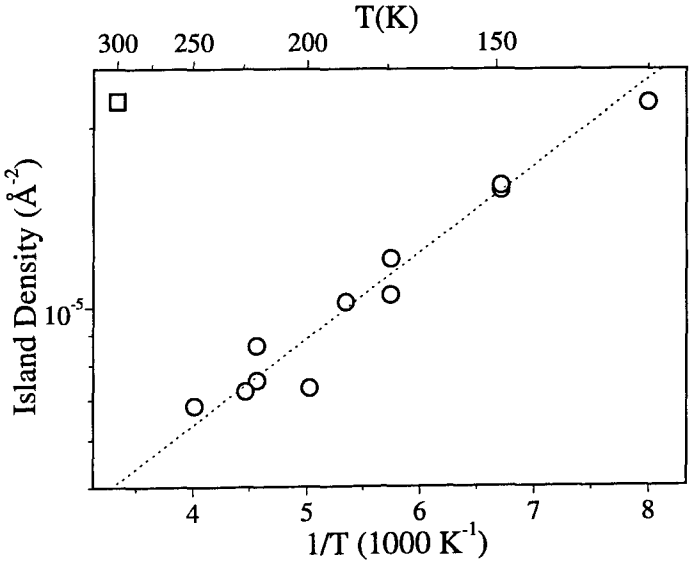

Figure 3.2: Arrhenius plot of the mean island density at 0.3 ML coverage as a function of temperature for Ni islands grown on Cu(111) by conventional growth (circles) and by ion assisted deposition (square). Deposition was carried out at a rate of $R = 0.02$ ML/sec.

To gain insight into the initial processes of film growth, the island density as a function of temperature was measured. In the experiments, 0.3 ML Ni were deposited with a rate of 0.02ML/sec at a temperature between 135 and 260 K followed by cooling to $\approx$ 120 K to suppress further diffusion. Anti-phase peak profiles, taken at that temperature, displayed a broadening due to the islands on the surface. According to the method described in [19, 20] the resulting average

island-densities were estimated from a fit to the broadened peak profiles. Fig. 3.2 displays an Arrhenius plot of the island number density. With rising temperature a decrease in the island number density is observed, as expected from the classical nucleation theory [21, 22]. The island density n is given by $n \propto \exp\left(\frac{iE_d+E_i}{(i+2)kT}\right)$, where i is the size of the critical nucleus, E_d the adatom diffusion energy on the terrace, E_i the binding energy of the critical nucleus, k the Boltzmann factor and T the temperature. Obviously, the data can be well fitted with a straight line. There are no signs for a change in the size of the critical nucleus in the temperature range studied. Supposing the dimer to be stable ($i = 1$), the linear fit to the curve gives an adatom diffusion energy for Ni on Cu(111) of $E_d = 79 \pm 18$ meV. This is in reasonably good agreement with EMT calculations for this system of $E_d = 52$ meV [23] and also explains the roughly five times higher island densities observed in this system compared to results of similar experiments for the homoepitaxial systems of Cu(111) ($E_d = 30^{+10}_{-5}$meV [9], see Fig. 2.4 on page 32) and Ag(111) ($E_d = 51 \pm 24$meV [8]). There are reasonable arguments that the opposite assumption, that the Ni dimer is not stable in the temperature range studied, is unlikely to be true. First, EMT calculations [24] estimate the binding energies of Ni dimers and Pt dimers on their (111) surface to be of similar size and the Pt dimer is found to be stable up to $\approx$245 K [25]. The small misfit between Ni and Cu should not change the situation dramatically, since a Ni dimer on the Cu surface most likely relaxes towards its bulk lattice spacing. Secondly, when $i = 2$ and a reasonable binding energy for the dimer are chosen (e.g. from EMT calculations [24]), the obtained diffusion barrier is only a fraction of the EMT value as well as the experimental values for similar homoepitaxial systems, which would imply faster diffusion and hence a much lower absolute island number density rather than the observed higher one.

3.3.2 Morphology

SPA-LEED offers with its resolution and short data acquisition times an elegant way to study the morphology of films in reciprocal space. Similar to TEAS, the scattering conditions (here the electron energy) for in and anti-phase have to be found. It is not straight forward to extract the scattering phase from the intensity as a function of the electron energy. However, the width of the specular spot contains information about the scattering phase in a simple way. At in-phase scattering conditions, the spot is sharp while at anti-phase scattering conditions, the specular peak is of maximal width. This also offers a simple method to determine the step height of the film. Provided that the energy-dependent phase shift between the deposit and the substrate is slowly varying compared to the phase shift caused by the interlayer distance, the step height can be determined [26].

Fig. 3.3 shows LEED peak profiles of the specular spot of surfaces onto which 1 ML of Ni were deposited at 140 K followed by a quench to 100 K. As already deduced from the TEAS measurements of the island density, the structures are small at these low temperatures and as a consequence the effect on the variation of

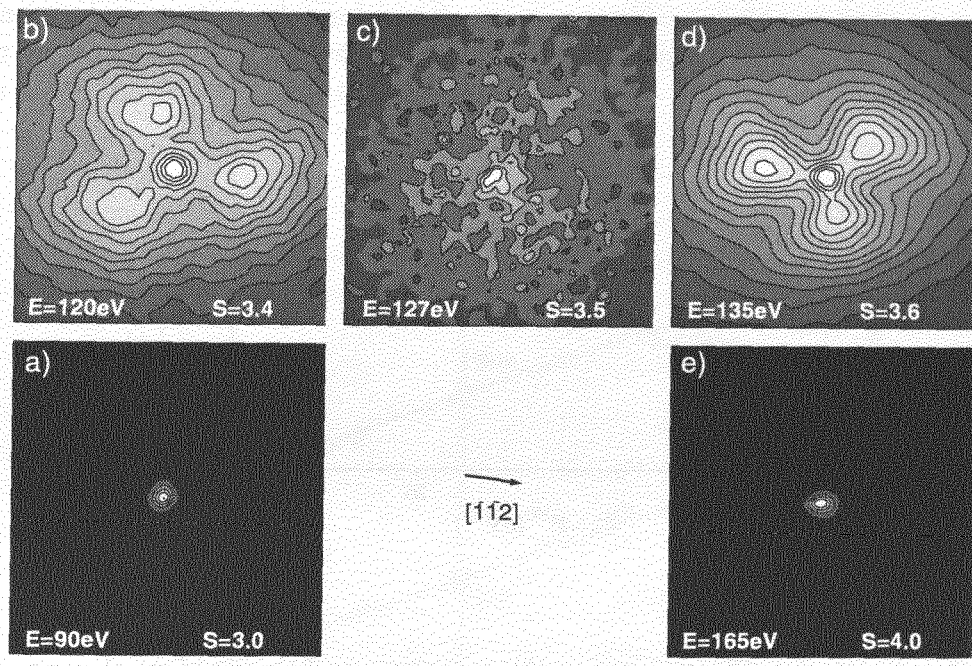

Figure 3.3: LEED contour plots of the (00)-spot in linear intensity scale of 1 ML Ni deposited at 140 K with incident electron energies as indicated. The size of the scans are 30% by 30% of the surface Brillouin zone.

the peak width with energy should be large. All scans are 30% by 30% of the surface Brillouin zone (SBZ) in size. At certain electron energies, the observed peak is very sharp like in Fig. 3.3a and e corresponding to in-phase scattering conditions. When raising the energy, the peak widens until three distinct facet reflexes become visible (see Fig. 3.3b) which move away from the specular peak and finally disappear and leave behind a very broad spot of low intensity (FWHM $\approx$ 10 %SBZ) corresponding to anti-phase scattering condition (see Fig. 3.3c). When the energy is further increased, again three facet reflexes show up but with a flipped orientation (Fig. 3.3d), move towards the central spot and at last merge with it again at in-phase condition (Fig. 3.3e).

In Fig. 3.4 the scattering phase S of in-phase (squares) and anti-phase (circles) conditions as determined by the sharpness of the spots is plotted versus the square root of the electron energy. A least square fit to the points yields the height of the Ni step on the Cu substrate to be 1.92 ± 0.03 Å which coincides with the step height seen with TEAS.

From the fact that both diffraction techniques see the same step height, although LEED probes the core level electrons while TEAS only probes the outermost electrons due to a turning point $\approx$ 3 Å in front of the surface, it can be concluded, that

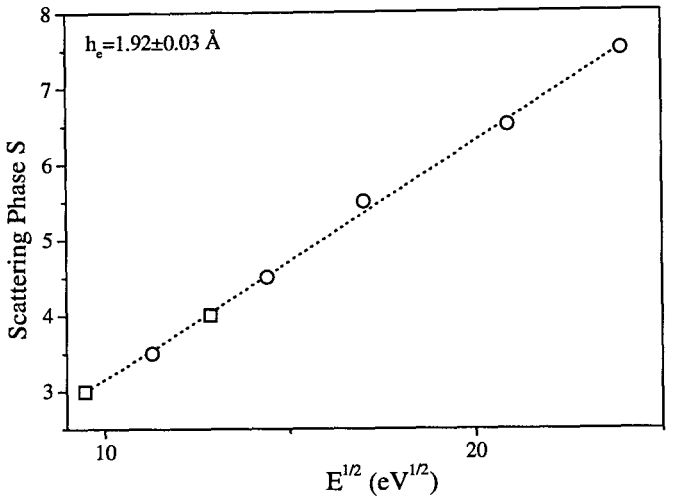

Figure 3.4: Scattering Phase S versus the square root of the incident electron energy determined from the broadening of peak profiles of 1 ML Ni deposited at 140 K. In-phase scattering conditions (squares) have been determined from sharp specular peaks and anti-phase (circles) from the flipping of the facet reflexes.

the interaction of He with the substrate and the film does not differ significantly as theoretical calculations predict [27] and that the differences in the energy dependent phase shift between electrons scattered from a Ni and a Cu atom is negligible in the energy range studied.

However, the experimental findings are not in good agreement with simple elasticity theory which predicts a 1.4% contraction of the interlayer distance when the Ni lattice is stretched in the (111) plane to the Cu lattice spacing under elastic deformation [28]. This results in a step height of 2.00Å. The measured interlayer distance is significantly smaller, showing the limited applicability of elastic bulk properties to ultra thin Ni films.

Having determined the step height and the scattering phase S as a function of the electron energy, we return to the study of the morphology of the films deposited at low temperatures. From the fact, that the observed diffraction pattern displays a threefold symmetry with three facet peaks under diffraction conditions close to anti-phase diffraction (Fig. 3.3d, b), one can directly deduce that the islands grown at this low temperatures show a threefold symmetry, i.e., are of triangular shape or are built up of smaller triangular parts, and that a certain facet slope is selected during growth of the islands. However, the facet peaks are very broad (FWHM $\approx$ 10% SBZ) indicating, that the facets are very small, irregular or that a distribution of facets with slightly varying orientation is present. This finding agrees with the

strong damping of the He intensity observed during growth, which is characteristic for a rough growth mode and small structures. The positions of the centre of the facet spots in k-space were surveyed as a function of electron wave number, i.e., a map of the facet rods in reciprocal space was made and is shown in Fig. 3.5. The

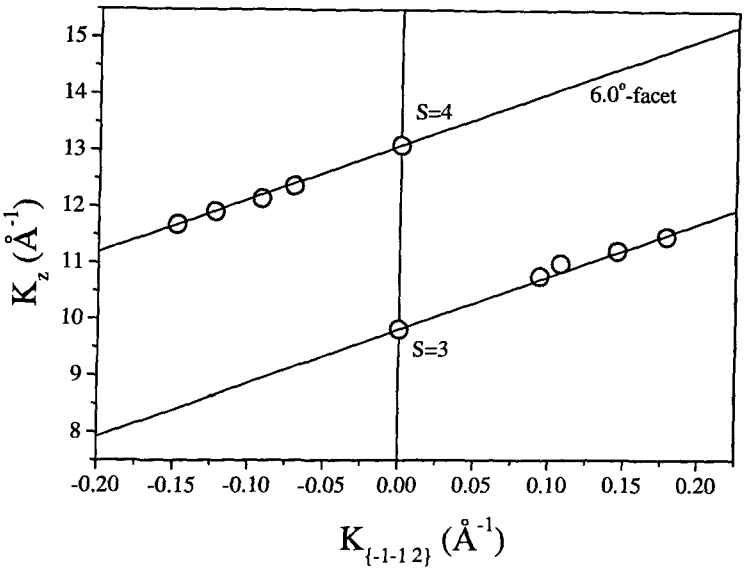

Figure 3.5: Reciprocal space mapping of the facet reflexes of 1 ML Ni deposited at 140 K (circles) and of a {445} facet (solid line).

measured positions (circles) are best fit with facets of a tilt angle of 6.0°, which is close to a {445}-facet. Since the facet spots are rather wide, it is questionable to talk about well ordered facets on the surface. Nevertheless, there is a preferential slope of the multilayer islands of 6° and from the direction of the movement of the facet peaks with energy, one can conclude that mainly {100} step edges are present on the surface. The other possible closed packed step edge, i.e., the {111} step edge, is not observed in the diffraction pattern.

First, we focus on the specific slope of the three-dimensional islands. The same slope of the facets have also been observed for films of 3 and 6 ML thickness within the uncertainty due to the rather diffuse peaks. In addition, for thicker films, the facet peaks become increasingly smeared out. It is unlikely that at such low coverages as 1 ML already mechanisms like slope selection or kinetic roughening are responsible for the specific slope observed. It is more likely that the lack of interlayer mass transport in combination with a typical island separation is the reason for the typical slope, which also explains the gradual loss of the preferred slope when coverage is increased. A simple estimation, using geometric arguments, illustrates this.

Assuming an regular array of perfect triangularly shaped islands with a separation taken the estimate of the island density from the fit of Fig. 3.2, one obtains a facet angle of $\approx 4°$, when interlayer mass transport is neglected. Keeping in mind the simple assumptions, this is in good agreement with the experiments. Allowing the island edges to be slightly rugged, which is reasonable at this low growth temperatures, the calculated facet angle is increased. In addition, the simple model is based on a regular arrangement of islands, which is only a crude approximation and the island densities obtained from the anti-phase peak profiles are only an estimation.

Second, we focus on the specific orientation of the step edges of the islands. The same orientation of the islands, i.e., the predominant existence of {100} step edges, has been found in the homoepitaxial growth of Pt(111) at a temperature range above dendritic growth and below $\approx$ 450 K with STM [29] and of Cu(111) at low temperatures and low growth rates with SPA-LEED [30]. The finding of the same orientation of islands also in the heteroepitaxial case of Ni on Cu(111) suggests that a mechanism fundamental for fcc (111) surfaces is responsible for this. The predominance of {100} step edges does not reflect the equilibrium shape of the islands as shown in the case of Pt/Pt(111) by STM [29] and later in this paper for Ni/Cu(111) with SPA-LEED. The shape of the island is caused by temperature dependent growth speeds of the two types of step edges. At low temperatures, the growth speed of the {111} step edges is faster than that of the {100} step edges, so that in compact structures, the {111} step edges die out quickly and a triangular island or an island consisting of triangular parts with {100} step edges is formed.

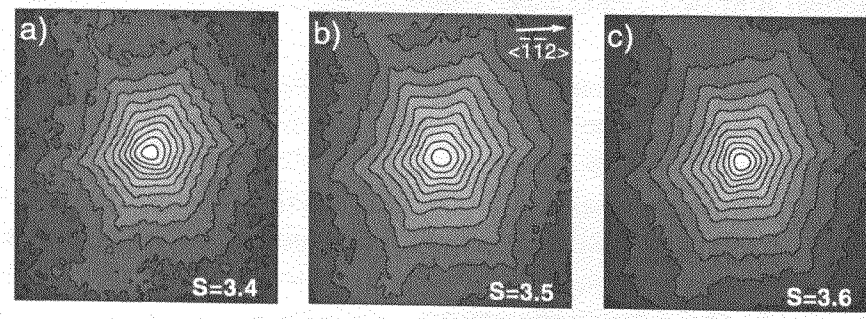

Figure 3.6: LEED contour plot of the (00)-spot in logarithmic intensity scale of 2 ML Ni deposited at 300 K with scattering phase S as indicated. The size of the scans are 30% by 30% of the surface Brillouin zone.

When the growth temperature is raised, the situation changes. The specular LEED spot of 2 ML Ni deposited at 300 K displays a star-like diffraction pattern

of sixfold symmetry in a wide energy range around anti-phase scattering conditions as can be seen in Fig. 3.6. At in-phase, a sharp spot-like diffraction pattern is observed, similar to those of Fig. 3.3a and e. Especially below (Fig. 3.6a) and above (Fig. 3.6c) the anti-phase condition, scattering in neither specific direction corresponding to {100} and {111} type of step edges is dominating. Hence, both types of steps are equally present on the surface. No specific facet reflexes are found indicating that the growth of 2 ML Ni at that temperature does not lead to distinct facets. The FWHM at anti-phase scattering condition of 2.5% SBZ indicates, that the film is far from being perfectly flat. The diffraction peak, consisting of a strong central spike and weak, broad wings of sixfold symmetry, may be explained by flat islands of either a superposition of both of the two possible orientations of triangular islands or more likely of a hexagonal shaped islands analogous to the islands observed on Pt(111) during homoepitaxy around 450 K [29], Cu(111) above 200 K [30] and Ag(111) at room temperature [31]. The phenomenon of a transition in growth shapes from {100} step edges at low temperatures to both types of step edges at intermediate temperatures was also found in Pt(111) [29] and Cu(111) [30]. But in the case of platinum this transition is driven by the growth speeds of the two types of steps which are equal at intermediate temperatures, where hexagonal islands are observed. When raising the temperature even higher, the growth speeds may even reverse and triangular islands with {111} step edges have been observed [29]. In the case of Ni/Cu(111) the change of the island shape is more likely driven by thermodynamical effects, since annealing experiments show that already above 250 K the threefold symmetry of the specular spot transforms into a sixfold symmetry, as will be discussed later.

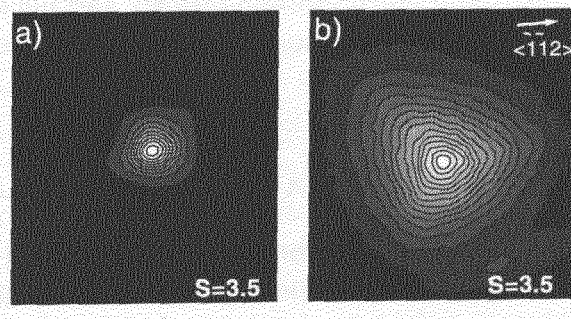

Figure 3.7: Anti-phase ($S = 3.5$) LEED profiles of the (00)-spot in linear intensity scale of a) 2 ML b) ≈ 8 ML Ni deposited at 440 K. The size of the scans are a) 10% by 10% b) 40% by 40% of the surface Brillouin zone.

When choosing an elevated growth temperature above 375 K, considerable intermixing sets in, but as already deduced from the deposition curves of Fig. 3.1b, the reflectivity remains high during growth, i.e., the film grows two-dimensionally. In accord to this, the anti-phase spot of 2 ML Ni deposited at 440 K is with a FWHM of 1.3% SBZ rather sharp and featureless, indicating a flat film (see Fig. 3.7a). This situation changes when the thickness is larger than 7 ML and dislocations build up to relax the film tension [12, 13]. Fig. 3.7b shows the (00)-spot of $\approx$ 8 ML Ni deposited at 440 K. The peak has a threefold symmetry and is with 13% SBZ extremely wide. Surprisingly, the width and shape does not depend on the scattering phase S as expected from a rough layer. When varying S in a range of $S = 3 - 4$, no major changes in the shape of the spot profile are detectable. This means, that whatever is responsible for the widening of the peak, it is certainly not related to the elementary step height of the system or a height in the same order of magnitude. This widening is more likely caused by a mosaic structure or distortions due to the dislocations in the film.

3.4 Growth Manipulation in Ni/Cu(111)

Similar to the growth manipulation experiments for Cu/Cu(111) of chapter 2.4, we also use the concept of two mobilities to enhance interlayer mass transport during heteroepitaxial growth of Ni on the same surface and by this achieve layer-by-layer growth. Provided that the film morphology is mainly determined by kinetics, also in this heteroepitaxial system the kinetic growth recipes should lead to flatter films. In the following, the mobility of the Ni adatoms during nucleation is reduced by three different methods and an artificially high density of nuclei is created. Then, growth is continued with a second and higher mobility. So, instead of few larger islands, many small islands grow on the surface. Ni adatoms landing on top of these small islands reach the edge of the island much more frequently and hence, the probability that they surmount the step edge barrier and fill the lower layer before nucleating a second layer island is increased.

3.4.1 Growth Manipulation via Temperature Alternation

As described in the previous section, also for Ni on Cu(111) the island density increases exponentially when deposition temperature is lowered and by this offers a simple way to artificially increase the island number density. Analogous to such experiments in the homoepitaxial system Ag/Ag(111) [6] and Cu/Cu(111) (see chapter 2.4.1), a significant improvement in interlayer mass transport resulting in layer-by-layer growth should be obtained, when performing the nucleation of islands at lower temperatures followed by deposition at higher temperatures for the rest of monolayer growth.

To test this procedure, first just enough material was brought onto the surface to

accomplish the stage of nucleation, i.e. 0.1 ML, at low temperatures ranging from 70 to 220 K. Then, the deposition was continued at higher temperatures between 200 and 300 K. Presuming that the nuclei survive the heating to the second temperature, the artificially raised island number density on the surface should result in an improved interlayer mass transport. However, none of the various deposition curves showed as strong oscillations as in the case of Ag/Ag(111) or Cu/Cu(111). No clear

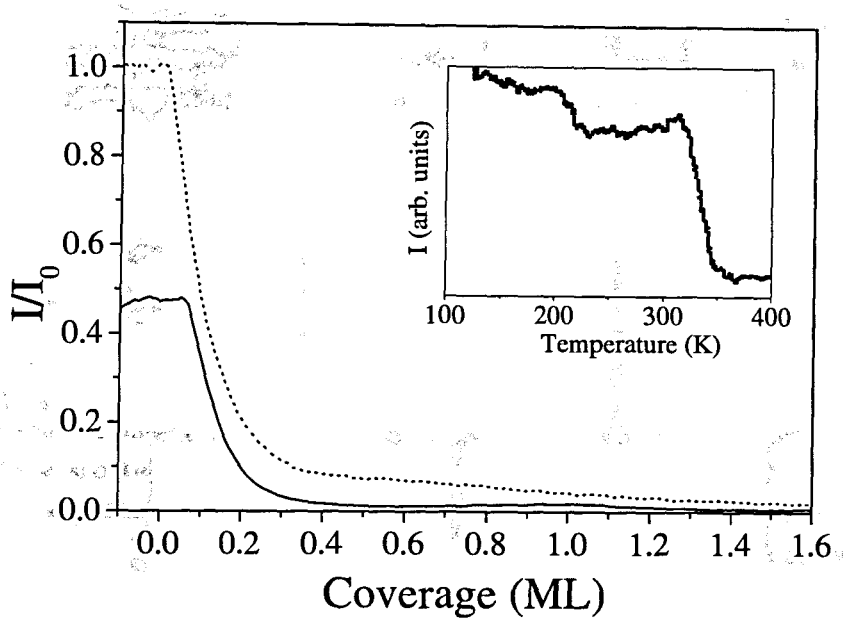

Figure 3.8: Evolution of the normalized anti-phase He intensities during deposition of Ni at $T = 245$ K onto Cu(111) surfaces, which were treated by pre-deposition of 0.1 ML Ni at 135 K (solid line) and for comparison during unmanipulated growth at $T = 245$ K (dotted line). Deposition was carried out at a rate of $R = 0.02$ ML/sec. The inset displays the in-phase $S = 2$ intensity during annealing of 0.3 ML Ni, deposited onto Cu(111) at 125 K, as a function of substrate temperature.

improvement of the growth could be obtained. On the contrary, as can be seen in Fig. 3.8, the normalized anti-phase He intensity reflected from the surface after the second stage of growth may even be lower than during natural growth, indicating that the film might even be rougher. Since lowering the temperature *does* increase the island number density also in the case of Ni on Cu(111), this discrepancy cannot be due to the nucleation but must be due to an unusual annealing behaviour of the Ni islands created at low temperatures during heating to the second and higher growth temperature. To study this annealing behaviour, the specularly reflected in-phase intensity ($S = 2$) of 0.3 ML Ni on Cu(111), deposited at 125 K, was recorded during heating. The in-phase intensity is insensitive to the layer distribution and is only determined by the density of steps and point defects. Surprisingly, as can

be seen in the inset of Fig. 3.8, the intensity[1] drops in two steps slightly above 200 K and at $\approx$ 320 K indicating that the surface roughens and either steps or point defects are created. This behaviour is the exact opposite of the one observed in the homoepitaxial systems Ag(111) and Cu(111) [6, 9] (see Fig. 2.2 on page 28). But even in the case that the second temperature is chosen below the first annealing step, i.e., below 200 K, and the nucleation temperature as low as possible (70 K), only multilayer growth could be observed, which is most likely due to the rather low enhancement of island number density after this temperature variation and the low probability of adatoms to thermally surmount the step edge barrier at this low growth temperatures.

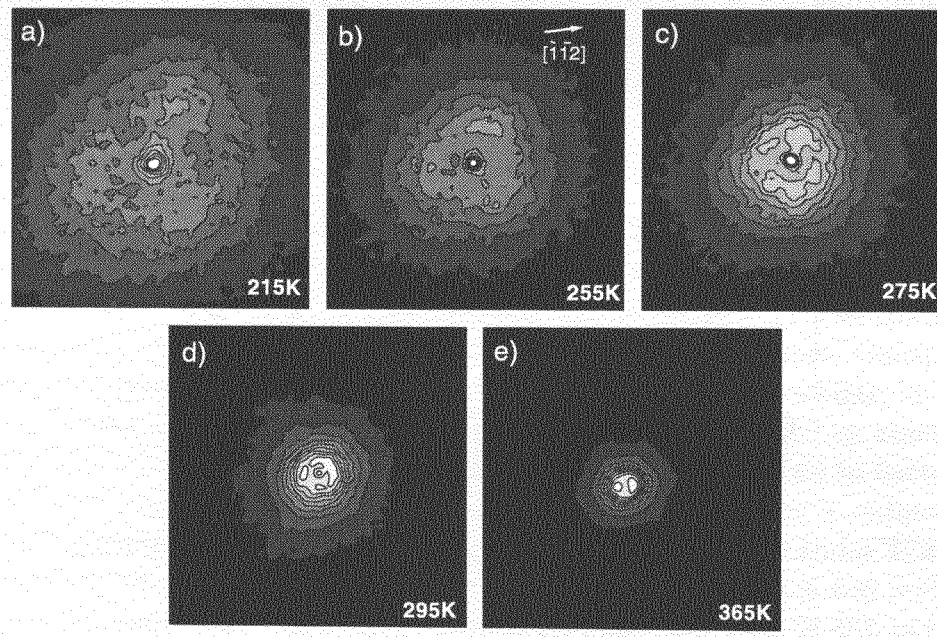

Figure 3.9: Near anti-phase (S = 3.6) LEED profiles of the (00)-spot in linear intensity scale taken during annealing at temperatures as indicated of 1 ML Ni deposited at 115 K. The size of the scans are 50% by 50% of the surface Brillouin zone.

We also took SPA-LEED profiles in anti-phase scattering conditions during annealing. The information gained from these profiles is complementary to those from the in-phase TEAS annealing curve. The in-phase specular TEAS intensity is predominantly sensitive to step edges or point defects like adatoms or vacancies, while SPA-LEED profiles under anti-phase scattering conditions reflect the layer distribution. In contrast to the roughening of the film seen by TEAS, the SPA-LEED profiles of 1 ML Ni deposited at 115 K show the normal sharpening trend of the spots during annealing, as can be seen in Fig. 3.9. When heating up the sample,

[1] The intensity has been in first order corrected for Debye-Waller effect of the substrate, only.

initially the spot narrows a bit, but still shows facet spots of threefold symmetry (see Fig. 3.9b). This may be explained by a slight smoothing of the rather ragged islands reducing the scattering from the specular spot. When the temperature is further increased, the facet spots suddenly disappear at $\approx$ 265 K and leave a circular ring behind, as displayed in Fig. 3.9c. Also the threefold symmetry disappears. Here, obviously, the predominance of the {100} step edges is lost and the islands begin to anneal to an equilibrium shape. The ring reflects the isotropic distribution of islands with a typical island separation set during nucleation. Further heating results in a rapid collapse of the ring diameter and the appearance of a background around the spot of clearly sixfold symmetry (see Fig. 3.9d and e). The islands now have sixfold symmetry and two-dimensional Ostwald ripening begins. Hence, the SPA-LEED profiles during annealing show a similar annealing behaviour as that of Cu islands on Cu(111). First, diffusion along the island edge sets in resulting in a change of the island shape and in a second step the evaporation of atoms from the step edge onto the terrace is activated, leading to two-dimensional Ostwald ripening. The apparent discrepancy between the results of LEED and TEAS can easily be lifted. It seems that during the annealing of the islands, point defects are created. Especially at higher temperatures, the rearrangement of atoms on the surface can lead to intermixing and upward diffusion of Cu, driven by the lower surface free energy of Cu. These defects do not show up in the LEED data, but may cause strong diffuse scattering in the TEAS measurements and may also act as nucleation centers in the second layer, such that growth, continued on annealed films results in multilayer growth instead of layer-by-layer growth. Therefore, in the case of Ni on Cu(111), the lower surface free energy of Cu leads to complications that prevent the successful application of temperature variation to obtain layer-by-layer growth. During heating to the second growth temperature, which typically takes several minutes, the surface is left to evolve towards thermal equilibrium by intermixing and the purely kinetic method of two mobility must fail.

Since the threefold symmetry is lost and a sixfold symmetry is achieved during annealing already at temperatures around 275 K, edge diffusion at these temperatures is sufficiently quick to allow the triangular islands to transform into hexagonal ones and the equilibrium shape of the islands is approached. Hence, also the sixfold symmetry of the (00) spot after growth at 300 K is most likely due to this equilibration of the island shape by diffusion along the step edges and not necessarily due to the growth speed of both types of steps being equal at that temperature. Obviously, the heteroepitaxial system of Ni/Cu(111) behaves differently from the homoepitaxial case of Pt(111), where at intermediate temperatures also hexagonal islands are observed, but due to a different reason. In the case of Pt, a crossover of the growth speeds of the two step types occurs. Efficient diffusion for the equilibration of the island shape only sets in at substantially higher temperatures [29].

3.4.2 Growth Manipulation via Rate Variation

A second way to increase the island number density during nucleation is to perform nucleation at a higher deposition rate than the subsequent growth, but the island number density only slowly varies with the deposition rate $n \propto R^{i/(i+2)}$ as has been derived by Venables [21, 22]. Hence, a rather large difference in deposition rates is required to achieve reasonably high enhancement factors for the island density. With our conventional electron bombardment evaporator, rate variations over two decades were possible, but did not lead to significantly better films. To achieve a very high flux during nucleation, a special evaporator was built consisting of thin high purity Ni wires which were thoroughly degassed in UHV. By discharging a large capacitor

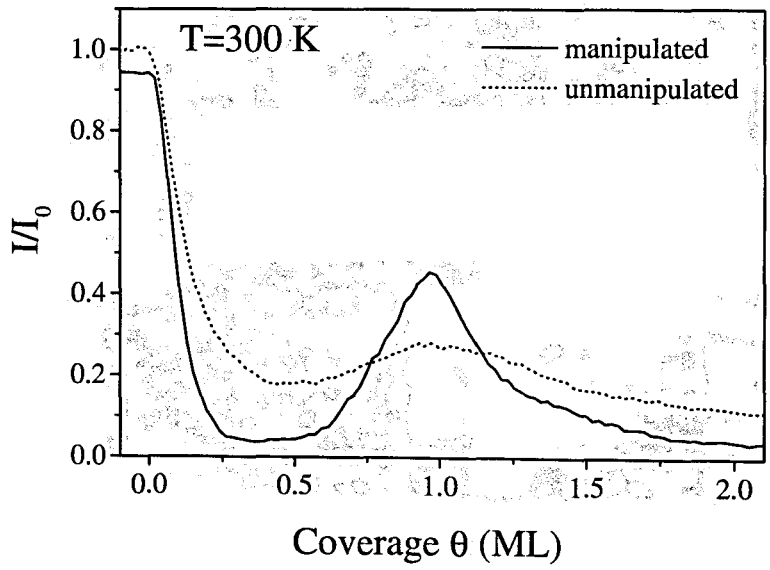

Figure 3.10: Normalized anti-phase He intensity during deposition of Ni at 300 K onto a surface, which was treated by pre-deposition at a high rate (solid line) and for comparison without pre-deposition (dotted line).

over one of the wires, it is instantaneously evaporated in an explosion resulting in a high deposition rate. The mass of the wires were chosen so that only less than 0.05ML is deposited onto the sample by the explosion. After nucleation of islands in this way, the electron bombardment evaporator is used to continue growth. As can be seen in Fig. 3.10, which depicts the reflected anti-phase He intensity during such a growth experiment at 300 K, a stronger oscillation and a higher reflectivity at monolayer completion is achieved when rate modulation is used (solid line) in comparison to the unmanipulated growth (dotted line), i.e. growth manipulation by a large rate variation does promote layer-by-layer growth and results in smoother

films. In contrast to temperature variation, here intermixing is limited since growth is continued only a few seconds after nucleation preventing strong upwards diffusion of Cu.

This very cheap and simple method of exploding wires has the obvious disadvantage that for each manipulation a new wire is needed. A more elegant way to modulate the deposition rate over many orders of magnitude offers the use of pulsed laser deposition for nucleation accompanied by conventional MBE for the growth of the rest of the monolayer. Here, the differences in rates may even be higher and hence, even better layer-by-layer growth may be achieved.

3.4.3 Growth Manipulation via Ion Beam Pulses

As a third way of creating an artificially high density of nuclei, bombardment of the surface with ions prior to deposition or during the early stage of the growth of each monolayer was used. Besides vacancies or vacancy islands in the topmost layer, adatoms are created by this on the topmost layer due to displacement of atoms by collisions or upward diffusion of interstitials created by collision cascades in the bulk [8, 32, 33, 34, 35]. These often form one or several adatom islands close to the impact site which then may serve as artificial nucleation centres during growth of the Ni film.

In a series of growth experiments at a substrate temperature of 300 K, freshly prepared surfaces were bombarded with a fluence between 0.8 and 8.2 $*10^{17}$ ions/m^2 of 1.2 keV Ne^+-ions corresponding to a sputtering of 0.015 to 0.16 ML [9]. Immediately after ion bombardment, Ni deposition was started at a rate of 0.02 ML/sec. The normalized anti-phase He-intensities recorded during manipulated and unmanipulated growth for comparison are shown in Fig. 3.11a. It can clearly be seen that ion bombardment at all used fluences leads to a stronger oscillation and a higher reflectivity around 1 ML coverage compared to the unmanipulated case. This indicates a smoother growth of the film and a higher degree of filling of the first monolayer. Nevertheless, strong differences show up when varying the fluence. For the lowest fluence, the oscillation is enhanced only weakly. When the fluence is raised, the oscillation becomes stronger. For the highest fluence, though, the maximum intensity near layer completion is not the highest but somewhat lower, which is most likely due to the surface structure after sputtering with such a high fluence. Since at the chosen substrate temperature sputtering does not lead to layer-by-layer but multilayer removal, a high ion fluence results in a surface structure with several open layers. Especially the created vacancies or vacancy islands can no longer be neglected. These vacancies are only filled by direct deposition of atoms and not by downward diffusion of adatoms from the first layer, since the material deposited on the first layer is immediately captured due to the high density of nuclei. This results in a lower reflectivity during growth. The best results are obtained for the intermediate ion fluence of $4*10^{17}$ ions/m^2 corresponding to a sputtering of 0.08 ML.

Also for doses between 0.8 and 8.2 $*10^{17}$ ions/m^2 anti-phase peak profiles were

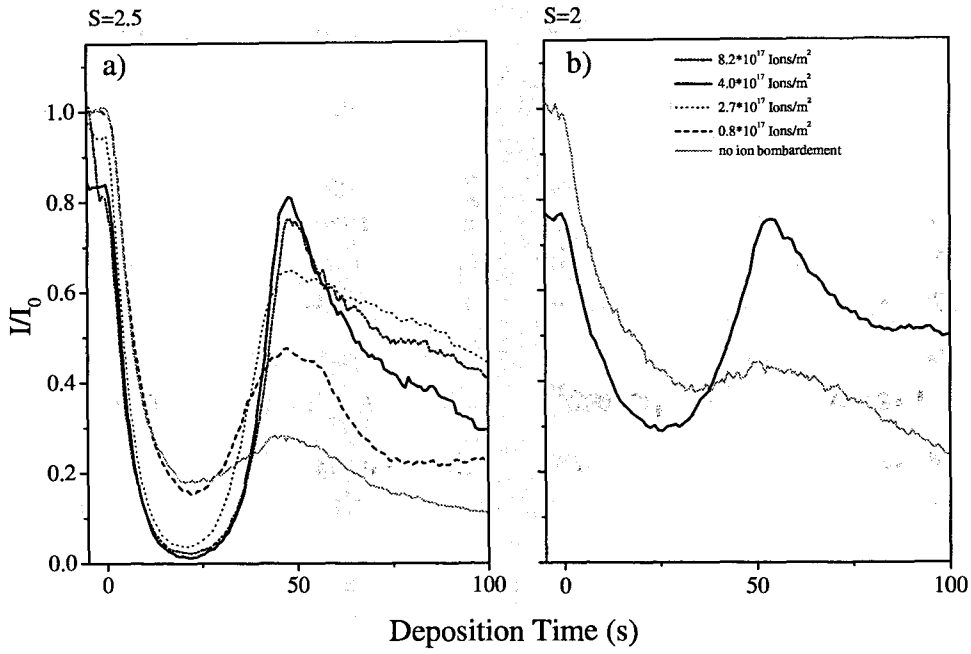

Figure 3.11: Normalized anti-phase (a) and in-phase (b) He intensities during deposition of Ni at 300 K onto surfaces which were treated by ion bombardment with fluences as indicated. Deposition was carried out at a rate of $R = 0.02$ ML/sec.

taken after deposition of 0.5 ML of Ni at 300 K to estimate the island density. Within the error of measurement, they display the same island density as depicted by the square in Fig. 3.2. This island density was also observed for equivalent experiments in the homoepitaxial system of Cu/Cu(111) with doses above $8*10^{16}$ ions/m^2 [9], where the island density created by sputtering saturates (see Fig. 2.8 on page 37). It is not clear, why in the case of Ni/Cu(111) a dose of $4*10^{17}$ ions/m^2 leads to better results than a lower dose of $8*10^{16}$ ions/m^2, although the island density observed at half monolayer coverage is the same. It seems, that in the heteroepitaxial case the enhancement in the island density is not the only parameter that determines the film quality.

To gain information about the density of defects during manipulated growth, also in-phase growth curves were taken as shown in Fig. 3.11b. Growth on surfaces pre-sputtered with a fluence of $4*10^{17}$ ions/m^2 show in the first stage of growth a lower reflectivity. This is expected and is due to the higher step density on such surface due to the enhanced island density. However, at one monolayer coverage and beyond, the intensity reflected from manipulated films is significantly higher than that of the unmanipulated. Obviously at higher coverages, the defects created by sputtering are insignificant in comparison to the step density evolving during the imperfect natural growth. Not only the layer distribution is better for the

manipulated films but also the defect density is lower.

Similar experiments at different substrate temperatures also revealed strong oscillations and good layer-by-layer growth after soft sputtering, even at low temperatures where no oscillations were observed during unmanipulated growth (see Fig. 3.12).

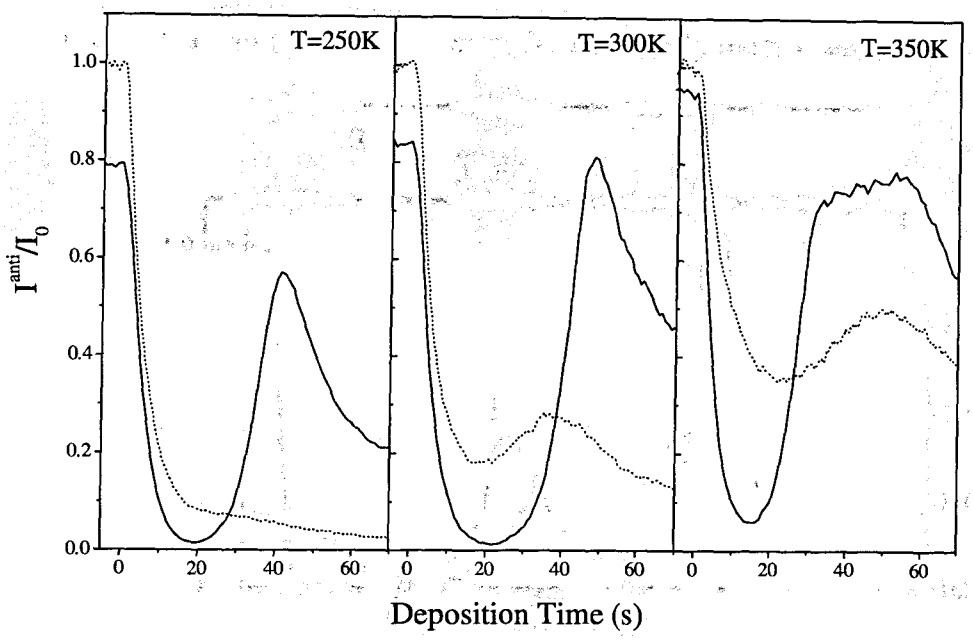

Figure 3.12: Normalized anti-phase He intensities during manipulated (solid) and unmanipulated (dotted) growth of Ni at temperatures as indicated. For manipulated growth, surfaces were treated by ion bombardment with a fluences of $Q = 8 * 10^{16}$ ions/m^2 prior to deposition at a rate of $R = 0.02$ ML/sec.

However, the better *surface* of the films might be traded for a slightly roughened film-substrate *interface*. The nuclei created by sputtering consist of Cu and not of Ni atoms and also some vacancies in the substrate Cu layer are created. Thus, growth on pre-sputtered surfaces might cause a rougher interface between the substrate and the film, but this roughness is rather small since the dose used corresponds to sputtering of only 0.08 ML (see chapter 2.4.2). To grow equally smooth films in unmanipulated growth, temperatures well above 375 K are needed [11], at which strong intermixing and even an up-sweep of a complete Cu cap-layer may occur [16]. Presumably, these diffusion processes will lead to an even rougher interface between film and substrate.

Besides the fact, that pre-sputtering leads to smoother film surfaces, one can learn from the enhanced amplitude of the growth oscillation that the Cu nuclei in the first layer do not give rise to preferential nucleation in the second layer. The Ni adatoms landing on top of the growing Ni islands with a Cu nucleus in the center are not trapped at the contact line between the Cu and Ni, but are efficiently diffusing over the step edge to fill the first layer.

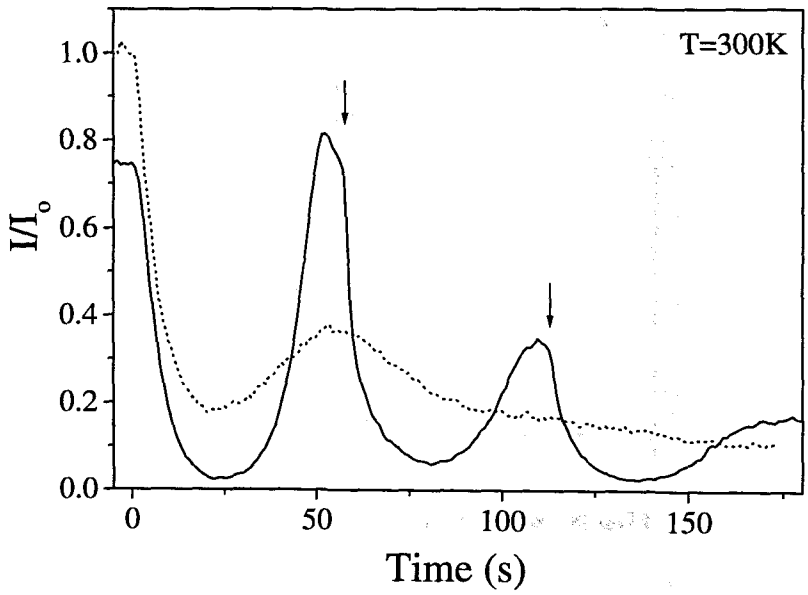

Figure 3.13: Normalized anti-phase He intensity during deposition of Ni at 300 K. Sputter pulses of $4*10^{17}$ ions/m^2 were given before deposition and at times indicated by arrows in the graph.

Growth manipulation by ion bombardment was also used to grow several layers in layer-by-layer fashion. Before deposition and during deposition at maxima of the reflected anti-phase He intensity, i.e., at layer completion, ion pulses of $4*10^{17}$ ions/m^2 were given. As can be seen in Fig. 3.13, this leads to clear oscillations. In this way the island density is enhanced in each new layer and the film grows two-dimensionally. Compared to the unmanipulated growth at that temperature, the film has a better filling of the lower layers, as can be concluded from the higher anti-phase intensity upon monolayer completion. The unmanipulated film grows in a multilayer mode which leads to many open layers even in thin films. Similar results are obtained for all growth temperatures tested, between 250 and 350 K.

Anti-phase SPA-LEED profiles of the (00)-spots taken from films grown with

the aid of sputter pulses showed no sixfold star-like pattern, but a round and sharp peak as expected from a flat film. With a FWHM of the (00) spot of only 1.4% SBZ manipulated films of the thickness of 2 ML were of much higher quality compared to the ones naturally grown, which display a FWHM of 2.5% SBZ. A similar film flatness could be achieved by unmanipulated growth only when the temperature is chosen well above the intermixing temperature, e.g., natural growth of a 2 ML Ni film at 440 K results in a FWHM of the (00) spot of 1.3% SBZ. One should not forget, though, that these films are covered with a Cu cup-layer and that due to the up-sweep of Cu the interface between Ni and Cu is most likely neither sharp nor flat.

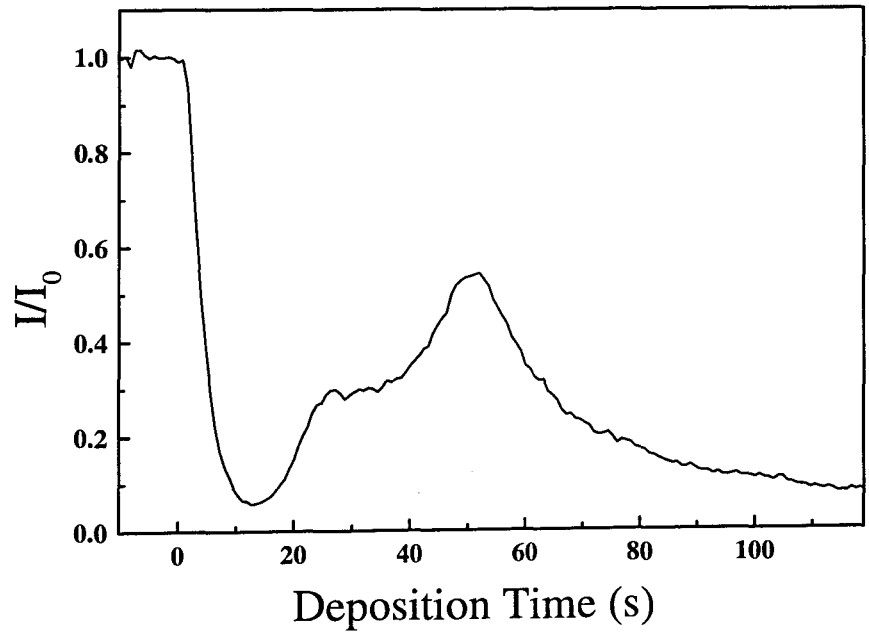

Figure 3.14: Normalized He anti-phase intensity as a function of Ni deposition time at $T = 300$ K onto a surface which was treated by O_2 pre-exposure of 18 Langmuir.

Besides natural and manipulated growth of Ni on Cu(111) we also tried to change the growth mode by using oxygen as a surfactant. In the best results two-dimensional growth was obtained for the first layer (see Fig. 3.14). After that, the surface of the film roughens very quickly. In no cases, the films were as smooth as those obtained with growth manipulation (rate variation and pulsed ion beam assisted growth). The use of oxygen as a surfactant is by far inferior to the kinetic growth manipulation methods and only leads to reasonably good results for the first monolayer and hence is of no practical use.

As a conclusion it can be said that Ni on Cu(111) grows three-dimensionally

rough below the intermixing temperature and that growth manipulation by the concept of two mobilities does overcome this and leads to layer-by-layer growth below this temperature. The layer filling obtained by these methods is much better than that by conventional growth, resulting in flatter surfaces. Also the defect density on the surface is lower. A comparison between pulsed ion beam assisted deposition at intermediate temperatures and unmanipulated growth at elevated temperatures is in clear favour of the first one, although some interface roughening may be caused by the sputtering. Further, it has been demonstrated that the use of a second evaporator, which performs nucleation in a pulse of very high deposition rate, also promotes layer-by-layer growth. In principle, an even higher rate during nucleation should lead to similarly good results as pulsed ion beam assisted deposition, but without the side effects of interface roughening and intermixing, making this recipe to the method of choice in heteroepitaxial growth manipulation.

Bibliography

[1] K. Meinel, M. Klaua, H. Bethge, J. Cryst. Growth **89**, 477 (1988)

[2] P. C. Dastoor, J. Ellis, A. Reichmuth, H. Bullman, B. Holst, W. Allison, Surface Review and Letters **1**, 509 (1994)

[3] E. Bauer, Appl. Surface Sci. **11-12**, 479 (1982)

[4] G. Ehrlich, F. G. Hudda, J. Chem. Phys. **44**, 1039 (1966)

[5] R. L. Schwoebel, E. J. Shipsey, J. Appl.Phys. **37**, 3682 (1966)

[6] G. Rosenfeld, R. Servaty, C. Teichert, B. Poelsema, G. Comsa, Phys. Rev. Lett. **71**, 895 (1993)

[7] G. Rosenfeld, B. Poelsema, G. Comsa, J. Cryst. Growth **151**, 230 (1995)

[8] G. Rosenfeld, N. N. Lipkin, W. Wulfhekel, J. Kliewer, K. Morgenstern, B. Poelsema, G. Comsa, Appl. Phys. A, **61**, 455 (1995)

[9] W. Wulfhekel, N. Lipkin, J. Kliewer, G. Rosenfeld, L. Jorritsma, B. Poelsema and G. Comsa, Surf. Sci. 348, 227 (1996)

[10] S. Esch, M. Breeman, M. Morgenstern, T. Michely and G. Comsa, Surf. Sci. **365**, 187 (1996)

[11] U. Gradmann, Ann. Physik **13**, 213 (1964)

[12] D. W. Gidley, Phys. Rev. Lett. **62**, 811 (1989)

[13] J. Zhang, Z. L. Han, S. Varma, Surf. Sci. 298, 351 (1993)

[14] S. P. Tear and K. Röll, J. Phys. C **15**, 5521 (1982)

[15] F. Huang, M. T. Kief, G. J. Mankey and R. F. Willis, Phys. Rev. B **49**, 3962 (1994)

[16] S. Yang, M. Yu, G. Meigs, X. H. Feng and E. Garfunkel, Surf. Sci. **205**, L777 (1988)

[17] B. Poelsema, G. Comsa, Scattering of Thermal Energy Atoms, Springer Tracts in Modern Physics **115**, Springer, Berlin 1989

[18] B. Poelsema, G. Mechtersheimer, G. Comsa, Surf. Sci. **111**, 519 (1981)

[19] M. Henzler, Appl. Surf. Sci. **11/12**, 450 (1982)

[20] J. Wollschläger, J. Falta and M. Henzler, Appl. Phys. A **50**, 57 (1990)

[21] J. A. Venables, Phil. Mag. **27**, 697 (1973)

[22] J. A. Venables, G. D. T. Spiller, M. Hanbücken, Rep. Prog. Phys. **47**, 399 (1984)

[23] K.Morgenstern, Besenbacher and Nørskov, private communication

[24] P. Stoltze, J. Phys. Condens. Matter 6, **9495** (1995)

[25] M. Bott, M. Hohage, M. Morgenstern, T. Michely and G. Comsa, Phys. Rev. Lett. **76**, 1304 (1996)

[26] Y.F. Liew, Y.L. He, A. Chan and G.C. Wang, Surf. Sci. Lett. **273**, L461 (1992)

[27] K. Lenarčič-Poljanec, M. Hodošček, D.Lovrić and B. Gumhalter, Surf. Sci. **251/252**, 706 (1991)

[28] Elastic constants for single crystal Ni were taken from American Institute of Physics Handbook, third edition, edited by D.E. Gray (McGraw-Hill Book Company, New York 1972)

[29] T. Michely, M. Hohage, M. Bott and G. Comsa, Phys. Rev. Lett. **70**, 3943 (1993)

[30] M. Henzler, private communication

[31] K. Morgenstern, G. Rosenfeld, G. Comsa, Phys. Rev. Lett.**76**, 2113 (1996)

[32] T. Michely, G. Comsa, Phys. Rev. B. **44**, 8411 (1991)

[33] M. Breeman, D. O. Boerma, Surf. Sci. **278**, L110 (1992)

[34] T. Michely and C. Teichert, Phys. Rev. B **50**, 11156 (1994)

[35] S. Esch, M. Bott, T. Michely and G. Comsa, Appl. Phys. Lett. **67**, 3209 (1995)

[36] W. Wulfhekel, I. Beckmann, N. Lipkin, G. Rosenfeld, B. Poelsema, G. Comsa, Appl. Phys. Lett. **69**, 3492 (1996)

Chapter 4

Heteroepitaxial Growth of Si on Ge(100)

4.1 Introduction

In the last decade, silicon-germanium heterostructures have received much attention. These heterostructures allow the creation of an entirely new class of materials based on modulated band-gap engineering and modification of the band properties due to strain. For technical applications of these heterostructures, flat stacks of layers with chemically sharp interfaces are desirable [1, 2]. A lot of effort has been put in finding the best deposition method and parameters and even the use of different surfactants to achieve that goal [3, 4, 5, 6, 7, 8, 9]. It is well established that the growth mode of Ge films on Si surfaces is of the Stranski-Krastanov type, i.e., that after the formation of a coherent pseudomorphic film with a thickness of a few monolayers 3D cluster formation takes place [5, 10]. Interestingly, the growth of Ge on Si has been studied in great detail - especially with STM [10, 11, 12, 13, 14, 15], whereas the growth of Si on Ge has received much less attention. This is remarkable because both interfaces are of equal importance in Si/Ge superlattices. In this chapter, we address only one of the two occurring growth situations during production of Ge/Si superlattices, namely the growth of Si on Ge(100). Besides the general kinetic problems to grow flat films and the problems due to the large misfit of 4.2% between Si and Ge, the trend of intermixing of the two materials additionally complicates the production of the desired films in this configuration, making it a more challenging task. From x-ray photoelectron spectroscopy (XPS) it is known that segregation of Ge to the growth front sets in around 525 K and becomes substantial (20% of the surface atoms) around 730 K [16]. The growth of Si on Ge(100) is studied from submonolayer coverages up to films as thick as 10 ML. From the growth kinetics observed at low coverages, a method is derived to grow flat films at low temperatures to limit interdiffusion.

The experiments were carried out in an UHV chamber with a base pressure below 1×10^{-10}mbar. The Ge(100) samples were cleaned ex-situ using ultra clean

isopropanol and were thoroughly out-gassed in UHV followed by cycles of sputtering with Ar^+-ions and annealing to 1100 K until practically no defects could be detected with STM. Samples were resistively heated. The sample temperature has been calibrated versus heating current using a Ni-CrNi thermocouple at low temperatures and a pyrometer at high temperatures [17]. In order to avoid contamination of the surfaces, the samples used in all STM measurements presented here have never been in direct contact with metals except for the Mo sample holder. This procedure allows the preparation of almost defect free surfaces but sample temperatures cannot be measured directly at temperatures not accessible to pyrometers. At these temperatures, the calibrated heating current is used to determine sample temperature. This results in some uncertainty in sample temperatures (typically 10K at 450K [17]). After surface preparation, Si was deposited at different substrate temperatures from a resistively heated Si wafer followed by imaging of the films in-situ with a commercial STM at room temperature. All STM scans are taken in non differentiated constant current mode.

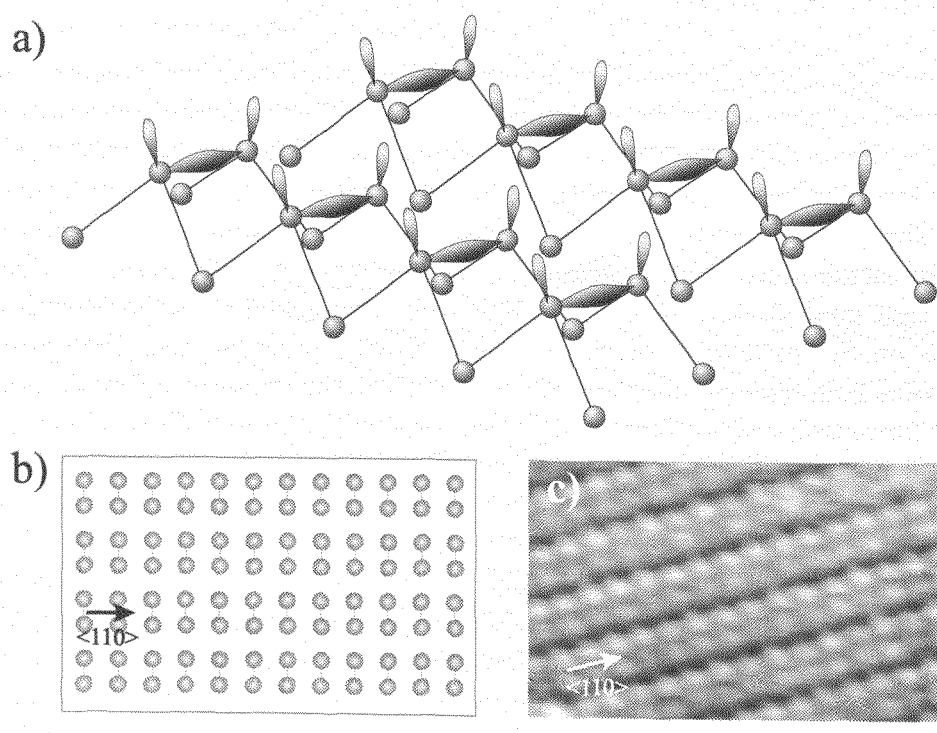

Figure 4.1: a) Three-dimensional model of the dimerised Ge(100) surface. b) Top view on the model showing the dangling bonds c) High resolution STM image. Size : 80 x 50 Å, Tunneling parameters : 0.16 V, 0.4 nA

Similar to the (100) surface of silicon, also the Ge(100) surface reconstructs into dimer rows. A schematic view of the (2x1) reconstruction can be seen in Fig. 4.1a. Two adjacent Ge surface atoms reduce their numbers of dangling bonds by building a

covalent dimer bond. Two, half filled orbitals per dimer protrude out of the surface. Due to the dimerisation, the dimerised surface atoms move slightly towards each other resulting in parallel rows of dimers running along <110> directions. Fig. 4.1b and c present a schematic top view of the dangling bonds as well as an STM scan of the reconstructed surface. For the STM scan, the tunneling voltage was chosen to lie in the bandgap and in between the two states (filled and empty) associated with the dangling bonds. So the highest contrast was achieved for the dangling bonds of the individual atoms, while the bonding and anti-bonding states of the dimer bonds were not imaged (for a detailed discussion of the surface states of Ge(100) see ref. [18]).

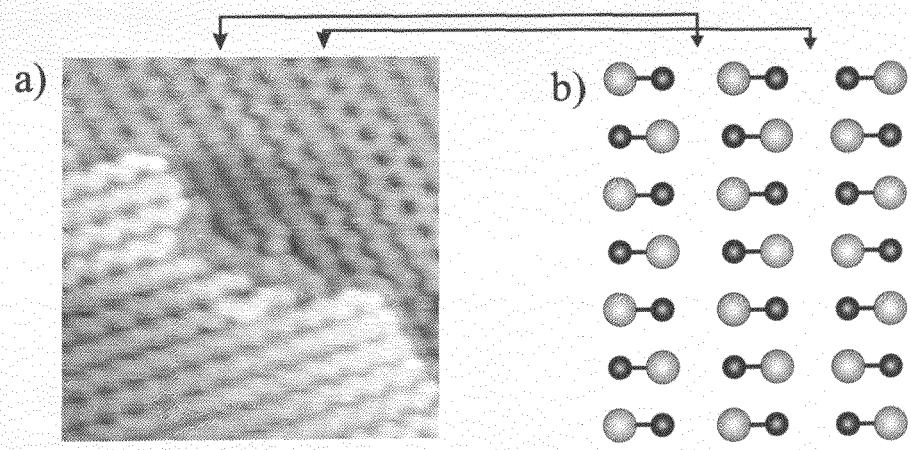

Figure 4.2: a) STM image and b) schematic drawing of the buckling of the (2x1) reconstructed Ge(100) surface. Size : 150 x 150 Å, Tunneling parameters : 1.6 V, 0.4 nA

The surface energy may be further reduced by buckling of the the dimers, i.e., the dimer bond is slightly tilted with respect to the surface plane [19]. Adjacent dimers in the same dimer row are usually buckled in the opposite direction. Fig. 4.2 displays the buckling of dimers. In the STM scan (see Fig. 4.2a) regions of buckled dimer rows as well as unbuckled dimer rows appear. Here, the tunneling parameters were chosen such that the upward buckled dangling bonds appear bright [18]. The unbuckled areas are either indeed unbuckled or, what is more likely, they flip very rapidly such that the STM only 'sees' the average of unbuckled dimers [19]. The statically buckled areas show two different possible orders. Either adjacent dimer rows are buckled in-phase or out-of-phase, as indicated in the model (see Fig. 4.2b).

Further, Fig. 4.2 illustrates that, due to the two fcc sublattices of the diamond structure of Ge, adjacent terraces display alternating a (2x1) and a (1x2) reconstruction. Dimer rows on adjacent terraces run perpendicular to each other. As a

result of this, two types of monatomic step edges occur. The type A step runs along the dimer rows of the upper terrace, while type B runs perpendicular to them.

As many studies have shown, the reconstruction leads to an anisotropic ad-atom and ad-dimer diffusion as well as sticking to A and B steps on Si(100) [11, 20, 21, 22, 23, 24, 25, 26]. Similar effects are likely to be present on Ge(100) leading to a very complex kinetic situation during growth. Some of these aspects will be addressed in this chapter.

4.2 Dimers and Clusters

In this section we study the initial steps of Si growth on Ge(100) at room temperature to extend the detailed studies of growth kinetics, nucleation and elementary diffusion processes also to the second interface present in Ge/Si heterostructures.

In principle four different isolated and high symmetry adsorption sites for Si ad-dimers exist on the (2x1) reconstructed Ge(100) surface (see Fig. 4.3). In the following, we want to focus on the identification of these configurations as well as their energetics and kinetics.

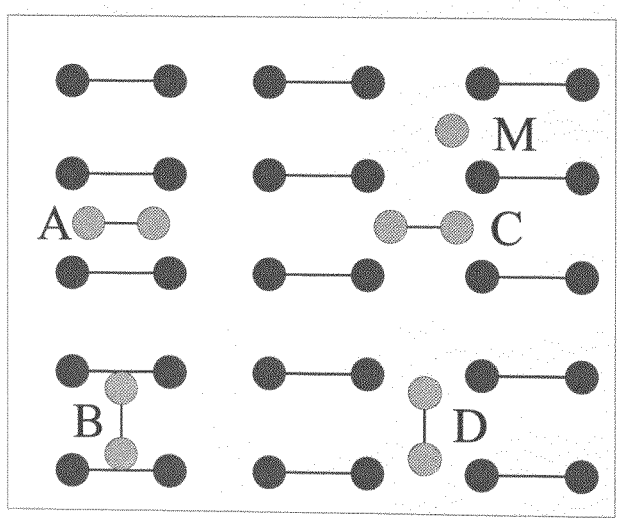

Figure 4.3: Schematic drawing of the (2x1) reconstructed Ge(100) surface atoms (black) and Si dimers (gray) in high symmetry position on the surface. Also the M adsorption site for an isolated adatom is indicated.

After cleaning of the surface and cooling to room temperature, small amounts of Si were deposited at room temperature. After deposition, the samples were transferred in-situ to the STM stage for imaging. In order to identify the deposited clusters properly, STM movies at both positive and negative polarity have been

taken. Occasionally, we have found rearrangement events in our STM movies which helped us to identify some specific ad-clusters.

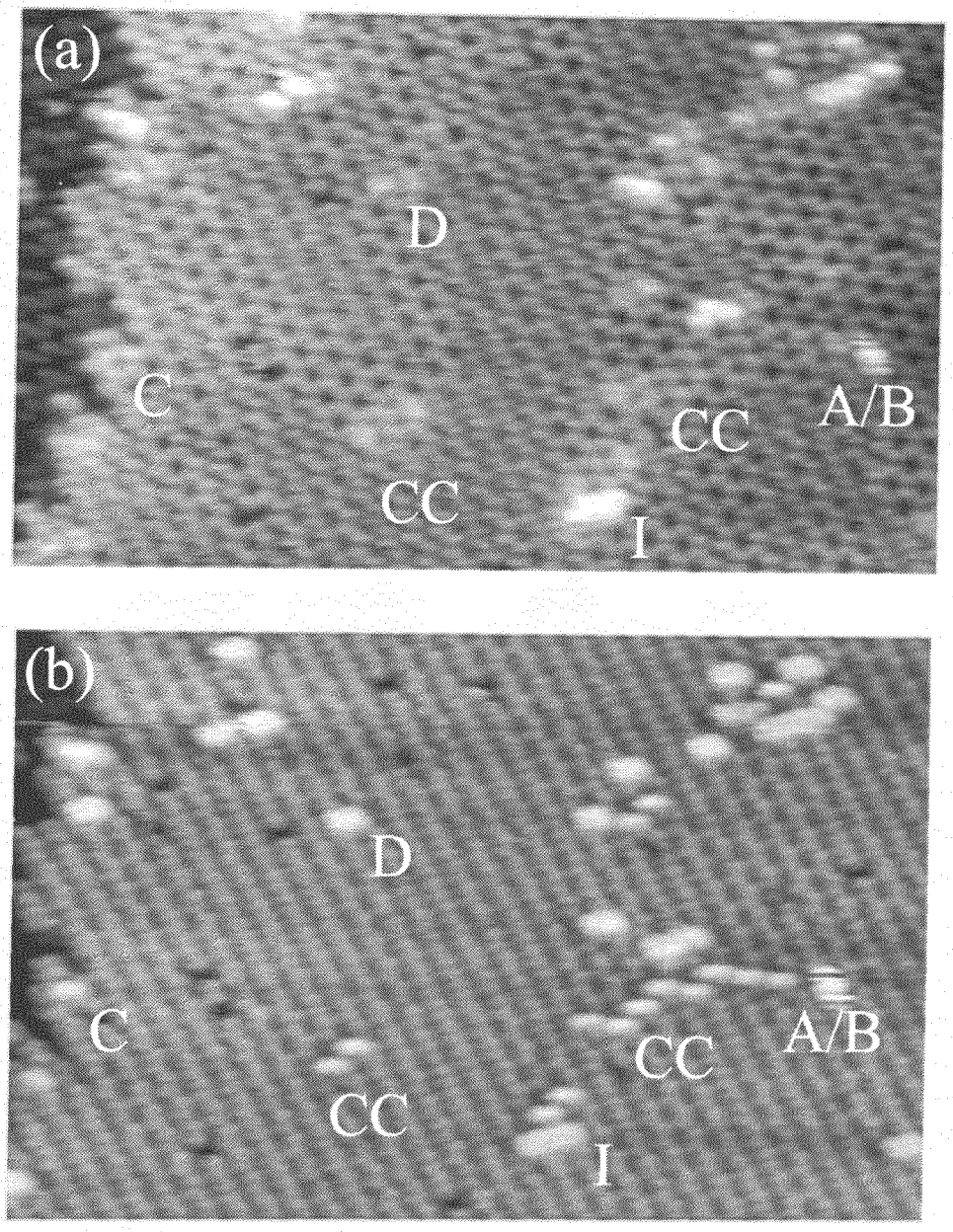

Figure 4.4: a) Filled and b) empty state images of Ge(100) after deposition of ≈ 0.01 ML Si at 300K. Sizes : 380x220Å. Tunneling parameters: a) 1.6V, 1nA; b) -1.6V, 1nA

In Fig. 4.4, filled and empty state STM images of the same area of the sample after deposition of ≈0.01 ML at 300 K are shown. The buckled and unbuckled

substrate dimer rows of the (2x1)-Ge substrate are clearly visible in the filled state image. In the empty state images presented, the substrate dimer rows appear similar, but the downward buckled dangling bonds appear bright [18, 27], i.e., the dimer rows appear with inverted contrast.

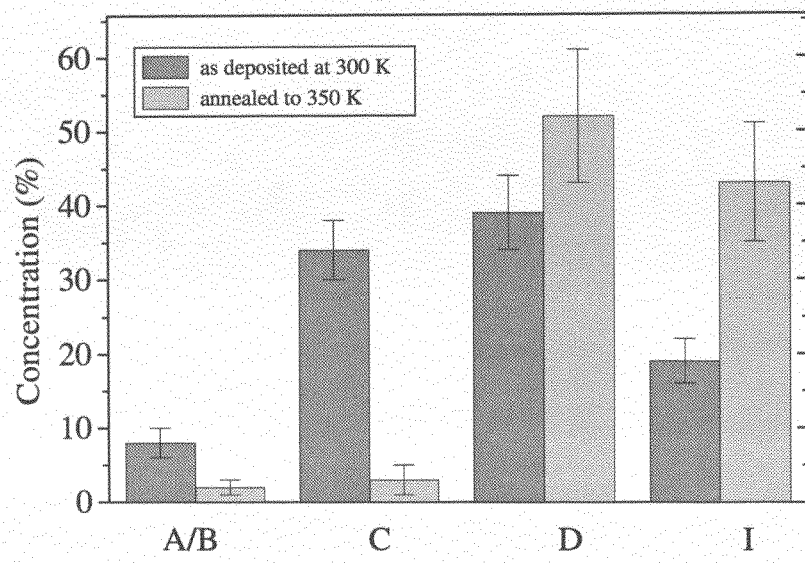

Figure 4.5: Coverage of A/B, C, D and I in percent of the deposited material after deposition of 0.01 ML at 300K and after annealing to 350 K for 5 minutes.

A variety of different clusters of Si atoms can be found on the surface. These clusters are absent before deposition and are labeled. In the following discussion, we will identify the observed clusters with those of Fig. 4.3. No evidence for single isolated Si adatoms has been found, suggesting that the deposited Si adatoms either diffuse easily at room temperature, exhibit a substantial amount of transient mobility or are moved away by the tip during tunneling. Although at low temperature (160 K) isolated Si adatoms and pairs of Si adatoms coupled via a substrate mediated interaction have been observed on Si(100) [28], the smallest observed isolated features which evolve after deposition at or above room temperature are dimers [29, 30]. Similar to MBE of Si on Si(100) [11] and Ge on Si(100) [20], strings of epitaxially oriented dimers, i.e., one dimensional islands (I) of alternating D and B dimers, are formed that clearly show up in both filled and empty state images. These islands are elongated perpendicular to the substrate dimer rows. Only 19% of the deposited material is found in these islands at room temperature at this low coverage[1] (see Fig. 4.5). When deposition is carried out at elevated temperatures

[1]Populations of the different species have been determined by identifying all features on large

(400K) these islands of epitaxially oriented dimers are the predominant species on the surface similar to the growth of Si and Ge on Si(100) [11, 20, 21]. Also, smaller bright features A/B, clearly visible in both filled and empty states, are present lying centered on top of a substrate dimer row, which are identified as individual Si ad-dimers of either type A or B. Similar dimers are also found after room temperature growth of Si on Si(100) [29]. With 8% of the total coverage, they play a minor role in condensation of the deposited adatoms (see Fig. 4.5). Obviously, these dimers are not static during scanning but seem to be mobile, either thermally or tip induced as can be seen from the strong variation of their shape from scanline to scanline. However, the surface is dominated by other features, that only faintly appear in the filled state image, but are clearly visible in the empty state images. These features can be divided into two groups. First, isolated structures of type D are found. In the filled state image, they extend over two substrate dimer rows as a faint disturbance of the dimer rows. In the empty state image, they seem to be centered between two dimer rows. Second, larger features (labeled CC), appearing as strings or worms of faint contrast change in the filled state images, are often seen. In the empty state image, they consist of bright, small features, that are elongated perpendicular to the substrate dimer rows and are centered between the rows of the substrate. Along the dimer rows, they are roughly one dimer wide. They are always separated by one dimer unit perpendicular to the substrate dimer rows and one dimer unit along the dimer rows, i.e., they form strings along the <130> directions.

Figure 4.6a,b displays these two types of features in more detail. The isolated feature D appears round and extends over two dimer rows in the filled state image. The empty state image clearly shows that the structure is elongated along the substrate dimer rows and is most likely a Si dimer in epitaxial orientation lying in between two substrate dimer rows (Type D dimer). Taking this into account, the filled state image of the type D dimer can easily be explained by a change in the buckling registry of the substrate dimer rows induced by the D dimer, as also visible in Fig. 4.4a. The Si dimer in between the rows causes the four adjacent Ge atoms of the two substrate dimer rows to recede into the surface and the corresponding four other Ge atoms of the four substrate dimers to buckle upwards, resulting in a ring like feature in the filled state image with a faint additional intensity in the middle caused by the Si dimer itself. This is further substantiated by the filled state STM image of Fig. 4.6c.

In the case of Si/Si(100), isolated D dimers have not been observed [31] indicating, that they are energetically unfavourable. In the case of Si/Ge(100), though, we find them frequently (39% of the deposited material). Hence, in contrast to Si/Si(100), they play a significant role during nucleation of islands, especially, because they have the correct orientation that is needed to form I islands. In addition, after deposition at 350K, the isolated dimers predominantly present on the surface are D dimers. Annealing of structures deposited at room temperature to 350K,

scans of both polarities.

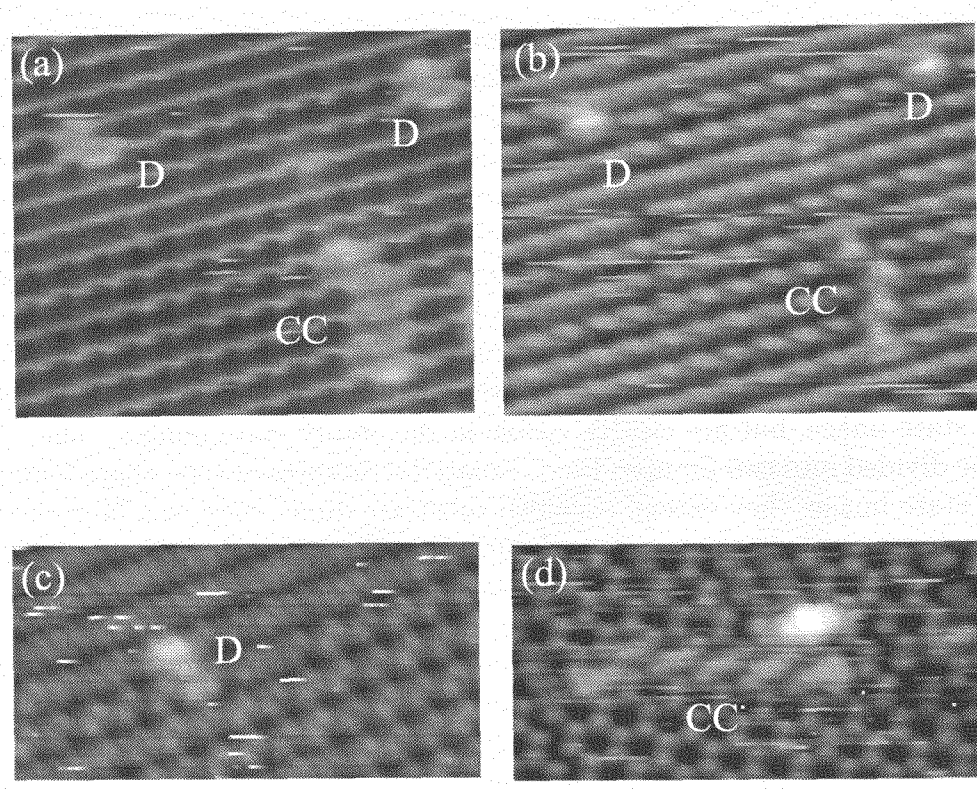

Figure 4.6: a) Filled and b) empty state images of Si clusters. Size : a),b) 150x120Å; c),d) 140x70Å. Tunneling parameters: a),c),d) 1.6 V, 0.4nA; b) -1.6V, 0.4nA.

results in an increase of the population of D dimers to ≈50% of the deposited material (see Fig. 4.5), indicating that the D configuration is the dimer configuration of lowest energy.

The string like structure CC cannot be identified that simply. It is clear from the empty state image of Fig. 4.6b, that the strings cannot be explained by simply clustering D dimers, since neither the intensity nor the shape of the individual features of the CC structure resemble a D dimer. Moreover, the width and height of the individual perturbations along the substrate dimers measured exactly in between two dimer rows is significantly smaller than that of the D type dimer (see Fig. 4.7). On the other hand, the ends of the string in the filled state images look similar to the ring like features of the D dimers. It seems to be more likely, that the CC cluster consists of either non epitaxially oriented dimers (C dimers) or Si adatoms, that lie in the M position. Also from other high resolution filled state scans (see Fig. 4.6d), it cannot be unambiguously decided, if these clusters are build up by C dimers or adatoms. To clarify this, we expand our study also to the dynamics of the observed features by taking STM movies at room temperature.

Fig. 4.8 represents an excerpt of such a movie, where during the movie, the polarity of the scan was frequently changed to obtain information in both filled and

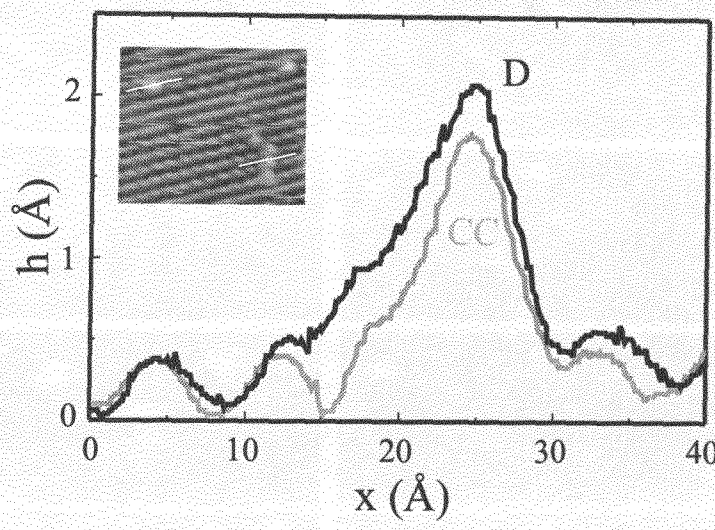

Figure 4.7: Linescans along the substrate dimer row direction over a D and CC cluster centered in between the substrate dimer rows as illustrated in the inset. Tunneling parameters: -1.6V, 1nA

empty states. Due to the frequent switching of polarity, the resolution of the scans is limited and not as good as in Fig. 4.6, but the surface features can still be clearly identified. First, we focus on a cluster consisting of three small individual parts labeled CC_b. During the first half of the movie, i.e., Fig. 4.8a-f, the cluster stays unchanged. Then, between Fig. 4.8f and g it collapses and creates two features, one on the lower side, that remains unchanged during the further scans and a mobile feature positioned on the upper side. In both polarities, the lower feature shows up brightly, ruling out a type D dimer. Further, Fig. 4.8i and j clearly show, that the feature is neither centered on top nor in between the substrate dimer rows, ruling out an A/B dimer. Further, it seems to extend from an on top position to a position between the substrate dimer rows. Hence, the lower feature can be identified as a small island of two epitaxially oriented Si dimers in a row, i.e., a BD structure. According to this, the upper feature of the collapsed structure should be a single dimer. In Fig. 4.8g one sees, that during one scan it stayed unchanged in the state that it was in the string CC_b. Since it is now an isolated feature, the observed shape is likely to be the real shape of the structure and it can be identified as a non-epitaxial dimer lying in between two dimer rows, i.e., a dimer of type C. It certainly can be ruled out to be a type D dimer, as it clearly distinguishes from the D_a dimer in Fig. 4.8a, d or f. Surprisingly, in the next image (Fig. 4.8h) the C dimer has diffused to an on top position (and hence becomes a bright A/B dimer) and starts to diffuse

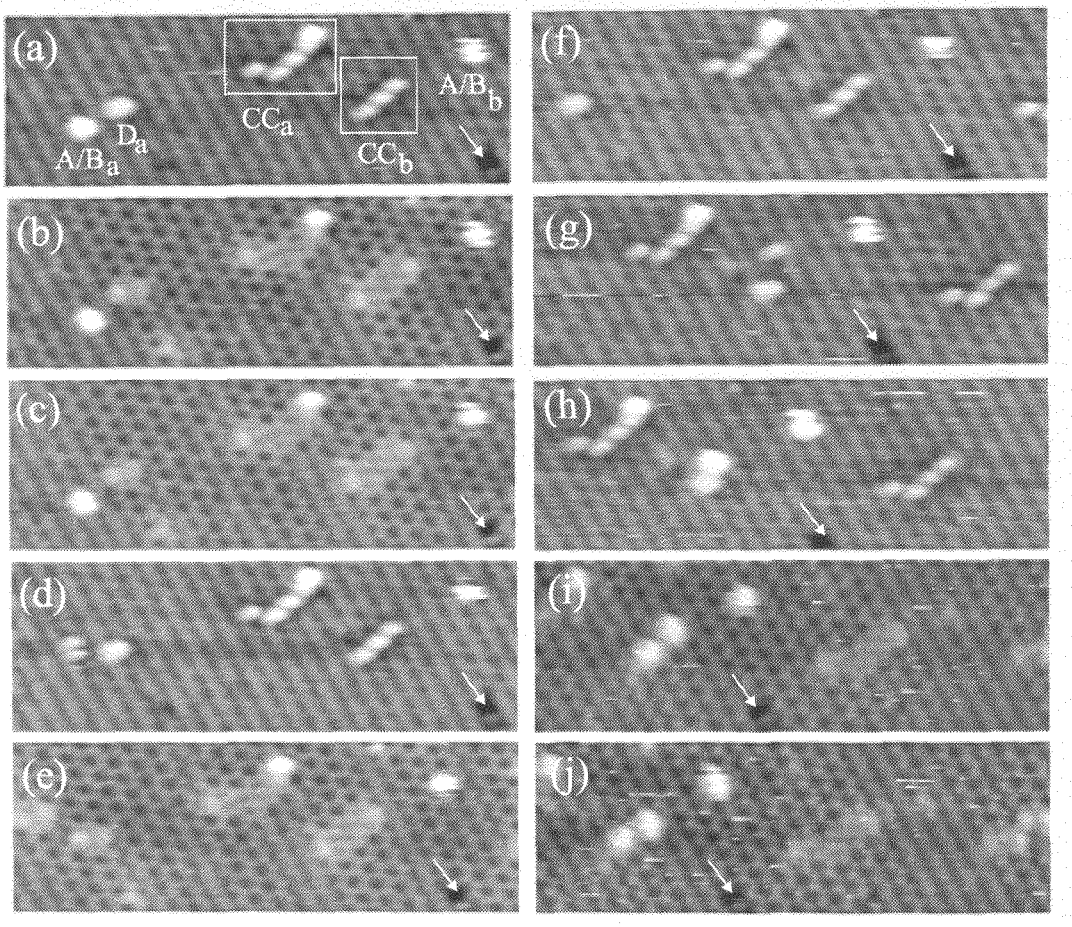

Figure 4.8: Successive scans of the same area (300x100Å) of filled b), c), e), i), j) and empty state a), d), f), g), h). Time between images : 150 sec. Tunneling parameters: ±1.6 V, 0.4 nA. Some drift is indicated by an arrow pointing at an immobile missing dimer defect.

along the substrate dimer row. This observation also explains, why practically no isolated type C dimers are found. They are thermally unstable and transform into A/B dimers and diffuse away or rotate to a more stable D configuration. At room temperature, they can only be observed in clusters , i.e., the CC structure, or very rarely in the vicinity of a missing dimer defect or other defects like on the left hand side of Fig. 4.4. It can be ruled out clearly that the CC structure is a cluster of single adatoms, since the observed structures after the collapse are incompatible with one dimer and one adatom. The lower feature cannot be a dimer and the upper one diffuses only slowly on top of the substrate dimer row in agreement with dimer diffusion and is clearly visible in both states, also characteristic for an A/B dimer in contrast to an adatom [32].

Similar clusters of C dimers have also very recently been seen in the homoepitaxial system of Si [31]. However, the CC clusters of Si dimers on Ge(100) are metastable at room temperature and eventually collapse into epitaxially oriented islands. To clarify, in how far the collapse is thermally activated or tip assisted, we carried out simple annealing experiments. First, 0.02 ML of Si was deposited at room temperature and STM scans were taken, showing a high density of CC clusters. In a second step, the sample was heated to 350 K outside the STM for 5 minutes and then was directly reinserted into the cold STM. After this short and mild annealing, practically no CC structures could be found on the surface anymore (for the population of C dimers before and after annealing, see Fig. 4.5). Similarly, after deposition of 0.02 ML of Si on a sample at 350 K, CC clusters were absent on the surface. These observations clearly proof the thermal instability of the CC clusters. In addition, also the kinetic barrier for the collapse can be estimated from these observations. Obviously, 5 min annealing at 350 K leads to at least one thermally activated jump per C dimer. On the other hand, from many STM movies, an upper limit of $\approx 10^{-5}$ Hz for the jump frequency at 300 K can be obtained (less than $\approx$5% of the CC clusters decay in two hours of observation). These upper and lower bounds of the jump frequency allow us to estimate the activation energy E_c for the rate limiting diffusion step of the CC cluster collapse as a function of the attempt frequency ν_0. Since the two limiting lines for E_c defined by the bounding jump frequencies cross when ν_0 is varied, it can be concluded, that ν_0 has to be larger than $\approx 10^{11}$Hz and E_c larger than 0.95 eV, allowing an error of 10K for the annealing temperature. For a typical value of ν_0 of $\approx 10^{12.8\pm1.3}$ Hz, as has been observed for Si dimer diffusion on Si [23], E_c can be quantified to be 1.1±0.1 eV.

To explain the high concentration of the CC clusters (34% of the deposited material) one has to consider the kinetics of the formation of such structures. Presuming, that two adatoms on neighboring rows diffuse along the rows by hopping from M position to M position [33] they eventually meet to form a C dimer. If no more adatoms arrive, the C dimer will transform into a stable D dimer or an A/B dimer. However, when additional adatoms diffuse along one of the two adjacent substrate dimer rows, it might be trapped in a precursor state one hop away from the C dimer [31], lowering the total energy of the three adatom system and hence stabilizing the system. The addition of a fourth adatom then leads to the formation of a CC cluster. Due to their large population on the surface, the CC clusters play an important role in binding the deposited atoms and in nucleation during growth of Si on Ge(100). At elevated temperatures, where the CC clusters become unstable on the time scale set by the deposition rate, they may contribute much to the nucleation and formation of Si islands. Besides direct diffusion of adatoms or dimers across dimer rows, the collapse of the CC clusters also leads to some additional diffusion of material across rows direction promoting the growth of well ordered and closed films. In contrast to Si/Si(100) [30], no diluted dimer rows have been observed in our case. This suggests that either diluted dimer rows on Ge(100) are not stable at room temperature or that they are not formed since the state leading to the formation of the CC structure

is, due to the different strain field of Si on Ge(100) the state of lowest energy.

In addition to the decay of a CC cluster, the movie in Fig. 4.8 reveals also other information about typical elementary diffusion processes at room temperature. The dimer A/B_b is not static during the scans. It is moving or deforming during the relatively short period of time that it is scanned by the tip, resulting in a ragged appearance. On the other hand, the position of the dimer varies only slightly from scan to scan, although the time between scans is 400 times as long as the time between two scanlines (0.4 sec/scanline). Therefore, the observed changes in the A/B dimer are hardly due to thermal diffusion along the dimer row. The behavior can be explained by either a tip induced diffusion or rotation of the dimer, or a thermal rotation of the dimer between epitaxial orientation (type B) and non epitaxial orientation (type A) as has been observed for Si dimers on Si(100) on the time scale of seconds to minutes at room temperature [29, 30, 23, 33]. Following the general trend, that the kinetic processes on Ge(100) have a slightly lower barrier, it might well be that the observed ragged appearance is due to a thermal activated rotation. In addition to the ragged appearance of the A/B dimer, on longer time scales we observe diffusion of such dimers over larger distances along the substrate dimer rows. An example is marked by arrows in Fig. 4.9e-h. However, from many STM movies it seems that more diffusion events along dimer rows take place, when the fast scanning direction is chosen along the dimer rows. It seems that the diffusion is mostly not thermally activated but tip induced even at moderate tunneling conditions. Hence, we cannot extract an activation energy for this type of diffusion from our experiments.

Besides displacements of A/B dimers along the underlying Ge dimer rows also diffusion of dimers across substrate dimer rows has been observed. This diffusion process can be split into two steps. As can be seen in Fig. 4.8c-e, the dimer A/B_a first diffuses along the substrate dimer row and then falls in between the rows to finally become a D type dimer. In other movies it has been observed that a D dimer hops up from between two dimer rows onto a row and then starts to diffuse along the row. Two of these diffusion steps - from on top to in between and back to on top of a dimer row - may lead to slow diffusion across dimer rows, revealing the kinetic pathway for this kind of diffusion. An example of this kind of diffusion is marked by arrows in Fig. 4.9a-d, where an A/B dimer falls in between two dimer rows and later jumps back onto a dimer row. Hence, both diffusion steps necessary for mass transport across dimer rows are observed in one movie, though, in this particular case, no net transport occurs since the dimer jumps back on the same dimer row it has fallen from.

The intermediate state in between the dimer rows may seldom also be a type C dimer, as seen in STM movies or very recently during diffusion of Si across the dimer rows of Si(100) [34]. However, the C dimer is unstable and energetically unfavourable and immediately either hops again to a position on top of a substrate dimer row, similar to the isolated C dimer left over from the collapse of the CC_b cluster, or transforms to a D dimer, so that it is only present for one STM scan. In our STM

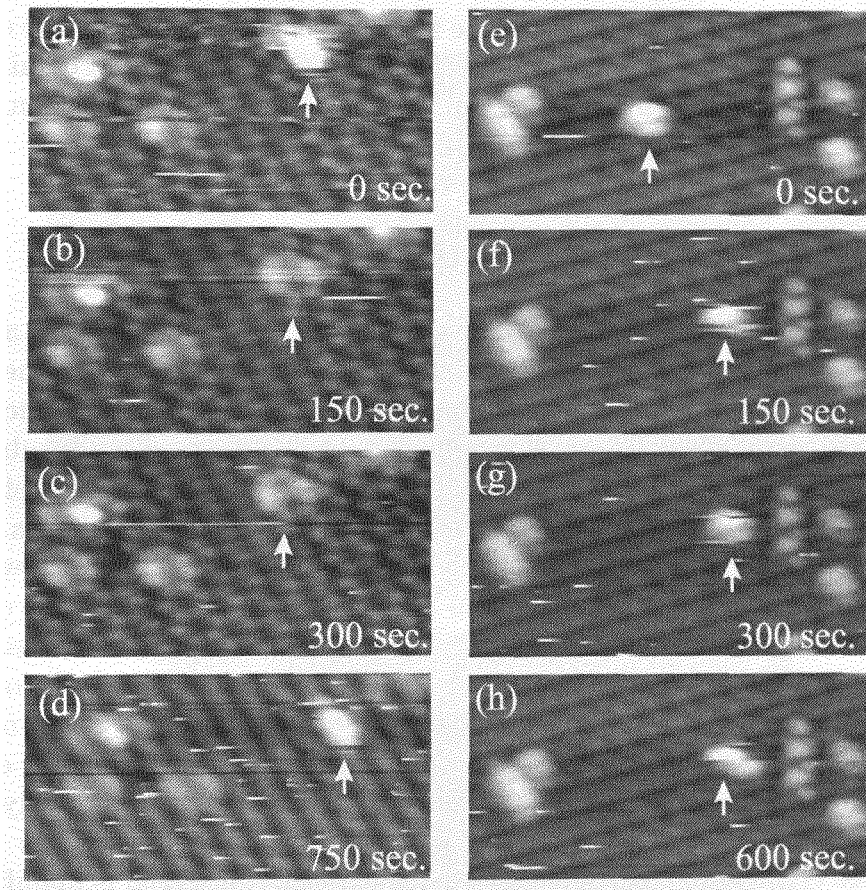

Figure 4.9: Two series of successive scans (160x80Å) of filled a)-d) and empty states e)-h). Relative times of the beginning of each scan are indicated. Tunneling parameters: ±1.6 V, 0.4 nA.

movies, it has never been seen to be stable for more than one scan (160sec./scan). Obviously, here the system Si/Ge(100) differs from Si/Si(100), where cross row diffusion in mostly takes place via C dimers in contrast to Ge/Si(100) where it takes place via D dimers.

Diffusion of dimers across dimer rows is intimately linked to the transformation between A/B and D dimers in the case of Si/Ge(100). From many STM movies, a lower limit of 0.93 eV for the activation energy of the transformation of an A/B dimer to a D dimer and hence for diffusion across dimer rows can be given, assuming $\nu_0 = 10^{12.8\pm1.3}$ Hz. An upper limit cannot be given, since we cannot exclude tip effects. The rate for the reverse process, for a D dimer to jump onto a neighboring row, is somewhat lower. This is in accord with annealing experiments to 350 K, after which the concentration of A/B dimers is very low (<2% of the deposited material), and the concentration of D dimers rises (see Fig. 4.5). An energy difference between A/B and D dimers, though, cannot be estimated from the annealing experiments, since there

may also be some loss of A/B dimers due to diffusion along the substrate dimer rows followed by incorporation at an island, cluster or step edge. More detailed studies of the energy difference between A/B and D dimers and about their transformation kinetics are needed to quantify dimer diffusion across dimer rows.

4.3 Nucleation and Growth of Islands

At temperatures above ≈400 K, Si film growth proceeds by nucleation and growth of islands, as can be seen in Fig. 4.10a. After deposition of 0.3 ML, the surface is covered with islands of Si dimer rows. The islands are elongated perpendicular to the underlying substrate dimer rows, similar to the islands observed after submonolayer growth of Si and Ge on Si(100) [11, 20, 22]. The island edge consists of long type A and short type B step edges. At these low temperatures, the islands are not in their equilibrium shape but the shape reflects the kinetics of island growth [11], as can be seen from the strong variations in the shape of the islands. Since diffusion of adatoms and dimers along the substrate dimer rows is faster than across the dimer rows (Si/Si(100) [21, 24, 25], Ge/Si(100) [20, 22, 37], Si/Ge(100) [35]), one expects the islands to be elongated in the direction opposite to the observed one, as the area, from which they can capture material is larger along the substrate dimer rows than perpendicular to them. This puzzling observation, though, is easily explained by an anisotropic sticking coefficient of adatoms. The coefficient is low for type A and high for type B step edges, such that the deposited material is mainly captured at the ends of the dimer rows of the growing islands. This has previously been experimentally observed for growth of Si and Ge on Si(100) [11, 20, 22, 26] and theoretically confirmed for Si on Si(100) [36].

Due to the (2x1) dimer reconstruction of the growing islands, two possible translational domain classes exist. Since neighboring islands nucleate independently, they do not necessarily belong to the same class. With 50% probability, they form different (2x1) domains and when they eventually coalesce during growth, an anti-phase boundary (APB) separates the two domains. An APB running perpendicular to the dimer rows of the two domains is marked APB1 in Fig. 4.10a. The same island also displays a APB running along the dimer rows. This type is found seldom in the early stages of monolayer growth, as the preferred growth direction of the islands leads to preferred coalescence of island at B type step edges. APBs running perpendicular to the dimer rows are known to serve as nucleation centres for next layer islands during Si homoepitaxy [39]. We find, that this is also the case for Si growth on Ge(100). An example is pointed out by APB2 in Fig. 4.10a, where the APB is decorated with a second layer dimer row.

To gain information about interlayer mass transport during island growth, Si was deposited at 475 K such that the first layer is almost completed (see Fig. 4.10b). At a total coverage of 0.92 ML Si, only 0.07 ML Si is found in the second layer[2],

[2]Coverages were determined from STM scans.

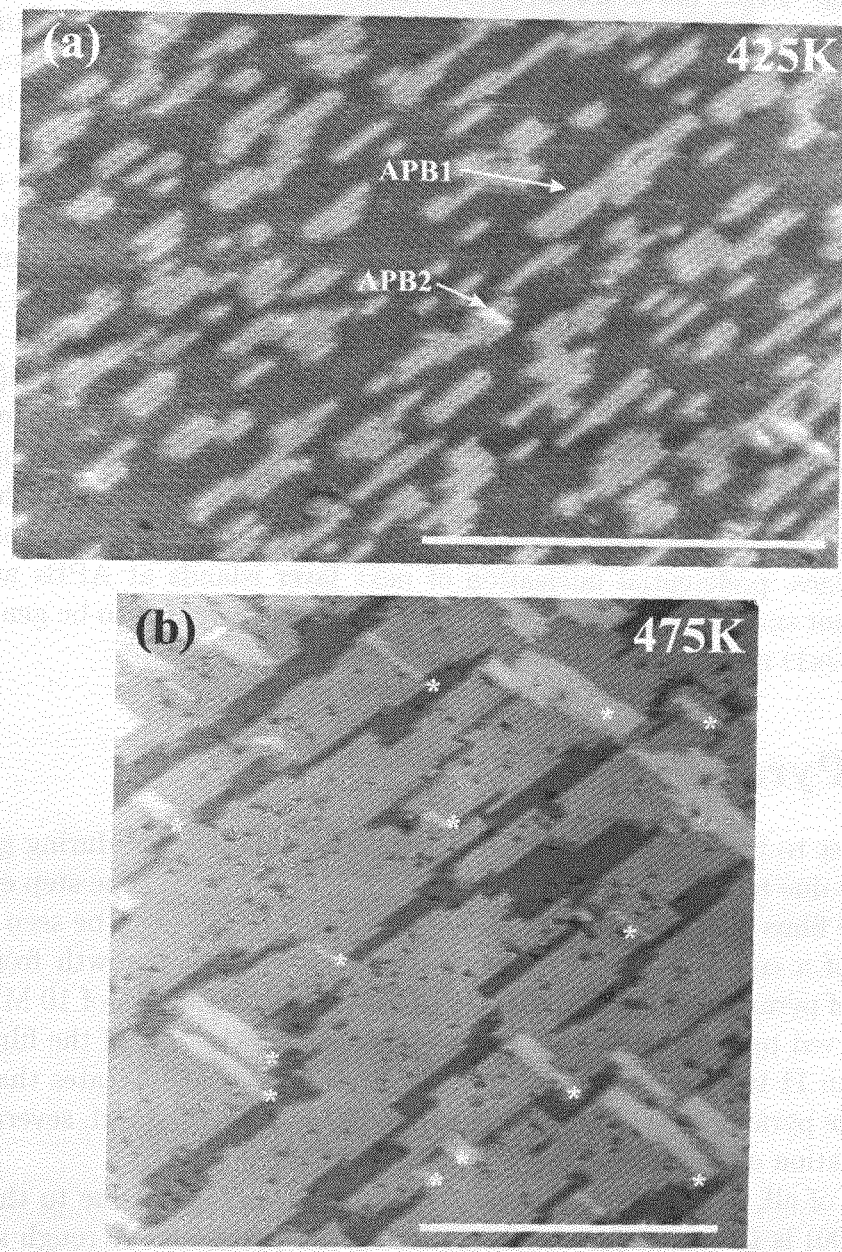

Figure 4.10: STM images of the surface after deposition of a) 0.3 ML, b) 0.92 ML with a rate of 1 ML/min. at substrate temperatures as indicated. The white bar represents 500Å. Second layer islands caused by nucleation at former APBs are marked by stars in b). Tunneling parameters: 1.6 V, 1 nA.

indicating a effective mass flow over the step edges of the growing islands. Focusing on the second layer islands, one notices that most of these islands (indicated by

stars in Fig. 4.10b) are situated at former APB of the underlying layer, i.e., they were formed by preferential nucleation at APBs of the first layer islands and not by homogeneous nucleation. Hence, in the absence of APBs, it is likely that the filling of the first layer would have been even higher and less second layer islands would have formed. Since diffusion mainly takes place along the dimer rows, one can conclude that the relevant step edge barrier in this system, i.e., the step edge barrier at B type step edges, is small or absent. In earlier STM studies of the denuded zone around step edges, Mo et al. also came to this conclusion for Si adatoms at B type step edges of Si(100) [20]. This was further substantiated by ab initio calculations for the same system [36].

From the strong similarities between Si as well as Ge growth on Si(100) and Si on Ge(100) we conclude, that the kinetic processes involved during growth in these systems are specific for the (2x1) dimer reconstruction. Fast diffusion of adatoms and dimers along dimer rows and slow diffusion across dimer rows, high sticking probability of adatoms to type B step edges and low sticking probability to type A step edges, preferential nucleation of next layer islands at APBs and no or an insignificant small step edge barrier at B type step edges seem to be general features of these (2x1) reconstructed systems.

4.4 Pyramidal Growth

In contrast to the efficient interlayer mass transport observed during growth of the first layer due to a small or vanishing step edge barrier at B type step edges, growth of thicker films leads to three-dimensionally rough films as can be seen in Fig. 4.11. Instead of a continuous layer-by-layer growth with a flat growth front, a regular pattern of pyramids is formed during growth. After deposition of 10 ML [3] at 525 K, the observed pyramids protrude up to ≈14 Å out of the rest of the film and locally more than 11 layers are exposed. In addition, Fig. 4.11 illustrates that the typical size of the pyramids rises with deposition temperature. A priori, several reasons for the formation of pyramids can be given.

First of all, one might conjecture that the strain energy due to the misfit of Si on Ge(100) is the cause for the formation of the pyramids. A rough surface would allow the higher layers of the film to release some of their strain and thereby reduce the strain energy. This implies that a thermodynamic drive is the cause for this phenomenon. Such a mechanism was found to be responsible for the formation of regular three-dimensional hut-clusters of Ge on Si(100) [10]. However, for the creation of the hut-clusters, much higher temperatures than those during our growth conditions were needed (≈ 700 K). Moreover, the Si islands are likely to equilibrate at even higher temperatures than Ge islands due to the stronger Si-Si bond indicating that the growth temperatures used in our experiment are much too low to allow

[3] Coverages beyond 1 ML were extrapolated from the deposition rate determined at coverages below 1 ML.

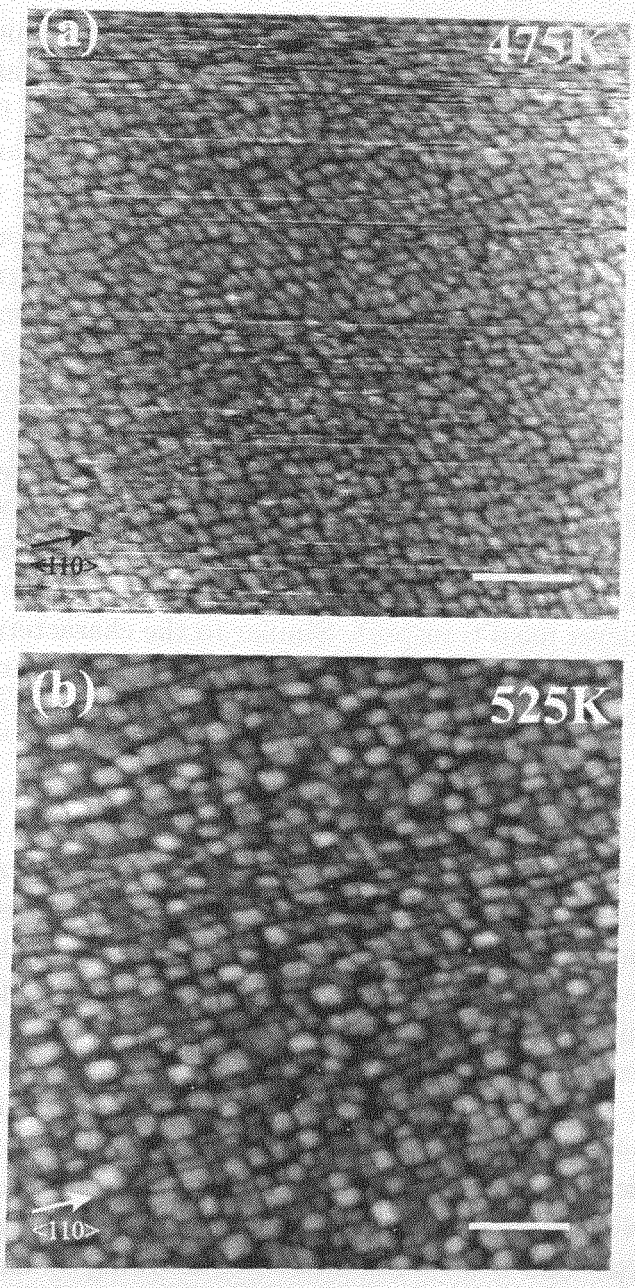

Figure 4.11: Filled state images of the surface after deposition of 10 ML Si with a rate of 1 ML/min. at substrate temperatures as indicated. The white bar represents 500Å. Tunneling parameters: 1.6 V, 1 nA. Contrast: 20Åfrom black to white.

efficient mass transport to thermodynamically build the pyramids. In addition, the orientation of the base of the Si pyramids run along the dimer row directions of the substrate, in contrast to those of the Ge hut-clusters which run under an angle of 45° to the dimer rows. Also the dependence of the pyramids size on growth temperature is a hint that the pyramids are of kinetic origin. Finally, neither annealing of a film

grown at 475 K to 525 K results in a change in the pyramids size nor a film of the same thickness, which is grown much flatter by growth manipulation, as will be shown later, splits up into pyramids during annealing to these temperatures. Hence, a thermodynamic reason for the formation of the pyramids can be ruled out.

Second, the mobility of adatoms can be a function of film thickness during heteroepitaxy [40]. A decreasing mobility with film thickness favours three-dimensional growth. Such a situation is also likely to be present during growth in this system, since Si adatoms on the 'soft' Ge(100) substrate should display a lower diffusion barrier than Si adatoms on a thick, 'hard' Si film. On the other hand, similar three-dimensional pyramids with the same orientation and similar size as in our case have also been observed during homoepitaxial growth of Si and Ge on their (100) face at similar temperatures [41, 42]. Hence, it seems that in all these cases - homoepitaxy of Si and Ge as well as heteroepitaxy of Si on Ge - the pyramids are caused by the same effect. In the homoepitaxial systems of Si and Ge, obviously the diffusion barrier does not change with film thickness. Some other kinetic mechanism seems to hamper interlayer mass transport. Similar to the characteristics of submonolayer island growth on the (2x1) reconstructed surfaces, the pyramidal growth at these temperatures seems to be a general property of these systems and is not related to strain.

To find out what kinetic process is responsible for the rough growth, we extend the study of growth scenario to coverages beyond 1 ML. During growth of the first monolayer, islands elongated perpendicular to the substrate dimer rows expand on the terraces. Interlayer mass transport is very efficient over the B step edges of the growing islands, so that nucleation of the second layer islands only sets in after coalescence. The islands coalesce predominantly at their B type step edges such that the surface is left with large, elongated vacancies in the first layer close to monolayer completion, as can be seen in Fig. 4.10b. The vacancies are terminated by long A type step edges and short B type step edges. During further growth, these vacancies are not filled very efficiently. Direct deposition into the vacancies only slowly fills them up and little material descends over the A type step edges into the vacancies due to the slow diffusion of material towards type A step edges. Also diffusion over the B type step edges contributes little to the filling of the vacancies due to the short length of the B step edges. After nucleation of the second layer islands, these islands expand perpendicular to the dimer rows of the first layer islands, i.e., their long axis is rotated by 90° in respect to the first layer islands. The expansion of the dimer rows of the second layer islands eventually stops when they reach a downward A step edge of the first layer islands as illustrated in Fig. 4.12. This is obvious, since the adatoms or ad-dimers diffusing on the first layer islands cannot reach the preferred absorption site at the B step edges of the second layer islands, anymore. So, the length of the second layer islands is initially limited by the width of the first layer. On the other hand, also material is deposited onto the second layer islands, especially, close to completion of the second layer. It quickly diffuses towards the B type step edges of the second layer island which are in fact often double steps

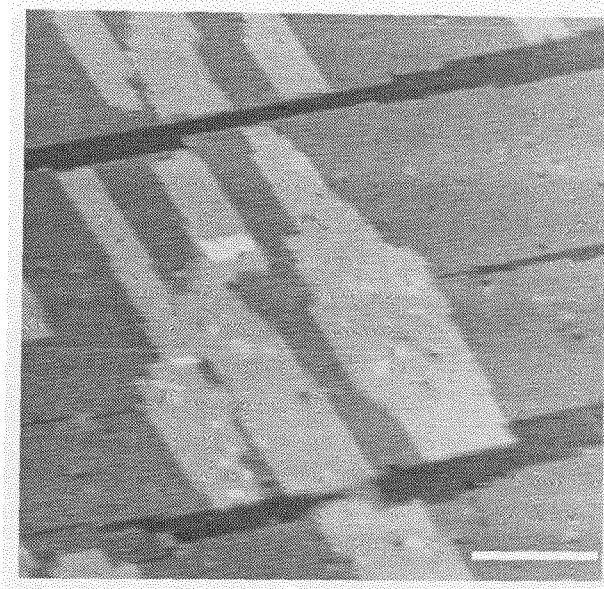

Figure 4.12: Filled state images of the surface after deposition of 1.3 ML Si with a rate of 1 ML/min. at 525 K. The white bar represents 200Å. Tunneling parameters: 1.6 V, 1 nA

(see Fig.4.12). If there was no step edge barrier at double steps, the material should diffuse two layers downward to fill up the remaining vacancies in the first layer in a very efficient way. This should be followed by the second layer island to extend to similar length as the first layer island before nucleation of the third layer sets in. Hence, in this case, the anisotropy in diffusion speed should lead to an efficient way to fill up the remaining vacancies in lower levels and should result in excellent layer-by-layer growth.

Instead of this scenario, we observe the slow accumulation of deep, elongated vacancies, that are hardly overgrown. The sides of the vacancies are double steps or accumulation of even more steps. Already at a coverage of 3 ML, many of these vacancies can be found (some vacancies are marked by V in Fig. 4.13a-d). Also, nucleation of higher layer islands sets in well before completion of the lower layers. Especially, next layer islands are found on those islands, that have already extended and reached a downward A step. An example of this is given in Fig.4.13d, where such islands of the fourth layer, display small islands of the fifth layer already at a total coverage of 3 ML.

This suggests the existence of a step edge barrier at double steps, which hampers interlayer mass transport in layers beyond a thickness of ≈ 1 ML. During growth, more and more of these double steps are accumulated, interlayer mass transport is suppressed, the growth front significantly roughens and three-dimensional pyramids are formed. The elongated shape of the islands in the different layers due to the (2x1) reconstruction is eventually lost when many double steps are formed and many open

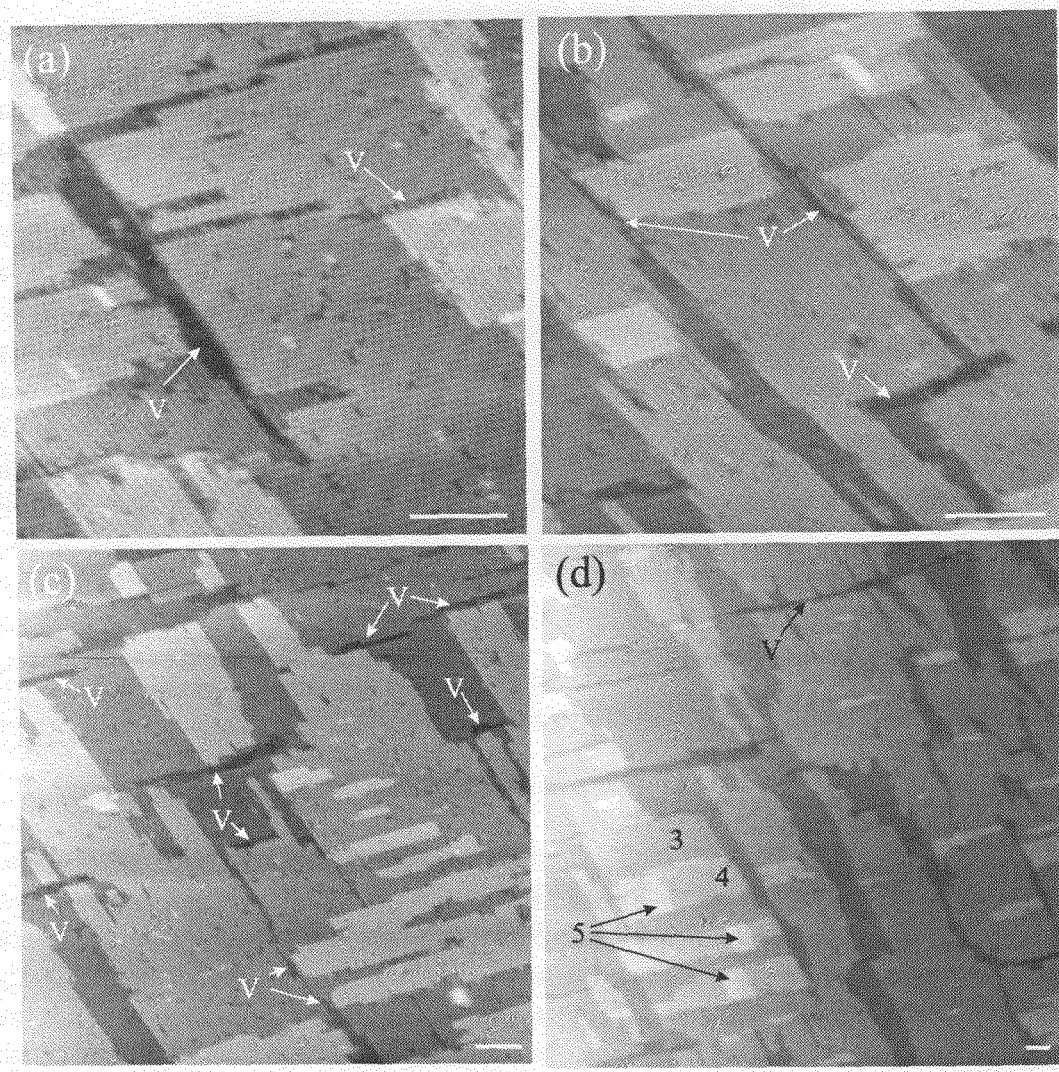

Figure 4.13: Filled state images of the surface after deposition of 3 ML Si with a rate of 1 ML/min. at 525 K. The white bars represent 100Å. Tunneling parameters: 1.6 V, 1 nA

layers are exposed such that pyramids with a nearly quadratic base evolve. The sides of the pyramids consist of multiple steps over which mass transport is inefficient. Double steps can also be understood as (111) micro facets. Then, the hampered diffusion of the adatoms downward over the (111) micro facet of the double step onto the lower terrace is in accord to the higher diffusion barrier observed on the (111) face of Si in comparison to the (100) face[4] (0.67 eV for Si(100) [21] and 0.97 eV for Si(111) [43]). The kinetic formation mechanism of pyramids via formation of

[4] Also from simple arguments about the number of bonds of an adatom to the substrate, diffusion on the (111) surface is slower then on the (100) surface.

double steps also explains the behaviour of the size and separation of the pyramids with growth temperature and the orientation of the sides of the pyramids. At higher temperatures, the island density decreases and the A type step edges of the islands become longer. So, longer double steps with larger separation form, leading to larger pyramids. The proof of the existence of a step edge barrier also for (100) semiconductor surfaces is in contrast to the general believe - namely the absence or insignificance of such a barrier. With this insight, also the pyramidal growth at low temperature of Ge/Ge(100) [42] or the rough growth of Si on Si(100) at low temperatures [41] can be understood.

Further, the accumulaion of multiple steps up to the formation of {11n}, n= $1, 3, 5 \ldots$ facets are known to appear during homoepitaxial growth at low temperatures of Si and Ge on their (100) faces just before the critical thickness is reached and the transition to amorphous growth takes place [44, 45]. Hence, the barrier at double steps, that are present on these facets may even be responsible for the loss of crystallinity, when too many double steps are accumulated.

4.5 Growth Manipulation

Growth manipulation by periodic variation of the growth parameters is known for a couple of years in homoepitaxial growth of Si(111) and Ge(111). As has been shown by Markov et al. [46], variation of the supersaturation during growth close to the step-flow growth regime results in an enhanced amplitude of RHEED oscillations. This observation was explained by synchronous nucleation of islands on all terraces (SN). During undisturbed growth, the small terraces grow via step-flow while on the larger terraces islands nucleate. It is argued that on terraces of intermediate size, nucleation of islands is delayed. During growth, the different terrace sizes then result in a continuous build up of a phase shift in the RHEED oscillations from the different terraces resulting in a slow damping of the macroscopic RHEED oscillations. By SN, this effect is avoided and growth can be monitored by almost undamped RHEED oscillations. However, in the light of our findings it might well be that Markov et al. misinterpreted their data. The modulation of the supersaturation in accord to the concept of two mobilities (see chapter 1.1.2) may lead to better layer-by-layer growth than that already quite good layer-by-layer growth during deposition with constant parameters observed in these systems. An enhanced interlayer mass transport might then be the reason for the stronger oscillations. Unfortunately, no other data than RHEED oscillations are published on SN, especially no quantitative data on film roughness. Hence, our suspicion cannot be further substantiated.

To achieve layer-by-layer growth in Si/Ge(100), the concept of two mobilities is applied to this system. However, the simple premises used to deduce the enhancement of the interlayer mass transport using this concept for metal systems (see chapter 1.1.2) are not fulfilled for this system. First of all, there is no significant step edge barrier at single steps leading to nucleation of next layer islands in

that simple way. In the case of Si/Ge(100), homogeneous nucleation of higher layers mainly takes place, when the islands are terminated by double steps. Hence, the creation of more nuclei does not directly lead to improved interlayer mass transport. On the contrary, an enhanced island density may even be counter productive, since secondly, more nuclei also mean more APBs and by this more inhomogeneous nucleation of second layer islands. And indeed, experiments with an enhanced density of nuclei obtained by nucleation at lowered temperatures or ion bombardment did not lead to layer-by-layer growth. Films grown in the manners display similar roughness as the conventionally grown.

Nevertheless, the concept of two mobilities can be modified to account for the specific kinetic processes during growth of Si/Ge(100). The key point is to avoid long, straight A type step edges and the formation of long double steps hampering interlayer mass transport. Similar to the experiments of manipulated growth of Cu and Ni on Cu(111) of chapter 2.4 and 3.4, deposition of each monolayer is split into two stages with different deposition conditions. In the first stage, $\approx$80% of a monolayer is deposited at a low temperature ($<$ 370 K). In the second stage, deposition is continued at a higher temperature (e.g. 525 K), until the monolayer is completed. During the first stage, the temperature is so low that surface diffusion is too slow to allow the formation of large islands. The islands are very small and irregular and the density of B steps is high and no long A steps are present. The small sizes of the structures evolving at these low growth temperatures result in some lateral disorder and crystal imperfections. We could not achieve dimer row resolution with our STM on films of 0.8 ML Si deposited at this temperature indicating, that the disorder is too large to allow longer dimer rows to evolve (see Fig. 4.14a). Due to the accumulation of crystal imperfections, growth of thicker films at these low temperatures results in a transition to amorphous films [41, 42, 44] [5]. However, interlayer mass transport is still efficient due to the high density of steps and structures locally only two atoms high are observed on the surface. During the second stage of growth, the sample is then heated to an elevated temperature resulting in annealing of the film and a reduction of crystal imperfections such as APBs or non-dimerised atoms. The lateral order of dimer rows is achieved and also material from the second layer can diffuse downward to fill the lower layer. Additionally, during the deposition of the remaining 20% of material for monolayer completion, a high mobility of the atoms on rather small islands allows the filling of the remaining vacancies to some extent, identically to the procedures used earlier during manipulated growth of metals. Fig. 4.14b shows an STM scan after the second stage of deposition, showing the (2x1) reconstructed dimer rows of the film. After 1 ML manipulated growth, no perfect filling of the first layer is achieved similar to conventional growth and no clear advantage of growth manipulation over conventional growth can be deduced from the scans. But keeping in mind, that the reason for roughening during conventional growth is related to the formation of

[5] We could observe neither dimer structure nor atomic steps on 10ML thick films deposited at 370K, even after annealing to 525K.

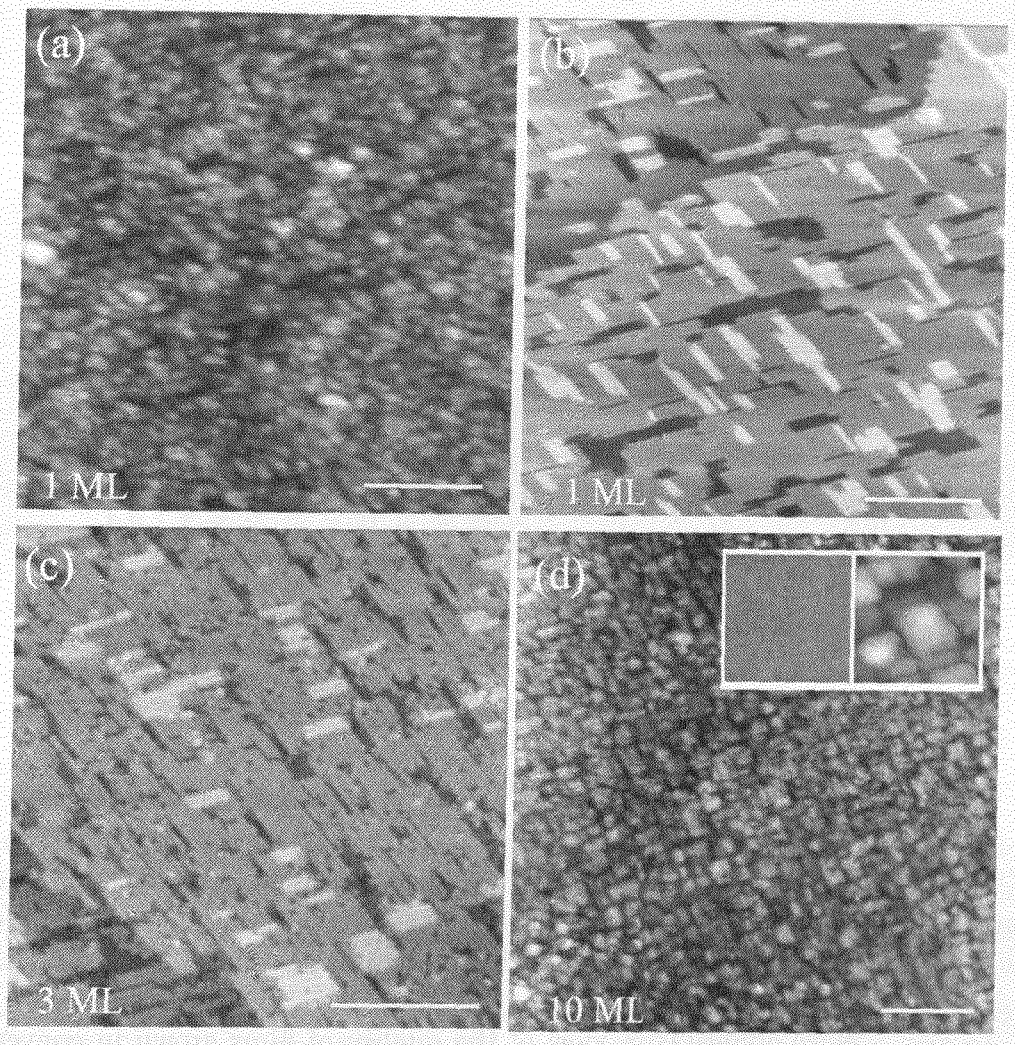

Figure 4.14: Filled state images of the surface after manipulated growth of Si films of thicknesses as indicated. Growth manipulation was done by varying the growth temperature for each monolayer between 370 and 525 K. The inset in d) shows STM scans with identical contrast per height variation after manipulated (left) and conventional (right) growth of 10 ML. The white bars represent 200Å. Tunneling parameters: 1.6 V, 1 nA

double steps at coverage well above 1 ML, this is not surprising. The advantages of growth manipulation only become obvious at higher coverages. Due to the limited diffusion length at low temperatures, the first stage of deposition of the second monolayer during growth manipulation does not lead to the creation of double steps and roughening of the growth front is avoided and the film stays rather flat as illustrated in Fig. 4.14c. At 3 ML coverage, the filling of the third layer is high, only small vacancies are present in this layer and only a small amount of material

is found in the fourth layer.

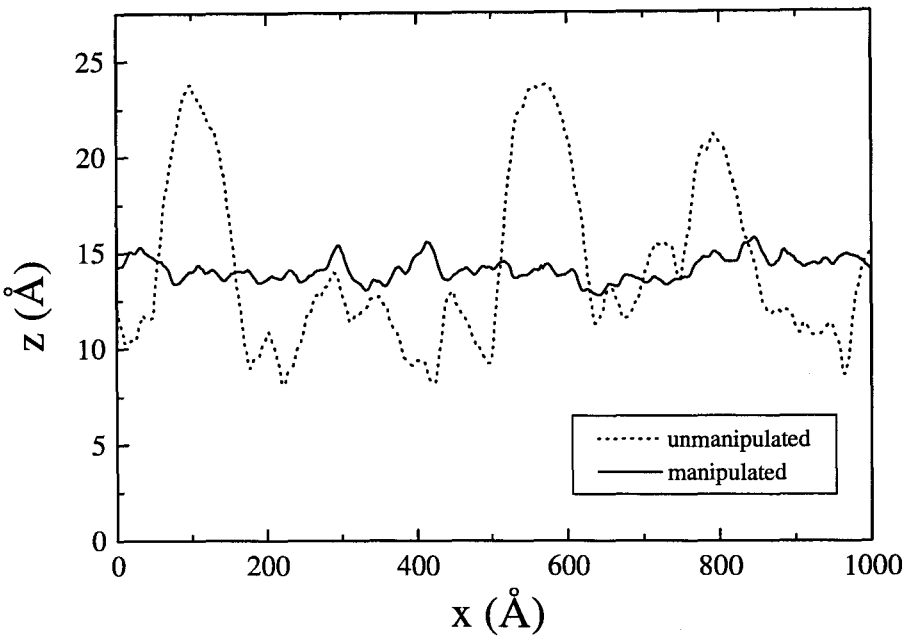

Figure 4.15: Line scans of 10 ML thick Si films resulting from unmanipulated (dotted line) and manipulated (solid line) growth. Tunneling parameters: 1.6 V, 1 nA

To give a more quantitative view of the quality of films grown in conventional and manipulated manner, we concentrate on the roughness of 10 ML films. An example of film morphology after manipulated growth of a 10 ML film is given in the STM scan of Fig. 4.14d. The film surface displays the (2x1) reconstruction with orientations of the dimer rows in registry with the substrate hinting at good crystallinity of the film. Locally, only three layers are exposed which is close to perfect layer-by-layer growth and much less than the ≈11 layers exposed after unmanipulated growth. For a direct comparison of the morphology after manipulated and unmanipulated growth, see the inset of Fig. 4.14d. From linescans of films grown in both manners as displayed in Fig. 4.15, it becomes obvious, that the height variation of the manipulated film is indeed only a fraction of those of the unmanipulated. To quantify this, we calculated the root mean square roughness (RMS-roughness) of the surfaces[6]. Conventionally grown 10 ML films deposited at 525 K display a RMS-roughness of ≈4.5Å. Growth manipulation, with the two growth temperatures set to 370 and 525 K, reduces this value to only ≈0.6Å.

[6]Some minute RMS-roughness (≈0.2 Å) is caused by steps on the substrate and the dimer reconstruction.

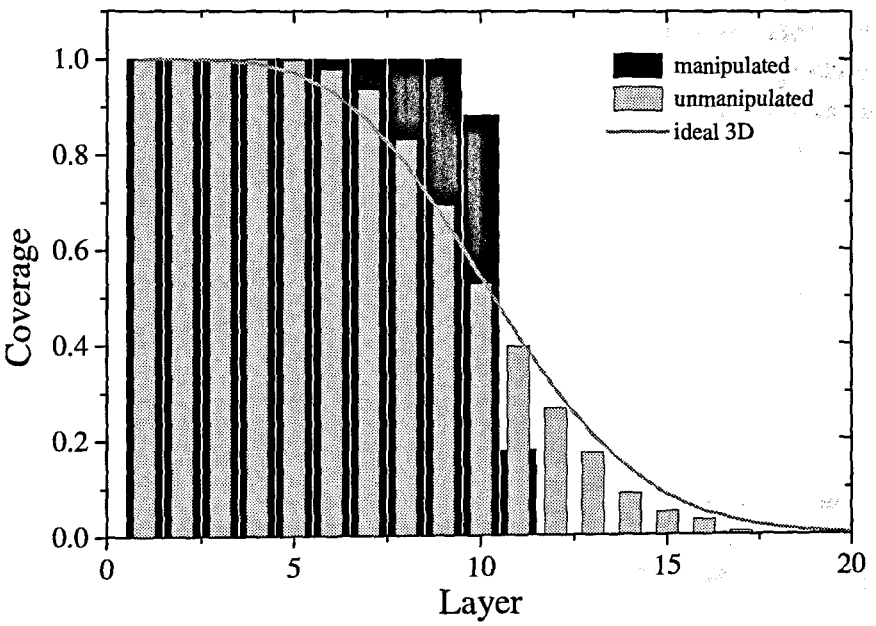

Figure 4.16: Relative coverage as a function of height above substrate in monolayers of unmanipulated, manipulated and ideal three-dimensional growth of 10 ML films.

Also the distribution of material in the different layers of the films clearly shows the significant improvement of film roughness due to growth manipulation. Fig. 4.16 illustrates the distribution of the deposited material in the different layers of the film. Unmanipulated growth at 525 K results in many open layers and a distribution only slightly better than ideal three-dimensional growth. This shows, that interlayer mass transport is indeed strongly suppressed during conventional growth at this temperature. In contrast to the very broad distribution in unmanipulated films, growth manipulation leads to only very few open layers. As can be seen from Fig. 4.16, only three layers are exposed at the surface and the layer distribution has a very sharp edge.

However, due to some uncertainty of the deposition flux, the quality of films grown by growth manipulation varies slightly. Small differences in the deposition rate may lead to a phase shift of temperature variation and monolayer completion during growth of thick layers resulting in less perfect surfaces. To exclude these effects and to optimize growth manipulation, monitoring the deposition by RHEED or a similar technique would be very helpful, in analogy to the experiments of growth manipulation on metals presented in this work. In addition, the crystallinity of the manipulated films has only been checked by STM on the surface. For technical

applications, the defect concentration in the film should be determined by x-ray diffraction. However, this is beyond the scope of this work.

The new growth recipe may be used in similar systems like Ge/Ge(100), Si/Si(100) and Ge/Si(100), allowing the fabrication of layered structures of flat films and avoiding high growth temperatures and by this limiting intermixing. Also, this recipe avoids the formation of (111) micro facets, which might be the cause for a transition to amorphous growth and critical thickness in the homoepitaxy of Si(100) and Ge(100) [41, 42].

In conclusion, we have studied the growth kinetics of Si on Ge(100) and by the insight gained, modified the concept of two mobilities to account for the specific growth kinetics of this system and developed a recipe to grow flat films at relatively low substrate temperatures. For technical applications, however, strong temperature variations for each deposited monolayer of material are impractical. For industrial production, it seems to be more useful to drastically vary the deposition rate during monolayer growth, e.g. by pulsed LASER deposition. Then, deposition with high rates should be used instead of lowering the temperature resulting in similar structures during growth.

Bibliography

[1] E. Kasper and H. Jorke, J. Vac. Sci. Technol. A **10**, 1927 (1992)

[2] G. Theodorou and C. Tserbak, Phys. Rev. B **51**, 4723 (1995)

[3] M. Asai, U. Ueba, C. Tatsuyama, J. Appl. Phys. **58**, 2577 (1985)

[4] M. Krishnamurthy, J.S. Drucker, J.A. Venables, J. Appl. Phys. **69**, 6461 (1991)

[5] H.-J. Gossmann, G.J. Fisanick, Surf. Sci. Lett. **244**, L117 (1991)

[6] M. Copel, M.C. Reuter, M. Horn von Hoegen, R.M. Tromp, Phys. Rev. B **42**, 11682 (1990)

[7] D.J. Eagelsham, M. Cerullo, Phys. Rev. Lett. **64**, 1943 (1990)

[8] S.J. Yun, S.-C. Lee, J.-J. Lee, S.-C. Park, J. Vac. Technol. B **13**, 728 (1995)

[9] X.W. Lin, Z. Liliental-Weber, J. Washbum, E.R. Weber, J. Vac. Technol. B **13**, 1805 (1995)

[10] Y.-W. Mo, D.E. Savage, B.S. Swartzentruber, and M.G. Lagally, Phys. Rev. Lett. **65**, 1020 (1990).

[11] Y.-W. Mo, B.S. Swartzentruber, R. Kariotis, M.B. Webb, and M.G. Lagally, Phys. Rev. Lett. **63**, 2393 (1989).

[12] R.J. Hamers, U.K. Köhler, and J.E. Demuth, J. Vac. Sci. Technol. A **8**, 195 (1990)

[13] A.J. Hoeven, J.M. Lenssinck, D. Dijkkamp, E.J. van Loenen, and J. Dieleman, Phys. Rev. Lett. **63**, 1830 (1989).

[14] F. Wu, X. Chen, Z. Zhang, and M.G. Lagally, Phys. Rev. Lett. **74**, 574 (1995).

[15] M.G. Lagally, Jpn. J. Appl. Phys. **32**, 1493 (1993).

[16] Z.H. Lu, J.-M. Baribeau, D.J. Lockwood, J. Appl. Phys. **76**, 3911 (1994)

[17] H. Janssen, Verslag doctoraal opdracht, University of Twente (1994)

[18] J.A. Kubby, J.E. Griffith, R.S. Becker and J.S. Vickers, Phys. Rev. B **36**, 6079 (1987)

[19] M.C. Payne, N. Roberts, R.J. Needs, M. Needles, J.D. Joannopoulos, Surf. Sci. **211**, 1 (1989)

[20] Y.W. Mo and M.G. Lagally, Surf. Sci. **248**, 313 (1991)

[21] Y. W. Mo, J. Kleiner, M.B. Webb and M.G. Lagally, Phys. Rev. Lett. **66**, 1998 (1991)

[22] Y.W. Mo and M.G. Lagally, J. of Cryst. Growth **111**, 876 (1991)

[23] B.S. Swartzentruber, A.P. Smith and H. Jónsson, Phys. Rev. Lett. **77**, 2518 (1996)

[24] G. Brocks, P.J. Kelly, R. Car, Phys. Rev. Lett. **66**, 1729 (1991)

[25] B.S. Swartzentruber, Phys. Rev. Lett. **76**, 459 (1996)

[26] C. Pearson, M. Krueger, E. Ganz, Phys. Rev. Lett. **76**, 2306 (1996)

[27] R.S. Becker, B.S. Swartzentruber and J.S. Vickers, J. Vac. Sci. Technol. A **6**, 472 (1988)

[28] R.A. Wolkow, Phys. Rev. Lett. **74**, 4448 (1995).

[29] Z. Zhang, F. Wu, H.J.W. Zandvliet, B. Poelsema, H. Metiu, and M.G. Lagally, Phys. Rev. Lett. **74**, 3644 (1995).

[30] P.J. Bedrossian, Phys. Rev. Lett. **74**, 3648 (1995).

[31] J. van Wingerden, A. van Dam, M.J. Haye, P.M.L.O. Scholte and F. Tuinstra, Phys. Rev. B **55**, 4723 (1997)

[32] B.S. Swartzentruber, Phys. Rev. B **55**, 1322 (1997)

[33] G. Brocks, P.J. Kelly and R. Car, Surf. Sci. **269**, 860 (1992)

[34] B. Borovsky, M. Krueger, E. Ganz, Phys. Rev. Lett. **78**, 4229 (1997)

[35] B. Kersten, Nanostructures on stepped semiconductor surfaces, Ph.D. thesis, University of Twente (1995)

[36] C. Roland, G.H. Gilmer, Phys. Rev. Lett. **67**, 3188 (1991)

[37] V. Milman, D.E. jesson, S.J. Pennycook, M.C. Payne, M.H. Lee, I. Stich, Phys. Rev. B **50**, 2663 (1994)

[38] Y.-W. Mo, R. Kariotis, B.S. Swartzentruber, M.B. Webb, and M.G. Lagally, J. Vac. Sci. Technol. A **8**, 201 (1990).

[39] R.J. Hamers, U.K. Köhler, J.E. Demuth, J. Vac. Technol. A **8**, 195 (1990)

[40] J.A. Meyer, P. Schmid, R.J. Behm, Phys. Rev. Lett. **74**, 3864 (1995); H. Brune, K. Bromann, H. Röder, K. Kern, J. Jacobsen, P. Stoltze, K. Jacobsen, J. Nørskov, Phys. Rev. B **52**, R14380 (1995)

[41] N.-E. Lee, D.G. Cahill, J.E. Greene, Phys. Rev. B **53**, 7876 (1996)

[42] J.E. Van Nostrand, S.J. Chey, M.-A. Hasan, D.G. Cahill, J.E. Greene, Phys. Rev. Lett. **74**, 1127 (1995)

[43] S. Kodiyalam, K.E. Khor, S. Das Sara, Phys. Rev. B, **53**, 9913 (1996)

[44] D.J. Eaglesham, H.-J. Gossmann, M. Cerullo, Phys. Rev. Lett. **65**, 1227 (1990)

[45] G. Xue, H.Z. Xiao, M.-A. Hasan, J.E. Greene, H.K. Birnbaum, J. Appl. Phys. **74**, 2512 (1993)

[46] V.A. Markov, O.P. Pchelyakov, L.V. Sokolov, S.I. Stenin, S. Stoyanov, Surf. Sci. **250**, 229 (1991)

Chapter 5

Summary

In this work, the growth of ultra thin films by MBE is studied for three systems - a homoepitaxial as well as a heteroepitaxial metal system without surface reconstructions (Cu/Cu(111) and Ni/Cu(111)) and a heteroepitaxial semiconductor system with reconstructed surfaces (Si/Ge(100)). For all three systems, three-dimensional structures evolve during growth with constant deposition parameters (conventional growth).

In the case of Cu/Cu(111) it is shown that at temperatures below step-flow growth, rough growth is due to very efficient *intra*layer mass transport resulting in laterally large features, while *inter*layer mass transport is hampered by a step edge barrier for diffusion of adatoms over a descending step. The diffusion barrier for adatom diffusion on the flat terrace is estimated to 30^{+10}_{-5} meV. At substrate temperatures below $\approx$200 K, edge diffusion at the step edges of the growing islands is inefficient leading to dendritic islands. At temperatures above $\approx$200 K, edge diffusion sets in and compact islands are observed.

Also in the case of Ni/Cu(111), conventional growth results in rough films. Similar to Cu/Cu(111), *intra*layer mass transport is quick due to a low diffusion barrier for adatoms (79$\pm$18 meV). At low temperatures ($<$ 250 K), multilayer growth is observed. The films consists of pyramids with {445} micro facets. Edge diffusion is limited so that the islands display a triangular shape with {100} step edges determined by faster growth of the {111} step edges in comparison to the {100} step edges. At room temperature growth leads to smoother films which consist of hexagonal structures, but interlayer mass transport is not sufficient to achieve layer-by-layer growth for more than the first layer. Edge diffusion is active at room temperature such that the islands show their equilibrium shape. At temperatures above $\approx$ 425 K, the films grow partially via step-flow, however, intermixing sets in.

In contrast to growth on the high symmetry (111) surface of Cu, diffusion processes of Si on the (2x1) reconstructed surface of Ge(100) are highly anisotropic resulting in a complex kinetic situation during growth. At room temperature, a variety of dimer configurations is observed by STM, showing substantial differences to the growth of Si on Si(100). Also, some elementary diffusion processes as dimer

diffusion along and across substrate dimer rows as well as the collapse of dimer clusters into first layer islands are seen in STM movies. Due to the absence of a barrier for downward diffusion over a B type step edges, practically no homogeneous nucleation of second layer islands takes place during growth of the first layer. However, preferential nucleation is found at anti-phase boundaries of the reconstruction. At higher coverages, the growth front roughens quickly and pyramidal structures evolve. This is traced back to a step edge barrier at double steps.

To improve the quality of the films of all three systems, growth manipulation methods based on the concept of two mobilities is applied. By temperature reduction, rate enhancement during nucleation or pulsed ion beam assisted deposition, the island number density is artificially increased and smoother growth of the first layers is promoted in most cases. However, the growth recipes for manipulated growth have to be adjusted to account for the specific kinetic processes occurring during growth in the three systems.

In the simplest case of Cu/Cu(111), growth manipulation by creation of an enhanced island density via temperature variation or ion bombardment results in almost perfect layer-by-layer growth.

For Ni/Cu(111), temperature reduction fails to promote better growth which is explained by an unusual annealing behaviour of the nuclei. However, manipulated growth via rate variation and ion bombardment is successfully applied to produce smooth films.

Due to the substantially different kinetic origin of the three-dimensional growth of Si/Ge(100), neither ion bombardment nor nucleation at lowered temperatures enhances interlayer mass transport significantly. Realizing that a step edge barrier at double steps is the origin for the rough growth, the concept of two mobilities is adjusted to account for this and layer-by-layer growth is also achieved for this system.

Finally, the use of oxygen as a surfactant modifying the growth mode is investigated for the growth of Cu and Ni on Cu(111). Under some growth conditions, pre-exposure of the surface to oxygen induces weak He-intensity oscillations during deposition. The quality of the films grown in this way is, however, lower than those obtained by growth manipulation techniques.

Chapter 6

Samenvatting

In dit proefschrift wordt de groei van ultra dunne films met behulp van Moleculaire Bundel Epitaxie (MBE) voor drie verschillende systemen - een homoepitaxial systeem alsmede een heteroepitaxial metaal systeem zonder oppervlakte reconstructie (Cu/Cu(111) en Ni/Cu(111)) en een heteroepitaxial halfgeleider systeem met oppervlakte reconstructie - beschreven. Onder de gebruikelijke constante depositiecondities (conventionele groei) ontstaan drie-dimensionale structuren tijdens de groei voor alle drie de systemen.

In het geval van Cu/Cu(111) wordt aangetoond dat voor temperaturen lager dan de step-flow temperatuur, de multilaag groeiwijze het gevolg is van zeer efficient intralaag massa transport, hetgeen leidt tot lateraal grote structuren, terwijl interlaag massa transport gehinderd wordt door een staprand barrière voor diffusie van adatomen over een neergaande stap. De diffusie barrière voor adatoomdiffusie op het vlakke terras wordt geschat op 30^{+10}_{-5} meV. Voor substraattemperaturen hoger dan $\approx$200 K vindt staprand diffusie plaats en ontstaan compacte eilanden.

Ook in het geval van Ni/Cu(111) leidt conventionele groei tot ruwe films. Vergelijkbaar met het Cu/Cu(111) systeem is intralaag massa transport snel tengevolge van een lage diffusie barrière voor atomen (79$\pm$18 meV). De film bestaat voor lage temperaturen (<250 K) uit pyramides met {445} micro facetten. Staprand diffusie is gelimiteerd zodat de eilanden een driehoekige vorm hebben welke begrensd wordt door {100} stapranden omdat de snel groeiende {111} stappen zichzelf elimineren. Groei bij temperaturen rond 300 K leidt tot veel gladdere films met zes-hoekige eilanden, maar het interlaag massa transport is onvoldoende om laag-voor-laag groei te krijgen voor lagen dikker dan 1 laag. Bij kamertemperatuur is de staprand diffusie snel genoeg zodat de eilanden hun evenwichtsvorm kunnen aannemen. Bij temperaturen boven $\approx$425 K groeit de film in de step-flow mode, maar tevens begint ook de menging van de materialen.

In tegenstelling tot de groei op het hoge symmetrie (111) oppervlak van Cu, is de diffusie van Si op het (2x1) gereconstrueerde Ge(100) in hoge mate anisotroop, leidend tot een complexe kinetische situatie gedurende het groeiproces. Bij kamertemperatuur is met STM een grote variateit van dimeerconfiguraties gevonden. Veel van

deze dimeerconfiguraties verschillen van die van het Si/Si(001) systeem. Ook zijn er enige elementaire diffusie processen, zoals de diffusie van een dimeer langs en loodrecht op een substraat dimeerrij alsmede het uiteen vallen van een dimeercluster in separate Si eilanden, zichtbaar gemaakt in STM filmpjes. Door de afwezigheid van een barrière voor diffusie over een enkellaags type B staprand vindt er tijdens de groei van de eerste laag praktisch geen nucleatie van eilanden in de tweede laag plaats. Preferentiële nucleatie vindt plaats aan anti-fase grenzen van de gereconstrueerde laag. Voor hogere bedekkingen verruwt het groeifront snel en een pyramide-achtige structuur ontwikkelt zich. De oorzaak van dit verruwen blijkt te liggen in de aanwezigheid van een staprand barrière voor dubbellaags stappen.

Om de kwaliteit van de gegroeide lagen voor alle drie de systemen te verbeteren wordt groei manipulatie, welke gebaseerd is op het concept van de twee mobiliteiten, toegepast. Door temperatuur reductie, flux verhoging tijdens nucleatie of gepulste ionen bombardement, wordt de eilanddichtheid kunstmatig verhoogd wat in de meeste gevallen tot vlakkere groei van de eerste lagen leidt. De groeirecepten voor gemanipuleerde groei moeten aangepast worden aan het systeem daar de dominerende kinetische processen kunnen verschillen.

In het eenvoudigste systeem, t.w. Cu/Cu(111), wordt bijna perfecte laag-voor-laag groei gerealiseerd door een verhoogde eilanddichtheid door middel van temperatuur variatie of ionen bombardement.

Voor Ni/Cu(111) lukt het niet om met temperatuurreductie de groei te bevorderen Dit heeft te maken met een ongewoon herstelgedrag van de groeikernen. Echter, gemanipuleerde groei middels variatie van flux en ionen bombardement kan met succes worden toegepast om gladdere lagen te produceren.

Tengevolge van het kinetisch wezenlijk anders zijn van de drie-dimensionale groei van Si/Ge(001), leiden zowel ionen bombardement als nucleatie bij lagere temperaturen niet tot een significant beter interlaag massa transport. Realiserend dat de staprand barrière voor dubbelstappen de reden is voor de multilaag groeiwijze is het concept van de twee mobiliteiten aangepast en is uiteindelijk ook laag-voor-laag groei voor dit systeem verkregen.

Tot slot, het gebruik van de surfactant zuurstof is onderzocht voor de groei van Cu en Ni op Cu(111). Onder sommige groei condities induceert pre-expositie van zuurstof zwakke He-intensiteits oscillaties gedurende de depositie. De kwaliteit van deze gegroeide films is echter slechter dan die van de films verkregen door gebruik te maken van groei manipulatie.

Acknowledgments

I thank my Promotors Prof. Dr. George Comsa and Prof. Dr. Bene Poelsema for giving me the opportunity for this promotion, for their generousness, trustful support and unhirarchial guidance.

Also thanks to Dr. Georg Rosenfeld and Dr. Harold Zandvliet for supervising the experiments, for the friendly atmosphere, for many discussions, help and hints and last not least proofreading.

I wish to thank my colleagues and coworkers Dr. Nuphar Lipkin, Jörg Kliewer, Ingo Beckmann and Bart Jan Hattink for their helping hands and company during long hours work in the lab. It was fun to work with you.

Thanks also to all the other members of the group in Jülich and in Enschede, especially Karina Morgenstern, Dietmar Schlösser, Markus Esser, Louis Jorritsma, Petra Hegemann, Bas Hendriksen and Dr. Herbert Wormeester for their discussions about and beyond physics.

An experimental Ph.D. is impossible without the help of the colleagues from the mechanical and electronical workshop. Thanks to Mr. Strobl, Mr. Rausch, Mr. Zimons and Mr. Zillikens.

For technical support I would like to thank Josef Larscheid, Karl Hieble, Ahmet Özdemir, Gerard Kip , Geert Mentink , Herman Oerbekke and especially Dr. Hans-Peter Oepen and Dr. Rudolph David for 'sharing some of their secrets' about UHV technique with me.

I wish to give my special thanks to Udo Linke for the excellent preparation of the Cu(111) single crystals and many hints for crystal handling.

I should not forget to thank my colleagues in Jülich for lots of activities after work, especially Michael Kolk, Jörg Kliewer, Nuphar Lipkin, Karina Morgenstern, Stephanie and Stephan Knappmann and Christoph Hanhart. Life in Jülich would have been hard without them. Many thanks also to the members of the choirs "Junge Chor Haus Overbach" and "Musilon", with whom I had lots of fun with singing and to my Dutch flat-mates Annemarie and Pieter for their company and for teaching me some Dutch.

I owe a lot to Arne, Gert, Barbara, Jörg and all my friends at the "Malteser Hilfsdienst" for their friendship, empathy and support in the dark hours of despair, occasionally caused by the break-down of the vacuum due to power failures or other natural or unnatural catastrophes.

Special thanks to my family and to Angela, Hucki, Juliane and Dörthe for their love, friendship and tolerance through the years of studying.

Forschungszentrum Jülich

Jül-3434
September 1997
ISSN 0944-2952